

---

# **NONLINEAR OPTICAL PARAMETRIC INFRARED GENERATION**

**J. M. Liu**

**Electrical Engineering Department  
University of California, Los Angeles  
Los Angeles, CA 90095**

**May 1996**

**Final Report**

---

**APPROVED FOR PUBLIC RELEASE; DISTRIBUTION IS UNLIMITED.**

---

DTIC QUALITY INSPECTED 4



**PHILLIPS LABORATORY  
Lasers and Imaging Directorate  
AIR FORCE MATERIEL COMMAND  
KIRTLAND AIR FORCE BASE, NM 87117-5776**

---

19960924 172

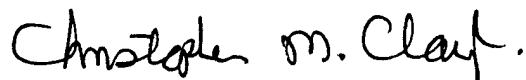
Using Government drawings, specifications, or other data included in this document for any purpose other than Government procurement does not in any way obligate the U.S. Government. The fact that the Government formulated or supplied the drawings, specifications, or other data, does not license the holder or any other person or corporation; or convey any rights or permission to manufacture, use, or sell any patented invention that may relate to them.

This report has been reviewed by the Public Affairs Office and is releasable to the National Technical Information Service (NTIS). At NTIS, it will be available to the general public, including foreign nationals.

If you change your address, wish to be removed from this mailing list, or your organization no longer employs the addressee, please notify PL/LIDN, 3550 Aberdeen Ave SE, Kirtland AFB, NM 87117-5776.

Do not return copies of this report unless contractual obligations or notice on a specific document requires its return.

This report has been approved for publication.



CHRISTOPHER M. CLAYTON  
Project Manager

FOR THE COMMANDER



MARC R. HALLADA, LtCol, USAF  
Chief, Laser Systems Division



ROBERT A. DURYEA, Col, USAF  
Director, Lasers and Imaging Directorate

# DRAFT SF 298

<b>1. Report Date (dd-mm-yy)</b> 21 May 96		<b>2. Report Type</b> Final Report		<b>3. Dates covered (from... to )</b> Feb 93 - May 96	
<b>4. Title &amp; subtitle</b> Nonlinear Optical Parametric Infrared Generation				<b>5a. Contract or Grant #</b> F29601-93-K-0016	
				<b>5b. Program Element #</b> 62601F	
<b>6. Author(s)</b> J. M. Liu				<b>5c. Project #</b> 3326	
				<b>5d. Task #</b> LA	
				<b>5e. Work Unit #</b> AC	
<b>7. Performing Organization Name &amp; Address</b> Department of Electrical Engineering University of California, Los Angeles Los Angeles, CA 90095					<b>8. Performing Organization Report #</b>
<b>9. Sponsoring/Monitoring Agency Name &amp; Address</b> Phillips Laboratory/LIDN 3550 Aberdeen Ave SE Kirtland AFB, NM 87117-5776					<b>10. Monitor Acronym</b> PL
					<b>11. Monitor Report #</b> PL-TR-96-1106
<b>12. Distribution/Availability Statement</b> Approved for public release; distribution is unlimited.					
<b>13. Supplementary Notes</b>					
<b>14. Abstract</b> The synchronously pumped optical parametric oscillator is an efficient, wavelength-tunable laser source that makes it possible to generate wavelength-tunable picosecond and femtosecond pulses which cover the wavelength range from visible to mid-infrared. A theoretical model for calculating the effective gain of parametric generation and amplification of ultrashort optical pulses is presented. An analytical formulation for the parametric efficiency coefficient and the effective gain in terms of six spatial and temporal characteristic lengths is obtained. Also presented is the experimental work to construct such a source based on the additive-pulse mode-locked Nd:YLF laser pulses. The design and characteristics of the KTP based picosecond synchronously pumped optical parametric oscillator are discussed and compared with the previous theoretical work. Efforts to extend the wavelength range to 10 microns by use of a newly developed crystal are included. Parametric generation of femtosecond optical pulses is also presented.					
<b>15. Subject Terms</b> nonlinear optics, optical parametric processes, frequency agility					
<b>Security Classification of</b>			<b>19. Limitation of Abstract</b>  Unlimited	<b>20. # of Pages</b>  200	<b>21. Responsible Person (Name and Telephone #)</b>  Dr Chris Clayton 505-846-4754
<b>16. Report</b> Unclassified	<b>17. Abstract</b> Unclassified	<b>18. This Page</b> Unclassified			

# Contents

<b>List of Tables</b>	<b>vi</b>
<b>List of Figures</b>	<b>xv</b>
<b>1.0 Introduction</b>	<b>1</b>
1.1 Introduction . . . . .	1
1.2 Background . . . . .	3
1.3 Previous Theoretical Approach . . . . .	4
1.4 Previous Experimental Demonstrations . . . . .	6
1.5 Outline of The Report . . . . .	8
<b>2.0 Theory of Parametric Gain</b>	<b>10</b>
2.1 Theoretical Approach . . . . .	10
2.2 Spatial Effects . . . . .	12
2.3 Temporal Effects . . . . .	15
2.4 Effective Gain . . . . .	20
2.5 Noncollinear Phase Matching . . . . .	23
<b>3.0 Numerical Simulation</b>	<b>32</b>
3.1 Collinear Phase Matching . . . . .	32
3.1.1 Beam and Pulse Broadening . . . . .	33
3.1.2 Spatial and Temporal Characteristic Lengths . . . . .	34
3.1.3 Spatial and Temporal Overlap . . . . .	41
3.1.4 Effective Interaction Length and Optimal Crystal Length . .	44
3.1.5 Parametric Efficiency Coefficient . . . . .	50

3.2	Noncollinear Phase Matching . . . . .	59
3.2.1	Maximization of Parametric Efficiency Coefficient for Non- collinear Phase Matching Cases . . . . .	60
3.2.2	Characteristic Lengths for Noncollinear Phase Matching . .	61
3.2.3	Parametric Efficiency Coefficient for Noncollinear Phase Match- ing . . . . .	64
<b>4.0</b>	<b>Pump Laser System</b>	<b>74</b>
4.1	Experimental Setup . . . . .	74
4.2	Noise Characteristics . . . . .	78
<b>5.0</b>	<b>AgGaS<sub>2</sub> Based Optical Parametric Oscillator</b>	<b>86</b>
5.1	Nonlinear Crystal . . . . .	86
5.2	Experimental Setup . . . . .	89
5.3	Results . . . . .	91
<b>6.0</b>	<b>Picosecond KTP Optical Parametric Oscillator</b>	<b>94</b>
6.1	Introduction . . . . .	94
6.2	Experimental Setup . . . . .	96
6.3	Characteristics of OPO . . . . .	102
6.4	High-Order Transverse Mode and Multiple wavelength Oscillation .	113
6.5	Discussions and Summary . . . . .	117
<b>7.0</b>	<b>Parametric Generation of Femtosecond Optical Pulses</b>	<b>122</b>
7.1	Introduction . . . . .	122
7.2	Second Harmonic Generation of Femtosecond Optical Pulses at 1053nm	123

7.3	Pulse Compression of Picosecond Pulse at 527 nm . . . . .	130
7.4	Threshold Study of Femtosecond OPO . . . . .	137
<b>8.0</b>	<b>Conclusions</b>	<b>139</b>
8.1	Summary . . . . .	139
8.2	Future Research . . . . .	143
	<b>References</b>	<b>146</b>
<b>A</b>	<b>Spectral Measurement of The Noise in Continuous-Wave Mode-Locked Laser Pulses</b>	<b>159</b>
A.1	Introduction . . . . .	159
A.2	Theoretical Derivation . . . . .	161
A.2.1	Noise Model . . . . .	161
A.2.2	Approximations . . . . .	162
A.2.3	Power Spectra . . . . .	163
A.2.4	Response of The Detection System . . . . .	166
A.3	Measurement Method . . . . .	167
A.4	Experimental Demonstration . . . . .	171
A.5	Discussions and Conclusion . . . . .	174
<b>B</b>	<b>Small Noise Approximations</b>	<b>176</b>
<b>C</b>	<b>Derivation of Power Spectra</b>	<b>177</b>
<b>D</b>	<b>Bibliography</b>	<b>181</b>

## List of Tables

1	Variation of temporal characteristic lengths with pump wavelength for 50 fs pump pulsewidth and 4 $\mu\text{m}$ signal wavelength. . . . .	49
2	$\beta_k$ of the Gaussian and $\text{sech}^2$ pulse shape . . . . .	165
3	Noise parameters of the fundamental and second harmonic pulses .	173

## List of Figures

1	Transmission windows of various nonlinear crystals(Upper half) and wavelength range of several existing lasers(Lower half) . . . . .	2
2	Propagation of an arbitrary beam in an anisotropic medium. The directions of $\mathbf{E}$ , $\mathbf{D}(\omega)$ , $\mathbf{E} \times \mathbf{H}$ , and $\mathbf{k}$ lie in the $xz$ -plane. . . . .	14
3	Schematic diagram of the collinear phase matching in KTP. . . . .	27
4	Schematic diagram of the noncollinear phase matching in KTP. . .	28
5	Phase matching angle and the angle of walkoff for $\lambda_3 = 1.053 \mu\text{m}$ . .	30
6	Percentage of (a) spatial beam broadening for focused beams of 20 $\mu\text{m}$ and 100 $\mu\text{m}$ initial beam waists and (b) temporal pulse broad- ening for nonchirped pulses of 50 fs and 500 fs initial pulsewidths as a function of wavelength after traveling 5 mm through a KTP crystal with field polarization along one of the principal axes. . . . .	35

7	Spatial characteristic lengths normalized to pump beam waist as a function of signal wavelength for three different pump wavelengths at 1.053 $\mu\text{m}$ , 780 nm, 527 nm using collinear phase matching geometry. The solid curves are for $o \rightarrow o + e$ phase matching and the dashed curves are for $o \rightarrow e + o$ . . . . .	37
8	Temporal characteristic lengths normalized to pump pulsewidth waist as a function of signal wavelength for three different pump wavelengths at 1.053 $\mu\text{m}$ , 780 nm, 527 nm. The data of $l_{tc}/\Delta t_{30}^2$ for 527 nm pump wavelength have very large absolute values outside of the scale for (b) and are not shown. The solid curves are for $o \rightarrow o + e$ phase matching and the dashed curves are for $o \rightarrow e + o$ . . . . .	40
9	Ratio of pump pulsewidth to pump beam waist when spatial and temporal walk-off lengths are equal as a function of signal wavelength for three different pump wavelengths at 1.053 $\mu\text{m}$ , 780 nm, 527 nm using collinear phase matching geometry. The solid curves are for $o \rightarrow o + e$ phase matching and the dashed curves are for $o \rightarrow e + o$ . . . . .	41



- 10 Distributions of the spatial contribution,  $\sigma_s$  (dotted curves), the temporal contribution,  $\sigma_t$  (dashed curves), and the total integrand,  $\sigma$  (solid curves), of the integral for the effective interaction lengths as a function of distance in a 5-mm KTP crystal for pump at  $1.053 \mu\text{m}$  and signal at  $3 \mu\text{m}$  wavelength with  $o \rightarrow o + e$  phase matching. Different combinations of pump beam waists of  $20 \mu\text{m}$  and  $100 \mu\text{m}$  with pump pulsewidths of 50 fs and 500 fs are shown. In (a), both beam overlap and pulse synchronization coincide at the center of the crystal. In (b) and (c), beam overlap occurs at the center but pulses are synchronized at the surface of the crystal. . . . . 43
- 11 Distributions of the integrand,  $\sigma$ , of the integral for the effective interaction length as a function of distance for three different crystal lengths,  $l_c = 1, 5$ , and  $10 \text{ mm}$ , and three different pump wavelengths at  $1.053 \mu\text{m}$  (dotted curves),  $780 \text{ nm}$  (dashed curves), and  $527 \text{ nm}$  (solid curves), but the same signal wavelength at  $4 \mu\text{m}$  with  $o \rightarrow o + e$  phase matching. . . . . 48
- 12 Parametric efficiency coefficient in KTP as a function of signal wavelength in the case of  $w_{30} = 100 \mu\text{m}$  and  $\Delta t_{30} = 5 \text{ ps}$  for three different pump wavelengths at (a)  $1.053 \mu\text{m}$ , (b)  $780 \text{ nm}$ , and (c)  $527 \text{ nm}$  using collinear phase matching geometry. The solid curves are for  $o \rightarrow o + e$  phase matching and the dashed curves are for  $o \rightarrow e + o$ . 52

- 13 Parametric efficiency coefficient in KTP as a function of signal wavelength in the case of  $w_{30} = 100 \mu\text{m}$  and  $\Delta t_{30} = 500 \text{ fs}$  for three different pump wavelengths at (a)  $1.053 \mu\text{m}$ , (b)  $780 \text{ nm}$ , and (c)  $527 \text{ nm}$  using collinear phase matching geometry. The solid curves are for  $o \rightarrow o + e$  phase matching and the dashed curves are for  $o \rightarrow e + o$ . 53
- 14 Parametric efficiency coefficient in KTP as a function of signal wavelength in the case of  $w_{30} = 100 \mu\text{m}$  and  $\Delta t_{30} = 50 \text{ fs}$  for three different pump wavelengths at (a)  $1.053 \mu\text{m}$ , (b)  $780 \text{ nm}$ , and (c)  $527 \text{ nm}$  using collinear phase matching geometry. The solid curves are for  $o \rightarrow o + e$  phase matching and the dashed curves are for  $o \rightarrow e + o$ . 54
- 15 Parametric efficiency coefficient in KTP as a function of signal wavelength in the case of  $w_{30} = 20 \mu\text{m}$  and  $\Delta t_{30} = 5 \text{ ps}$  for three different pump wavelengths at (a)  $1.053 \mu\text{m}$ , (b)  $780 \text{ nm}$ , and (c)  $527 \text{ nm}$  using collinear phase matching geometry. The solid curves are for  $o \rightarrow o + e$  phase matching and the dashed curves are for  $o \rightarrow e + o$ . 56
- 16 Parametric efficiency coefficient in KTP as a function of signal wavelength in the case of  $w_{30} = 20 \mu\text{m}$  and  $\Delta t_{30} = 500 \text{ fs}$  for three different pump wavelengths at (a)  $1.053 \mu\text{m}$ , (b)  $780 \text{ nm}$ , and (c)  $527 \text{ nm}$  using collinear phase matching geometry. The solid curves are for  $o \rightarrow o + e$  phase matching and the dashed curves are for  $o \rightarrow e + o$ . 57

17	Parametric efficiency coefficient in KTP as a function of signal wavelength in the case of $w_{30} = 20 \mu\text{m}$ and $\Delta t_{30} = 50 \text{ fs}$ for three different pump wavelengths at (a) $1.053 \mu\text{m}$ , (b) $780 \text{ nm}$ , and (c) $527 \text{ nm}$ using collinear phase matching geometry. The solid curves are for $o \rightarrow o + e$ phase matching and the dashed curves are for $o \rightarrow e + o$ .	58
18	Changes in $\alpha$ 's, $\gamma$ 's, and the value of $l_{sw}$ at $\lambda_1 = 2.00 \mu\text{m}$ and $\lambda_3 = 1.053 \mu\text{m}$ for $o \rightarrow e + o$ phase matching as $\theta_1$ varies from $\theta_c$ to $\theta_c + 2\alpha_c$ .	62
19	Changes in $\alpha$ 's, $\gamma$ 's, and the value of $l_{sw}$ at $\lambda_1 = 3.25 \mu\text{m}$ and $\lambda_3 = 1.053 \mu\text{m}$ for $o \rightarrow e + o$ phase matching as $\theta_1$ varies from $\theta_c$ to $\theta_c + 2\alpha_c$ .	63
20	Spatial characteristic lengths normalized to pump beam waist as a function of signal wavelength for three different pump wavelengths at $1.053 \mu\text{m}$ , $780 \text{ nm}$ , $527 \text{ nm}$ using noncollinear phase matching geometry. The solid curves are for $o \rightarrow o + e$ phase matching and the dashed curves are for $o \rightarrow e + o$ .	65
21	Ratio of pump pulsewidth to pump beam waist when spatial and temporal walk-off lengths are equal as a function of signal wavelength for three different pump wavelengths at $1.053 \mu\text{m}$ , $780 \text{ nm}$ , $527 \text{ nm}$ using noncollinear phase matching geometry. The solid curves are for $o \rightarrow o + e$ phase matching and the dashed curves are for $o \rightarrow e + o$ .	66

- 22 Parametric efficiency coefficient in KTP as a function of signal wavelength in the case of  $w_{30} = 100 \mu\text{m}$  and  $\Delta t_{30} = 5 \text{ ps}$  for three different pump wavelengths at (a)  $1.053 \mu\text{m}$ , (b)  $780 \text{ nm}$ , and (c)  $527 \text{ nm}$  using noncollinear phase matching geometry. The solid curves are for  $o \rightarrow o + e$  phase matching and the dashed curves are for  $o \rightarrow e + o$ . 67
- 23 Parametric efficiency coefficient in KTP as a function of signal wavelength in the case of  $w_{30} = 100 \mu\text{m}$  and  $\Delta t_{30} = 500 \text{ fs}$  for three different pump wavelengths at (a)  $1.053 \mu\text{m}$ , (b)  $780 \text{ nm}$ , and (c)  $527 \text{ nm}$  using noncollinear phase matching geometry. The solid curves are for  $o \rightarrow o + e$  phase matching and the dashed curves are for  $o \rightarrow e + o$ . 68
- 24 Parametric efficiency coefficient in KTP as a function of signal wavelength in the case of  $w_{30} = 100 \mu\text{m}$  and  $\Delta t_{30} = 50 \text{ fs}$  for three different pump wavelengths at (a)  $1.053 \mu\text{m}$ , (b)  $780 \text{ nm}$ , and (c)  $527 \text{ nm}$  using noncollinear phase matching geometry. The solid curves are for  $o \rightarrow o + e$  phase matching and the dashed curves are for  $o \rightarrow e + o$ . 69
- 25 Parametric efficiency coefficient in KTP as a function of signal wavelength in the case of  $w_{30} = 20 \mu\text{m}$  and  $\Delta t_{30} = 5 \text{ ps}$  for three different pump wavelengths at (a)  $1.053 \mu\text{m}$ , (b)  $780 \text{ nm}$ , and (c)  $527 \text{ nm}$  using noncollinear phase matching geometry. The solid curves are for  $o \rightarrow o + e$  phase matching and the dashed curves are for  $o \rightarrow e + o$ . 71

26	Parametric efficiency coefficient in KTP as a function of signal wavelength in the case of $w_{30} = 20 \mu\text{m}$ and $\Delta t_{30} = 500 \text{ fs}$ for three different pump wavelengths at (a) $1.053 \mu\text{m}$ , (b) $780 \text{ nm}$ , and (c) $527 \text{ nm}$ using noncollinear phase matching geometry. The solid curves are for $o \rightarrow o + e$ phase matching and the dashed curves are for $o \rightarrow e + o$ .	72
27	Parametric efficiency coefficient in KTP as a function of signal wavelength in the case of $w_{30} = 20 \mu\text{m}$ and $\Delta t_{30} = 50 \text{ fs}$ for three different pump wavelengths at (a) $1.053 \mu\text{m}$ , (b) $780 \text{ nm}$ , and (c) $527 \text{ nm}$ using noncollinear phase matching geometry. The solid curves are for $o \rightarrow o + e$ phase matching and the dashed curves are for $o \rightarrow e + o$ .	73
28	Schematic of the pump laser system and the measurement setup. Inside the dashed box is the pump laser. . . . .	75
29	The autocorrelation trace of the APM Nd:YLF laser pulse. . . . .	76
30	The spectrum of the APM Nd:YLF laser pulse. . . . .	77
31	(a) The single-sideband timing jitter noise spectra and (b) the single-sideband amplitude noise spectra of the Nd:YLF laser in both active mode-locking and APM operation modes in units of decibels below the carrier in a 1-Hz bandwidth. . . . .	80
32	The noise power spectra of the 30th harmonic of the Nd:YLF laser under a cavity length detuning of $100 \mu\text{m}$ for both active mode-locking and APM cases. . . . .	82
33	(a) The rms timing jitter and (b) the rms amplitude noise of the APM Nd:YLF laser as a function of cavity mismatch. . . . .	83

34	Calculated tuning curves for Type I(Solid line) and Type II (Dotted line) phase matching of AgGaS <sub>2</sub> for the pump wavelength of 1053 nm	87
35	The experimental setup of the silver thiogallate OPO . . . . .	90
36	The autocorrelation trace of the 527 nm pump pulse . . . . .	97
37	The spectrum of the 527 nm pump pulse . . . . .	98
38	Schematic of the KTP OPO setup. . . . .	99
39	Parametric wavelength-tuning curves for KTP pumped at 527 nm(left) and 1053 nm(right) as a function of phase matching angle for different crystal cuts to phase match in the <i>xy</i> -, <i>xz</i> -, and <i>yz</i> -planes, respectively. . . . .	101
40	The average signal and idler output power versus the average pump power sent into the KTP crystal. . . . .	104
41	The total signal and idler efficiency versus the average power sent into the KTP crystal. . . . .	105
42	The percentage of pump depletion and total conversion efficiency versus the average power sent into the KTP crystal. . . . .	106
43	The background-free autocorrelation of (a) the signal pulses at the wavelength of 889 nm and (b) the idler pulses at wavelength of 1292 nm. The dots correspond to the experimental data; the solid line is the theoretical fitting curve assuming a Gaussian pulse shape.	108
44	Spectrum of (a) the signal pulses at the wavelength of 889 nm and (b) the idler pulses at the wavelength of 1292 nm. . . . .	109
45	The single-wavelength TEM <sub>00</sub> mode signal output power as a function of cavity-length detuning. . . . .	111

46	Tuning curve for KTP OPO phase-matched in $xz$ -plane for a 527 nm pump. Thick bars correspond to the experimental data points. Solid lines are calculated tuning curves. . . . .	112
47	Spectra of the signal pulses with different transverse modes. The solid line represents the spectrum of a $TEM_{00}$ mode and the dashed line corresponds to the spectrum of a $TEM_{11}$ mode. . . . .	114
48	Spectra of the signal and idler pulses under different conditions of multiple-wavelength oscillation. . . . .	116
49	Signal output power as a function of cavity-length detuning under the condition of Fig. 4.10(e) and (f). . . . .	118
50	Broadened spectrum of the pulse emerging from the 85 cm length of fiber. . . . .	124
51	The arrangement of a grating-prism dispersive delay line . . . . .	126
52	Autocorrelation trace of the compressed 1053 nm pulse . . . . .	127
53	The spectrum of the 527 nm pulses generated by second harmonic generation of 450 fs pulses at 1053 nm . . . . .	128
54	The autocorrelation trace of the 527 nm pulses generated by second harmonic generation of 450 fs pulses at 1053 nm . . . . .	129
55	The spectrum of the output pulse emerging from the 2 m length of fiber. . . . .	131
56	Average output power of the 527 nm and the first Raman Stokes emerging from a 2 m long fiber as a function of the average power coupled into the fiber . . . . .	132
57	The spectrum of the output pulse emerging from a 65 cm long fiber.	134

58	The configuration of the prism pair dispersive delay line . . . . .	135
59	The autocorrelation trace of the 527 nm pulses exiting the fiber prism-pair pulse compressor . . . . .	136
60	The Schematic diagram of the current available laser pulses(solid line) and the future systems(dotted line). . . . .	144
61	Total noise power $\sigma_{n_k}^2$ of (a) the fundamental and (b) the second harmonic pulses of an actively mode-locked Nd:YLF laser. The solid line is the fitting curve of Eq. 93. The dashline is the fitting curve of Eq. 102. . . . .	172



# 1.0 Introduction

## 1.1 Introduction

Ultrashort wavelength-tunable optical pulses are useful in time resolved study of ultrafast processes in semiconductors and molecular vibrations. However, the existing wavelength-tunable lasers, such as dye lasers, color-center lasers, and Ti:sapphire laser, only cover a portion of the spectral range from visible to near infrared. In the spectral range of wavelength longer than  $2\text{ }\mu\text{m}$ , wavelength-tunable laser pulses had not been available except for several particular wavelengths, such as the recently developed solid state lasers doped with Er, Tm, or Ho and  $\text{CO}_2$  laser.

With the advances in the development of various nonlinear crystals and the techniques of generating femtosecond and picosecond continuous wave (cw) mode-locked pulses, difference-frequency generation and optical parametric generation became promising to generate wavelength-tunable optical pulses. In order to generate wavelength-tunable pulses by use of difference-frequency generation, one fixed-wavelength pulsed laser and one wavelength-tunable pulsed laser have to be used. However, only one pump laser is required in optical parametric generation and wavelength tuning is simply achieved by tuning the nonlinear crystal. Figure 1.1 shows the transmission windows of various nonlinear crystals and the wavelength range of several existing lasers. It can be seen clearly that the wide range of transmission windows of various nonlinear crystals offers a possibility to generate wavelength-tunable pulses which cover the visible to infrared range. The goal of this project is to efficiently generate wavelength-tunable ultrashort optical pulses.

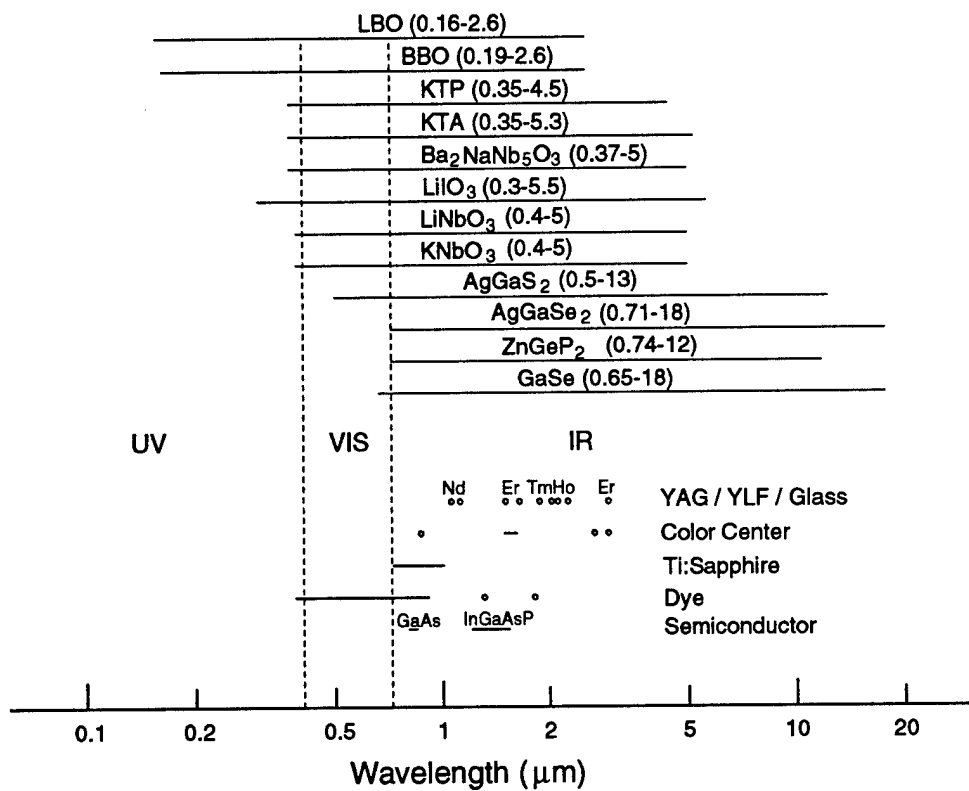


Figure 1: Transmission windows of various nonlinear crystals(Upper half) and wavelength range of several existing lasers(Lower half)

A brief discussion on the background of synchronously pumped optical parametric oscillators (OPOs), previous theoretical approaches and their deficiencies, a summary of previous experimental demonstrations, and outline of this report are given in this section.

## 1.2 Background

In recent years, there has been a renewed interest in parametric generation of wavelength-tunable ultrashort pulses. This is largely due to recent developments in two fundamental areas of research in the field of nonlinear optics. First, more advanced methods in crystal growth technology produced high-quality nonlinear optical crystals with higher nonlinearity, wider transmission range, and higher damage threshold. Second, recent developments in laser technology made more efficient pump sources of picosecond and femtosecond mode-locked lasers readily available. Depending on the experimental conditions, such as the energy and repetition rate of the pump pulses, different approaches can be taken for efficient parametric generation of these ultrashort pulses. With pump pulses of high pulse energy but low repetition rate, direct traveling-wave optical parametric generation with single or multiple stages is often efficient enough [1, 2]. If a second pulsed laser source with wavelength tunability is available and is synchronized to the pump pulses, wavelength tunable pulses at the difference frequency can be generated simply by difference-frequency generation [3]. However, with a single pump source of cw mode-locked picosecond or femtosecond pulses at a high repetition rate but low individual pulse energy, the most efficient approach is the cw synchronously pumped OPO [4, 5]. Very efficient cw synchronously pumped OPOs with wide

wavelength tuning ranges have recently been demonstrated for the generation of both picosecond [6, 7, 8, 9, 10, 11, 12, 13, 14, 15, 16] and femtosecond [17, 18, 19, 20, 21, 22, 23, 24, 25, 26] pulses.

### 1.3 Previous Theoretical Approach

As much as the recent interest in OPOs is high, much of the theoretical studies analyzing OPOs have been done since the birth of nonlinear optics in the early 60's. However, much of the studies have been performed for the cw and quasi-cw systems. Only a few groups have analyzed the theoretical model of cw synchronously pumped optical parametric oscillators which is the system of our concern. From these groups, several efforts are worth mentioning. Becker *et al.* [27] have considered a degenerate case, in which the signal and the idler wavelengths are equal, and derived some approximate solutions only for a few special cases. The more general degenerate OPO cases were analyzed through numerically solving the coupled wave equations. This method, however, is time consuming and is not efficient in studying the various effects of the OPO. Moreover, the synchronously pumped OPO was only considered for the plane wave case [27]. Although more realistic approaches in analyzing the OPO system were undertaken by several groups using the Gaussian beams on the parametric interactions and on OPOs, their studies were limited to the quasi-steady-state case in which the continuous-wave (time-independent) solutions of the parametric interaction are assumed at each instant [28, 29, 30, 31, 32].

A more complete, efficient method for analyzing various effects of the synchronously pumped OPO was not available until the two recent publications by

Cheung and Liu [4, 5]. In Ref. [4], a theoretical model for cw synchronously pumped OPOs was developed and detailed numerical simulations were carried out to describe the general characteristics of cw synchronously pumped OPOs. In a subsequent extension [5] of this model, the spatial effects of the interacting beams in a generally anisotropic nonlinear crystal were considered, various nonlinear crystals for parametric generation of infrared pulses were compared for their relative efficiencies, and some useful design criteria for practical systems were established [5]. Many significant characteristics of cw synchronously pumped OPOs predicted by these analyses have been verified by recent experimental results [6, 11, 14, 16].

The temporal effects, including temporal walk-off and group-velocity-dispersion, of the interacting pulses in parametric systems were considered in both the original and extended models of Cheung and Liu [4, 5]. In these models, these temporal effects appear in three terms, two containing first-order time derivatives and one containing second-order time derivatives either in the final master differential equation describing a cw synchronously pumped OPO. When the master differential equation including these terms is solved, the temporal effects are automatically accounted for. In Ref. [4], a detailed numerical simulation was performed to include the temporal effects in the coupled wave equations and described many detailed characteristics of the parametric pulses. However, this type of analysis is time consuming and complicated and did not address the issues of more practical questions, such as; How do the effective parametric gain and efficiency of a system change with varying pulsewidth and varying signal wavelength? and; What is the optimal crystal length for a femtosecond OPO? Although the extended model in Ref. [5] was more practical in answering such questions for various nonlinear crystals in

a synchronously pumped OPO, only the spatial effects were treated extensively while the temporal effects were only included as perturbations to the solution of the coupled wave equations. Clearly, the temporal effects become more important than the spatial effects as the pulses become shorter. When working with systems generating picosecond and, in particular, femtosecond pulses, one often faces these practical questions. As we shall see in the following sections, for femtosecond systems the limitations imposed by the temporal effects often become more important than those imposed by the spatial effects. Although some criteria were set in the extended model of Cheung and Liu [5] for the limitation of useful crystal length due to temporal effects, a more detailed analysis is clearly needed to address these questions without having to numerically solve the master differential equation. Therefore, to answer such practical questions often asked by many, we present a method for analyzing the OPO systems with various crystal lengths, pulsewidths, and beam waists.

## 1.4 Previous Experimental Demonstrations

The most efficient way to generate wavelength-tunable ultrashort optical pulses by using femtosecond or picosecond mode-locked pulses at high repetition rate with low pulse energy is the synchronously pumped optical parametric oscillator (OPO). For many years OPO pumped by Q-switched mode-locked lasers have been demonstrated to generate picosecond wavelength-tunable pulses from visible to mid-infrared[33, 34, 35, 36]. However, the pulsewidth and the amplitude of these pulses are not constant and the pulses are not truly repetitive.

Piskarskas *et al.* [6] first demonstrated a doubly resonant cw mode-locked synchronously pumped optical parametric oscillator in 1988 by use of a  $\text{Ba}_2\text{NaNb}_5\text{O}_{15}$  crystal and a cw mode-locked Nd:YAG laser. The advantage of the doubly resonant OPO is the low pump threshold. The disadvantage of the doubly resonant OPO is the poor output stability.

In 1989 Edelstein *et al.* [17] first demonstrated a cw mode-locked KTP-based singly resonant OPO. The nonlinear crystal of the OPO is located inside the cavity of a colliding-pulse passively mode-locked dye laser. Mak *et al.* [19] demonstrated the first externally synchronously pumped, singly resonant OPO which produced 220 fs pulses tunable from 1200 to 1290 nm with an output power of 30 mW. The nonlinear crystal used was KTP and the pump source was a hybridly mode-locked dye laser.

Since then several research groups have demonstrated various synchronously pumped OPOs based on different nonlinear crystals and different pumped lasers. Most of the femtosecond OPOs used Ti:sapphire laser as the pump source and the nonlinear crystals used in the OPOs included KTP[18, 20, 21, 24], KTA[22], CTA[25], and RTA[37]. Some picosecond OPOs also used Ti:sapphire laser as a pump source[9, 38]. Nd:YLF and Nd:YAG lasers and their second-harmonic were often used as the pump source for the picosecond OPOs and the nonlinear crystals included KTP[7, 8, 10, 11], KTA[39] and LBO[13, 12, 15]. The OPOs mentioned above covered the spectral range from 800 nm to 3000 nm.

Cheung *et al.* [16] first used  $\text{AgGaS}_2$  as the nonlinear crystal for the OPO and an actively mode-locked Nd:YAG laser as pump source. Due to the large transmission windows of  $\text{AgGaS}_2$ , tunable pulses around 5.5  $\mu\text{m}$  were generated.

OPOs based on CTA[40] and KTP[41] were also demonstrated to produce tunable pulses from 3 to 4  $\mu\text{m}$ . Visible range OPOs were also achieved by using frequency-doubled Ti:sapphire laser pulses as pump source[26, 42] and by using an intracavity-frequency-doubled femtosecond OPO based on RTA[43].

In this report, we present the experimental work to generate wavelength-tunable optical pulses based on a novel picosecond cw mode-locked Nd:YLF laser. This laser can be mode-locked either actively or passively, producing 10 W average power of 30 ps and 6.4 ps pulses, respectively. The passive mode-locking mechanism is additive-pulse mode-locking (APM). Due to the high peak power of these laser pulses, the ultimate goal is to generate optical pulses tunable from visible to mid-infrared by using only one pump source.

## 1.5 Outline of The Report

Because the extensive analysis on the formulations of coupled traveling wave equations using Gaussian beam profile and their transformation to the plane wave equations has been done in Refs. [4] and [5], only a brief summary of the key formulations is presented in section 1.5. Since the previous model did not explicitly consider the temporal effects in the calculation of the OPO gain, the incorporation of the temporal effects into this theory is also presented in section 1.5. A brief theoretical background and the method for maximizing the parametric efficiency using the noncollinear phase matching are also discussed.

The detailed simulations of this theoretical model have been carried out in section 2.5. Special attention is paid to the collinear phase matching geometry since it is most widely used. Simulations on noncollinear phase matching is also



included in section 2.5. The method for the maximization of the parametric efficiency coefficient and the advantages and the limitations of the noncollinear phase matching geometry are also presented with pertinent comparisons of the important parameters in both the collinear and noncollinear phase matching geometries.

In section 3.2.3 the experimental setup and the noise characteristics of the pump laser systems are described. In section 3.2.3 the efforts to produce wavelength-tunable pulses in the range of 10-11  $\mu\text{m}$  from a picosecond  $\text{AgGaS}_2$ -based OPO are presented. In section 3.2.3 the characteristics of a singly resonant OPO synchronously pumped by frequency-doubled APM Nd:YLF laser pulses are described. In section 3.2.3 two different approaches to generate femtosecond pump pulses are presented and discussed. The efforts to produce femtosecond wavelength-tunable pulses are also included. A summary of the results and the possible future research are given as a conclusion in the final section.

## 2.0 Theory of Parametric Gain

In this section, the derivation and formulation of the theory, which contains both spatial and temporal effects, are presented. The effective gain of the parametric process involving ultrashort pulses is derived from this theory. Since the spatial effects have been thoroughly discussed in Ref. [5], the bulk of this section discusses the incorporation of temporal effects to the previous theory. In the following sections, pertinent formulations in the treatment of the spatial effects in Ref. [5] are summarized, and then the extension, which now includes the temporal effects, to the previous theory is thoroughly treated. Additionally, due to recent interest in the effects of noncollinear phase matching conditions on the parametric efficiency, the formulation of optimal parametric efficiency under both collinear and noncollinear phase matching conditions is also given.

### 2.1 Theoretical Approach

Optical parametric oscillation is a special case of difference-frequency generation. In general, the theory of difference-frequency generation parallels that of sum-frequency generation. In fact, difference-frequency generation is considered as an inverse process of sum-frequency generation which is manifested by energy flow from the two lower-frequency fields to the sum frequency field. While difference-frequency generation is initiated by two pump beams of more or less comparable intensities, one at sum-frequency and the other at either of two lower-frequencies, it is also initiated by a single pump beam of strong intensity. There is no definite distinction between these two processes, with the exception of two input conditions described above. In general, the latter is called parametric amplification.

Moreover, if an optical cavity is used, the overall gain of parametric amplification is increased [44]. Then, a coherent output at one of two lower-frequencies can also build up from a noise input and oscillate in an optical cavity. This process, therefore, is called parametric oscillation.

Parametric oscillation is dictated by two fundamental concepts: conservation of energy and phase-matching condition. Conservation of energy is given by,

$$\omega_3 = \omega_1 + \omega_2, \quad (1)$$

with a signal pulse at a central frequency  $\omega_1$  and an idler pulse at  $\omega_2$  by a strong pump pulse at  $\omega_3$ . In difference-frequency mixing, a "pump" at frequency  $\omega_3$  mixes with a "signal" at  $\omega_1$  to generate an "idler" at  $\omega_2 = \omega_3 - \omega_1$ . The phase matching condition is given by,

$$\mathbf{k}_3 = \mathbf{k}_1 + \mathbf{k}_2, \quad (2)$$

where  $\mathbf{k}_1$ ,  $\mathbf{k}_2$ , and  $\mathbf{k}_3$  indicate the wave vectors of the signal, idler, and pump beams, respectively. When the phase mismatch,  $\Delta\mathbf{k} = \mathbf{k}_3 - \mathbf{k}_1 - \mathbf{k}_2$ , is zero, maximum efficiency of the parametric interaction is achieved.

With these two conditions satisfied, we can now discuss the wave equations in the nonlinear media. The parametric interaction of these three pulses in a nonlinear crystal is described by three coupled nonlinear differential equations of the following form,

$$\nabla \times \nabla \times \mathbf{E}_j(\mathbf{r}, t) + \frac{1}{c^2} \frac{\partial^2}{\partial t^2} \mathbf{D}_j(\mathbf{r}, t) = -\frac{4\pi}{c^2} \frac{\partial^2}{\partial t^2} \mathbf{P}_j^{NL}(\mathbf{r}, t) \quad (3)$$

where  $j = 1, 2$ , and  $3$  are for the signal, idler, and pump frequencies, respectively, and the nonlinear polarizations are given by  $\mathbf{P}_1^{NL}(\mathbf{r}, t) = {}^{(2)} : \mathbf{E}_2^*(\mathbf{r}, t) \mathbf{E}_3(\mathbf{r}, t)$ ,  $\mathbf{P}_2^{NL}(\mathbf{r}, t) = {}^{(2)} : \mathbf{E}_1^*(\mathbf{r}, t) \mathbf{E}_3(\mathbf{r}, t)$ , and  $\mathbf{P}_3^{NL}(\mathbf{r}, t) = {}^{(2)} : \mathbf{E}_1(\mathbf{r}, t) \mathbf{E}_2(\mathbf{r}, t)$ .

## 2.2 Spatial Effects

The spatial effects on the parametric efficiency has been thoroughly detailed through a series of analysis and simulations [4, 5]. Therefore, only brief reformulations of the coupled wave equations and the necessary spatial characteristic parameters are presented.

First, to incorporate the spatial effects into equation (3), the complex electric field for frequency  $\omega_j$  is written as:

$$\mathbf{E}_j(\mathbf{r}, t) = \hat{\mathbf{e}}_j \mathcal{E}_j(z, t) \psi_j(\mathbf{r}) \exp(ik_j z - i\omega_j t) \quad (4)$$

where  $\hat{\mathbf{e}}_j$  is the unit vector of the field polarization direction,  $\mathcal{E}_j(z, t)$  is the field envelope of the pulse traveling in the  $z$ -direction,  $\psi_j(\mathbf{r})$  describes the spatial profile of the pulse beam, and  $k_j = \mathbf{k}_j \cdot \hat{\mathbf{z}}$ . As for the spatial profile of the interacting beams, a TEM<sub>00</sub> Gaussian spatial mode is assumed. For the most efficient parametric generation process, the pump beam should have a focused Gaussian profile and the resulting signal and idler beams would also have a Gaussian profile. The TEM<sub>00</sub> Gaussian spatial profiles are written as

$$\psi_j(x, y, z) = \frac{1}{1 + i\xi_j} \exp \left\{ -\frac{[x - \alpha_j(z - f_s)]^2 + y^2}{w_{j0}^2(1 + i\xi_j)} \right\}, \quad (5)$$

where  $f_s$  is the  $z$ -coordinate of the Gaussian beam focus and is assumed to be the same for all three interacting beams for efficient interaction,  $w_{j0}$  and  $\alpha_j$  are the beam waist and the spatial walk-off angle, respectively, of the beam at frequency  $\omega_j$ , and  $\xi_j = 2(z - f_s)/w_{j0}^2 k_j$ . The  $z$ -coordinate has its origin,  $z = 0$ , at the input surface of the nonlinear crystal. The  $z$ -direction is chosen to be the direction of the propagation of  $\mathbf{k}_3$  for mathematical simplicity. As shown in Fig. 2, the angle  $\gamma$  is the angle between the propagation of the wave front, represented by  $\mathbf{k}$ , and the  $z$

axis.  $\varphi$  is the birefringence angle, and  $\alpha$  is the angle between the Poynting vector and the  $z$  axis. Thus the angle  $\alpha = \gamma + \varphi$  describes the walk-off of the beam from the  $z$  axis caused by both double diffraction and noncollinear phase matching [5].

After the substitution of Eqs. (4) and (5) in (3) and some mathematical manipulations, the coupled traveling wave equations under the slowly varying amplitude approximation are obtained

$$\begin{aligned} \left( \frac{\partial}{\partial z} + \frac{1}{v_{g1}} \frac{\partial}{\partial t} + i \frac{D_1}{2\omega_1 c} \frac{\partial^2}{\partial t^2} \right) \mathcal{E}_1(z, t) &= \frac{i2\pi\omega_1^2}{k_1 c^2} \Gamma_{s1}(z) \chi_{eff} \mathcal{E}_2^* \mathcal{E}_3 e^{i\Delta k z}, \\ \left( \frac{\partial}{\partial z} + \frac{1}{v_{g2}} \frac{\partial}{\partial t} + i \frac{D_2}{2\omega_2 c} \frac{\partial^2}{\partial t^2} \right) \mathcal{E}_2(z, t) &= \frac{i2\pi\omega_2^2}{k_2 c^2} \Gamma_{s2}(z) \chi_{eff} \mathcal{E}_1^* \mathcal{E}_3 e^{i\Delta k z}, \\ \left( \frac{\partial}{\partial z} + \frac{1}{v_{g3}} \frac{\partial}{\partial t} + i \frac{D_3}{2\omega_3 c} \frac{\partial^2}{\partial t^2} \right) \mathcal{E}_3(z, t) &= \frac{i2\pi\omega_3^2}{k_3 c^2} \Gamma_{s3}^*(z) \chi_{eff} \mathcal{E}_1 \mathcal{E}_2 e^{-i\Delta k z}, \end{aligned} \quad (6)$$

where  $v_{gj}$  is the group velocity and  $D_j = \omega_j c (d^2 k_j / d\omega_j^2)$  is the dimensionless dispersion coefficient at  $\omega_j$ ,  $\chi_{eff} = \hat{e}_3 \cdot {}^{(2)}(\omega_3 = \omega_1 + \omega_2) : \hat{e}_1 \hat{e}_2$  is the effective nonlinear susceptibility,  $\Delta k = k_3 - k_1 - k_2$  is the phase mismatch, and  $\Gamma_{sj}(z)$  are the spatial beam overlap factors. The dimensionless spatial beam overlap factors are given by

$$\Gamma_{sj}(z) = \frac{\int \int \psi_1^*(\mathbf{r}) \psi_2^*(\mathbf{r}) \psi_3(\mathbf{r}) dx dy}{\cos^2 \alpha_j \int \int \psi_j^*(\mathbf{r}) \psi_j(\mathbf{r}) dx dy} = \frac{w_{30}^2}{w_{j0}^2 \cos^2 \alpha_j} \kappa_s(z) = \frac{\kappa_s(z)}{r_{sj}^2 \cos^2 \alpha_j}, \quad (7)$$

where  $r_{s1} = w_{10}/w_{30}$  and  $r_{s2} = w_{20}/w_{30}$  are the beam-waist ratios of the signal and idler, respectively, to the pump, and

$$\begin{aligned} \kappa_s(z) &= \frac{2r_{s1}^2 r_{s2}^2}{r_{s1}^2 + r_{s2}^2 + r_{s1}^2 r_{s2}^2} \left[ 1 + \frac{(z - f_s)^2}{l_{sb}^2} \right]^{-1/2} \\ &\times \exp \left[ -\frac{(z - f_s)^2}{l_{sw}^2} \frac{1 + (z - f_s)^2 / l_{sb} l_{sc}}{1 + (z - f_s)^2 / l_{sb}^2} + i\phi_s(z) \right]. \end{aligned} \quad (8)$$

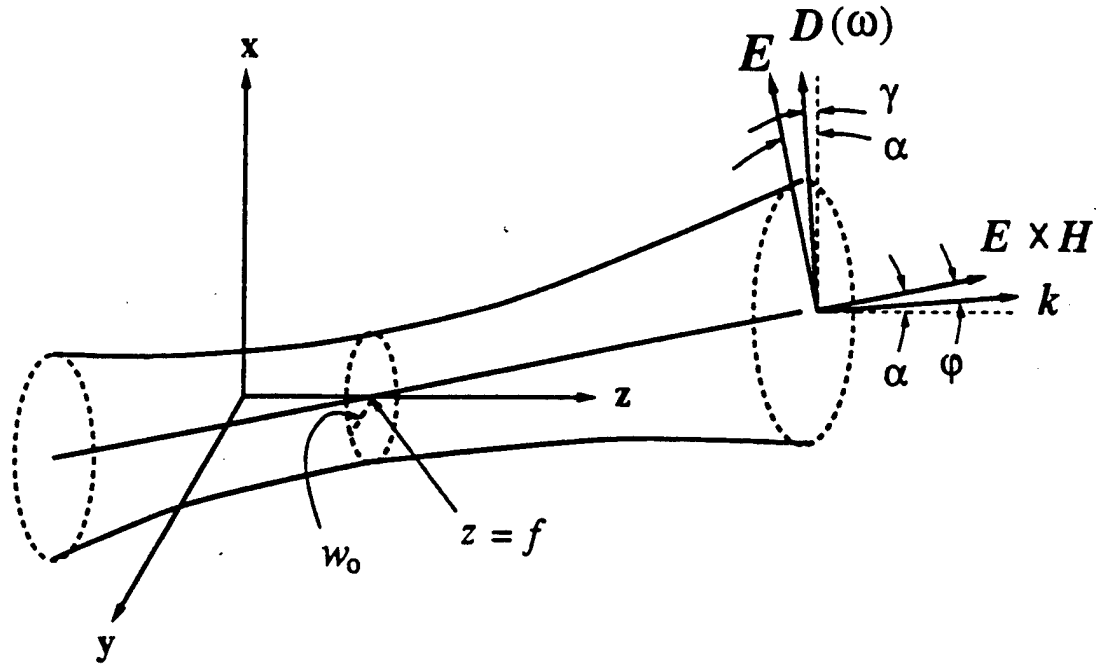


Figure 2: Propagation of an arbitrary beam in an anisotropic medium. The directions of  $\mathbf{E}$ ,  $\mathbf{D}(\omega)$ ,  $\mathbf{E} \times \mathbf{H}$ , and  $\mathbf{k}$  lie in the  $xz$ -plane.

The spatial characteristic lengths in Eq. (8) are defined by

$$l_{sb} = \frac{w_{30}^2}{2} \frac{r_{s1}^2 + r_{s2}^2 + r_{s1}^2 r_{s2}^2}{r_{s1}^2(k_2^{-1} - k_3^{-1}) + r_{s2}^2(k_1^{-1} - k_3^{-1}) + (k_1^{-1} + k_2^{-1})}, \quad (9)$$

$$l_{sc} = \frac{w_{30}^2}{2} \frac{r_{s1}^2(\alpha_2 - \alpha_3)^2 + r_{s2}^2(\alpha_3 - \alpha_1)^2 + (\alpha_1 - \alpha_2)^2}{k_1^{-1}(\alpha_2 - \alpha_3)^2 + k_2^{-1}(\alpha_3 - \alpha_1)^2 - k_3^{-1}(\alpha_1 - \alpha_2)^2}, \quad (10)$$

$$l_{sw} = w_{30} \left[ \frac{r_{s1}^2 + r_{s2}^2 + r_{s1}^2 r_{s2}^2}{r_{s1}^2(\alpha_2 - \alpha_3)^2 + r_{s2}^2(\alpha_3 - \alpha_1)^2 + (\alpha_1 - \alpha_2)^2} \right]^{1/2}, \quad (11)$$

and the phase  $\phi_s(z)$  is given by

$$\phi_s(z) = \frac{l_{sb} - l_{sc}}{l_{sb} l_{sc} l_{sw}^2} \frac{(z - f_s)^3}{1 + (z - f_s)^2 / l_{sb}^2} + \tan^{-1} \frac{z - f_s}{l_{sb}}. \quad (12)$$

Each of these spatial characteristic lengths has very clear physical meaning:  $l_{sb}$  is a length parameter characterizing the effect of spatial beam broadening due to diffraction;  $l_{sw}$  is the aperture length due to spatial walk-off; and  $l_{sc}$  is a characteristic length of the combined effect of beam broadening and beam walk-off. Note that  $l_{sb}$  and  $l_{sc}$  can be either positive or negative, but  $l_{sw}$  is always positive.

### 2.3 Temporal Effects

In the previous theoretical analyses in Refs. [4] and [5], the time-dependent characteristics of the parametric pulses are kept explicit until the final master differential equation describing the OPO. This is done by keeping the time-derivative terms containing  $v_{gj}$  and  $D_j$  in Eq. (6) in the operator form to arrive at a time-dependent gain containing time-derivative operators [4]. The advantage of this approach is that the temporal characteristics of the pulses can be studied in detail, as the simulation results in Ref. [4] show. The disadvantage is that no simple evaluation of

the temporal effects is possible without a full simulation of the master differential equation, as mentioned in the preceding section. The objective here is to include the temporal effects in the formulation of an effective gain coefficient which can be evaluated without solving the master differential equation. The strategy is to remove the time-derivative terms in Eq. (6) by integrating them out before proceeding further in the calculation of the effective gain. By doing so, we trade our ability of simulating the detailed temporal characteristics of the parametric pulse for an ability to evaluate both the spatial and the temporal effects in combination through an effective gain coefficient.

To integrate out the time-derivative terms in Eq. (6), we recognize that the left-hand side of these equations has the form of a complex diffusion equation, or Schrödinger-like equation. Its eigenfunction solutions are a series of Hermite-Gaussian functions. Therefore, the pulse envelope  $\mathcal{E}_j(z, t)$  can be expanded in terms of these Hermite-Gaussian eigenfunctions. Normally the field envelope of the pump pulse has a temporal shape of either Gaussian or hyperbolic secant. Since a hyperbolic secant function can be closely approximated with a fundamental Gaussian, only the fundamental Gaussian term is needed for the expansion of the pump pulse envelope in the first-order approximation. With such a pump pulse, the signal and idler pulses all have single dominant temporal peaks which can also be approximated by the fundamental Gaussian in the first-order approximation. This can be seen from the temporal characteristics obtained through simulations in Ref. [4] and can be understood from the fact that the parametric interaction is a nonlinear process which favors energy conversion at the peak of high field intensities.



The fundamental Gaussian solutions for the temporal pulse characteristics have the following form

$$h_j(z, t) = \frac{1}{(1 - i\eta_j)^{1/2}} \exp \left\{ -2 \ln 2 \frac{[t - (z - f_t)]/v_{gj}]^2}{\Delta t_{j0}^2 (1 - i\eta_j)} \right\}, \quad (13)$$

where  $\Delta t_{j0}$  is the full-width at half-maximum temporal pulsewidth for the pulse at frequency  $\omega_j$  and  $\eta_j = (4 \ln 2) D_j z / \omega_j c \Delta t_{j0}^2$ . The parameter  $f_t$  is the  $z$ -coordinate of the location where the peaks of the pulses overlap. It depends on the synchronization of the input pump and signal pulses and can be adjusted experimentally with an external delay line or, in the case of a synchronously pumped OPO, by fine-tuning the cavity length. It has a meaning analogous to the spatial overlap of the beam waists defined by  $f_s$  in Eq. (5). However, in the spatial case, the parameters  $w_{j0}$ 's are the beam waists measured right at the common focal location at  $z = f_s$ . In the temporal case, the pulsewidths that can serve as good reference are the ones at the input surface of the nonlinear crystal because a pulse starts changing its pulsewidth once it enters the crystal and the change depends on many case-specific parameters. For this reason, we take  $\Delta t_{j0}$ 's to be the input pulsewidths at  $z = 0$  rather than those at  $z = f_t$ . This explains why  $\xi_j$  in Eq. (5) is a function of  $z - f_s$  while  $\eta_j$  in Eq. (13) is a function of  $z$  alone.

Therefore, the pulse envelope is written as

$$\mathcal{E}_j(z, t) = \mathcal{A}_j(z) h_j(z, t), \quad (14)$$

where the complex amplitude  $\mathcal{A}_j(z)$  retains the dimension of the electric field, as do  $\mathcal{E}_j$  and  $\mathbf{E}_j$ . Substitution of Eqs. (13) and (14) in (6) yields

$$\frac{\partial \mathcal{A}_1(z)}{\partial z} = \frac{i 2 \pi \omega_1^2}{k_1 c^2} \Gamma_1(z) \chi_{\text{eff}} \mathcal{A}_2^*(z) \mathcal{A}_3(z) e^{i \Delta k z},$$

$$\frac{\partial \mathcal{A}_2(z)}{\partial z} = \frac{i2\pi\omega_2^2}{k_2 c^2} \Gamma_2(z) \chi_{\text{eff}} \mathcal{A}_1^*(z) \mathcal{A}_3(z) e^{i\Delta k z}, \quad (15)$$

$$\frac{\partial \mathcal{A}_3(z)}{\partial z} = \frac{i2\pi\omega_3^2}{k_3 c^2} \Gamma_3^*(z) \chi_{\text{eff}} \mathcal{A}_1(z) \mathcal{A}_2(z) e^{-i\Delta k z},$$

where the total overlap factors  $\Gamma_j(z)$ 's are dimensionless and contain both spatial and temporal effects

$$\Gamma_j(z) = \Gamma_{sj}(z) \Gamma_{tj}(z). \quad (16)$$

The temporal pulse overlap factors are given by

$$\Gamma_{tj}(z) = \frac{\int_{-\infty}^{\infty} h_1^*(z, t) h_2^*(z, t) h_3(z, t) dt}{\int_{-\infty}^{\infty} h_j^*(z, t) h_j(z, t) dt} = \frac{\Delta t_{30}}{\Delta t_{j0}} \kappa_t(z) = \frac{\kappa_t(z)}{r_{tj}}, \quad (17)$$

where  $r_{t1} = \Delta t_{10}/\Delta t_{30}$  and  $r_{t2} = \Delta t_{20}/\Delta t_{30}$  are the pulsewidth ratios of the signal and the idler, respectively, to the pump, and

$$\kappa_t(z) = \frac{2^{1/2} r_{t1} r_{t2}}{(r_{t1}^2 + r_{t2}^2 + r_{t1}^2 r_{t2}^2)^{1/2}} \left(1 + \frac{z^2}{l_{tb}^2}\right)^{-1/4} \exp \left[ -\frac{(z - f_t)^2}{l_{tw}^2} \frac{1 + z^2/l_{tb} l_{tc}}{1 + z^2/l_{tb}^2} + i\phi_t(z) \right]. \quad (18)$$

The temporal characteristic lengths in Eq. (18) are defined by

$$l_{tb} = \frac{\Delta t_{30}^2}{4 \ln 2} \frac{r_{t1}^2 + r_{t2}^2 + r_{t1}^2 r_{t2}^2}{r_{t1}^2 (\tilde{D}_2 - \tilde{D}_3) + r_{t2}^2 (\tilde{D}_1 - \tilde{D}_3) + (\tilde{D}_1 + \tilde{D}_2)}, \quad (19)$$

$$l_{tc} = \frac{\Delta t_{30}^2}{4 \ln 2} \frac{r_{t1}^2 (N_2 - N_3)^2 + r_{t2}^2 (N_3 - N_1)^2 + (N_1 - N_2)^2}{\tilde{D}_1 (N_2 - N_3)^2 + \tilde{D}_2 (N_3 - N_1)^2 - \tilde{D}_3 (N_1 - N_2)^2}, \quad (20)$$

$$l_{tw} = \frac{c \Delta t_{30}}{(2 \ln 2)^{1/2}} \left[ \frac{r_{t1}^2 + r_{t2}^2 + r_{t1}^2 r_{t2}^2}{r_{t1}^2 (N_2 - N_3)^2 + r_{t2}^2 (N_3 - N_1)^2 + (N_1 - N_2)^2} \right]^{1/2}, \quad (21)$$

where  $\tilde{D}_j = D_j/\omega_j c = d^2 k_j/d\omega_j^2$  and the group index  $N_j = c/v_{gj} = n_j - \omega_j (dn_j/d\omega_j)$ .

The phase  $\phi_t(z)$  is given by

$$\phi_t(z) = -\frac{l_{tb} - l_{tc}}{l_{tb} l_{tc} l_{tw}^2} \frac{z(z - f_t)^2}{1 + z^2/l_{tb}^2} - \frac{1}{2} \tan^{-1} \frac{z}{l_{tb}}. \quad (22)$$

Each of the temporal characteristic lengths also has clear physical meaning in analogy to its spatial counterpart:  $l_{tb}$  is the length characterizing the effect of temporal pulse broadening due to group-velocity dispersion;  $l_{tw}$  is the temporal aperture length due to temporal pulse walk-off; and  $l_{tc}$  is a characteristic length of the combined effect of pulse broadening and pulse walk-off. Similar to their spatial counterparts,  $l_{tb}$  and  $l_{tc}$  can also be positive or negative while  $l_{tw}$  is always positive.

In Eq. (15), the temporal characteristics of the pulses have been integrated and their effects accounted for by the  $\Gamma_{tj}$  factors. Therefore, the parameter to be used in evaluating the gain in the following is the pulse energy rather than intensity or power used in Refs. [4] and [5], respectively. The energy of pulse  $j$  at the location  $z$  is given by

$$\mathcal{U}_j(z) = \int_{-\infty}^{\infty} P_j(z, t) dt = \left( \frac{\pi}{4 \ln 2} \right)^{1/2} \frac{c^2 k_j w_{j0}^2 \cos^2 \alpha_j}{4 \omega_j} \Delta t_{j0} |\mathcal{A}_j(z)|^2, \quad (23)$$

where  $w_j(z) = w_{j0}(1 + \xi_j^2)^{1/2}$  and  $\Delta t_j(z) = \Delta t_{j0}(1 + \eta_j^2)^{1/2}$ . The total energy of the three interacting pulses is conserved:

$$\mathcal{U} = \mathcal{U}_1(z) + \mathcal{U}_2(z) + \mathcal{U}_3(z). \quad (24)$$

## 2.4 Effective Gain

Following a procedure similar to that taken in Ref. [5], Eq. (15) can be solved by first defining  $u_j$  and  $\phi_j$  with

$$\mathcal{A}_j(z) = \left( \frac{4 \ln 2}{\pi} \right)^{1/4} \left( \frac{4\omega_j^2 \mathcal{U}}{c^2 k_j w_{j0}^2 \cos^2 \alpha_j \Delta t_{j0}} \right)^{1/2} u_j(z) e^{i\phi_j(z)}, \quad (25)$$

and then making the following change of variable

$$\begin{aligned} \zeta &= \frac{4\pi}{c^3} \left( \frac{4 \ln 2}{\pi} \right)^{1/4} \left( \frac{\mathcal{U}}{k_1 k_2 k_3} \right)^{1/2} \\ &\times \frac{\omega_1 \omega_2 \omega_3 \chi_{\text{eff}}}{w_{30} \Delta t_{30}^{1/2} r_{s1} r_{s2} r_{t1}^{1/2} r_{t2}^{1/2} \cos \alpha_1 \cos \alpha_2 \cos \alpha_3} \int_0^z |\kappa_s(z) \kappa_t(z)| dz. \end{aligned} \quad (26)$$

Then, Eq. (15) can be transformed to the following equations

$$\begin{aligned} \frac{du_1}{d\zeta} &= -u_2 u_3 \sin \theta, \\ \frac{du_2}{d\zeta} &= -u_3 u_1 \sin \theta, \\ \frac{du_3}{d\zeta} &= u_1 u_2 \sin \theta, \end{aligned} \quad (27)$$

and

$$\begin{aligned} \frac{d\phi_1}{d\zeta} &= \frac{u_2 u_3}{u_1} \cos \theta, \\ \frac{d\phi_2}{d\zeta} &= \frac{u_3 u_1}{u_2} \cos \theta, \\ \frac{d\phi_3}{d\zeta} &= \frac{u_1 u_2}{u_3} \cos \theta, \end{aligned} \quad (28)$$

where

$$\theta = \Delta k z + \phi_s(z) + \phi_t(z) + \phi_3(z) - \phi_1(z) - \phi_2(z), \quad (29)$$

which satisfies

$$\frac{d\theta}{d\zeta} = \left[ \Delta k + \frac{d\phi_s(z)}{dz} + \frac{d\phi_t(z)}{dz} \right] \frac{dz}{d\zeta} + \cot \theta \frac{d \ln(u_1 u_2 u_3)}{d\zeta}. \quad (30)$$

Exact analytical solutions in terms of elliptic functions can be obtained for  $u_j$  and  $\phi_j$ . This has been discussed in Ref. [4]. For our purpose here, we consider the most efficient case of exact phase matching with input  $\mathcal{U}_3(0) = \mathcal{U}_3$ ,  $\mathcal{U}_1(0) = \mathcal{U}_1$ , but  $\mathcal{U}_2(0) = 0$ . This yields the following solution for the signal

$$\begin{aligned} u_1(\zeta) &= u_1(0) \text{cn} \left[ i u_3(0) \zeta, i \frac{u_1(0)}{u_3(0)} \right] \\ &\approx u_1(0) \left( 1 + \frac{1}{2} u_3^2(0) \zeta^2 + \frac{1}{24} u_3^4(0) \zeta^4 - \frac{1}{6} u_1^2(0) u_3^2(0) \zeta^4 \right). \end{aligned} \quad (31)$$

For a crystal length  $l_c$ , the single-pass effective field gain is

$$G_{\text{eff}} = \frac{u_1(\zeta_c) - u_1(0)}{u_1(0)} = b \mathcal{U}_3 + \frac{1}{6} b^2 \mathcal{U}_3^2 - \frac{2\omega_3}{3\omega_1} b^2 \mathcal{U}_1 \mathcal{U}_3 \quad (32)$$

where  $\zeta_c = \zeta(l_c)$ . In Eq. (32), the first term,  $b \mathcal{U}_3$ , is the small signal gain and the third term represents gain saturation. The  $b$  coefficient is given by

$$b = \frac{a' l_{\text{eff}}^2}{w_{\text{eff}}^2 \Delta t_{\text{eff}}}, \quad (33)$$

where

$$a' = \frac{4\pi^3 \omega_1^2 \omega_2^2 \omega_3}{k_1 k_2 k_3 c^6} \chi_{\text{eff}}^2, \quad (34)$$

$$\frac{1}{w_{\text{eff}}^2} = \frac{8}{\pi} \frac{1}{w_{30}^2 \cos^2 \alpha_1 \cos^2 \alpha_2 \cos^2 \alpha_3} \frac{r_{s1}^2 r_{s2}^2}{(r_{s1}^2 + r_{s2}^2 + r_{s1}^2 r_{s2}^2)^2}, \quad (35)$$

$$\frac{1}{\Delta t_{\text{eff}}} = \left( \frac{8}{\pi} \right)^{1/2} \frac{(2 \ln 2)^{1/2}}{\Delta t_{30}} \frac{r_{t1} r_{t2}}{r_{t1}^2 + r_{t2}^2 + r_{t1}^2 r_{t2}^2}, \quad (36)$$

and

$$l_{\text{eff}} = \int_0^{l_c} \left[ 1 + \frac{(z - f_s)^2}{l_{sb}^2} \right]^{-1/2} \exp \left[ -\frac{(z - f_s)^2}{l_{sw}^2} \frac{1 + (z - f_s)^2/l_{sb}l_{sc}}{1 + (z - f_s)^2/l_{sb}^2} \right] \\ \times \left( 1 + \frac{z^2}{l_{tb}^2} \right)^{-1/4} \exp \left[ -\frac{(z - f_t)^2}{l_{tw}^2} \frac{1 + z^2/l_{tb}l_{tc}}{1 + z^2/l_{tb}^2} \right] dz. \quad (37)$$

The effective field gain  $G_{\text{eff}}$  is a dimensionless quantity which measures the amplification of the field magnitude of the signal pulse through the parametric process. It can be seen from Eq. (32) that the  $b$  coefficient is the key parameter which determines the efficiency of the parametric interaction. It is thus called the parametric efficiency coefficient. The quantity  $1/b$  has the dimension of energy and corresponds to the pump pulse energy required to have a small-signal gain of 100%. One can see from Eq. (33) that the  $b$  coefficient contains all the spatial and temporal effects of parametric interaction because the effective interaction length,  $l_{\text{eff}}$ , is determined by the six characteristic lengths, three spatial and three temporal. When the crystal length exceeds a particular characteristic length, the corresponding effect responsible for that characteristic length becomes important in limiting the efficiency of the parametric interaction, thus setting a limit for the useful effective length. If more than one characteristic length is shorter than  $l_c$ , the effective interaction length is limited by a combination of the effects behind those characteristic lengths.

In a cw synchronously pumped OPO with a total round-trip electric field loss  $L$  in the cavity,  $G_{\text{eff}}$  can be used to estimate the threshold pump pulse energy for oscillation by setting the small signal gain equal to the loss to have

$$\mathcal{U}_3^{\text{threshold}} = \frac{L}{b}. \quad (38)$$

For pumping not too high above threshold,  $G_{\text{eff}} = L$  when the OPO reaches its steady state. This can be used to roughly estimate the energy of the signal pulse in the cavity,

$$\mathcal{U}_1 \approx \frac{2\omega_1}{3\omega_3} \frac{1}{b} \left( 1 + \frac{b\mathcal{U}_3}{6} - \frac{L}{b\mathcal{U}_3} \right), \quad (39)$$

and the output signal-pulse energy,

$$\mathcal{U}_s = (1 - R_2)\mathcal{U}_1, \quad (40)$$

where  $R_2$  is the reflectivity of the output coupling mirror.

The results obtained here can also be applied to parametric amplification or difference frequency generation of ultrashort pulses without a resonant cavity. For parametric amplification, the single-pass amplification factor of the signal-pulse energy is given by

$$A_s = \frac{u_1^2(\zeta_c)}{u_1^2(0)} = (1 + G_{\text{eff}})^2. \quad (41)$$

For difference-frequency generation, the desired output is the idler pulse at  $\omega_2$ . Its energy at the output is given by

$$\mathcal{U}_2(l_c) = \frac{\omega_2}{\omega_1} [\mathcal{U}_1(l_c) - \mathcal{U}_1(0)] = \frac{\omega_2}{\omega_1} G_{\text{eff}} (2 + G_{\text{eff}}) \mathcal{U}_1. \quad (42)$$

## 2.5 Noncollinear Phase Matching

When considering OPO systems, there are two possible phase-matching geometries used in an experimental condition: collinear and noncollinear phase-matching. Out of these two possible geometries, the more often used configuration is collinear phase-matching geometry for it is simpler. However, simplicity does not necessarily mean efficiency because noncollinear phase matching may increase the parametric

efficiency under certain experimental conditions. One way to increase the parametric efficiency under noncollinear phase-matching conditions is the reduction of walk-off in anisotropic crystals. This reduction of walk-off will increase the value of  $l_{sw}$ ; as a result, the value of  $l_{eff}$  will also increase. Consequently, the value of  $b$  will increase. To reduce walk-off, Wachman *et al.* [18] collinearly aligned the Poynting vectors of the pump and signal waves. Subsequent experiments [21, 22, 23] followed using a similar approach and the increase in parametric efficiency was observed. However, for many phase matching geometries in nonlinear crystals, when the Poynting vectors of the pump and signal waves are collinear, the Poynting vector of the idler wave also walks off. To achieve maximum parametric interaction, all three Poynting vectors should ideally be overlapping with one another.

Although some theoretical treatment of noncollinear phase matching and the parametric efficiency has been performed [45, 46, 47], none compares the effects of various experimental conditions, such as the crystal length, phase matching angle, the beam waists, and the pulsewidths, on the parametric efficiency. Many experiments have shown that noncollinear phase matching in parametric generation increases the efficiency and reduces the operational threshold [48, 49, 50, 51, 52, 53]. For example, Gloster *et al.* [51] reports, for Type I phase matching in a BBO OPO pumped by the third harmonic of a Q-switched Nd:YAG laser, the optical conversion efficiency increased from 10.7% in the collinear case to 40% in the noncollinear case. In this section, we briefly review the underlying theory of noncollinear phase matching and propose a method for finding a set of conditions for optimal parametric efficiency.

For electromagnetic waves traveling through an anisotropic medium, such as a



nonlinear crystal, the waves have two types of polarizations: ordinary and extraordinary. For a wave propagating along  $\hat{k}$  in a uniaxial crystal with the optical axis  $\hat{z}$ , the directions of the polarization of the ordinary and extraordinary waves are defined as

$$\hat{e}_o = \hat{k} \times \hat{z} \quad \text{and} \quad \hat{e}_e = \hat{k} \times \hat{e}_o, \quad (43)$$

respectively. If the vector  $\hat{k}$  is in a direction which is at an angle  $\theta$  with respect to the axis  $\hat{z}$  and an angle  $\phi$  with respect to the axis  $\hat{x}$ , then we have

$$\hat{k} = \hat{x} \sin \theta \cos \phi + \hat{y} \sin \theta \sin \phi + \hat{z} \cos \theta, \quad (44)$$

$$\hat{e}_o = \hat{x} \sin \phi - \hat{y} \cos \phi, \quad (45)$$

$$\hat{e}_e = -\hat{x} \cos \theta \cos \phi - \hat{y} \cos \theta \sin \phi + \hat{z} \sin \theta. \quad (46)$$

While the Poynting vector, represented by  $\mathbf{S}_j$ , of the ordinary wave is parallel to the wave vector,  $\mathbf{k}_j$ , that of the extraordinary wave is not parallel to the wave vector. Collinear phase-matching is achieved when three wave vectors,  $\mathbf{k}_1$ ,  $\mathbf{k}_2$ , and  $\mathbf{k}_3$ , are collinear. However, this collinearity of the wave vectors does not lead to the collinearity of three Poynting vectors,  $\mathbf{S}_1$ ,  $\mathbf{S}_2$ , and  $\mathbf{S}_3$ . Insufficient overlapping of the Poynting vectors, as a result, is assumed to lead to lower parametric efficiency. On the contrary, in noncollinear phase-matching,  $\mathbf{k}_j$ 's are not aligned collinearly, therefore one may be able to "align" the Poynting vectors close to each other for better parametric interactions, thus producing higher parametric efficiency. Regardless of the phase-matching geometry, the fundamental constraints for the parametric process given in Eqs. (1) and (2) must be satisfied at all times.

To further clarify and investigate this concept, we consider the parametric interaction in a most widely used nonlinear crystal, KTP. To compare the effects

of collinear and noncollinear phase matching, we choose a representative case of Type II phase matching,  $o \rightarrow e + o$  for  $\omega_3 \rightarrow \omega_1 + \omega_2$ . In this configuration, the pump and idler waves are polarized in the crystal  $y$ -direction and the signal wave is polarized in the  $zx$ -plane. As mentioned before, the crystal axes are defined as  $\hat{x}$ ,  $\hat{y}$ , and  $\hat{z}$ . Therefore, for the phase matching configuration considered in the analysis,  $\phi = 0^\circ$  and  $\chi_{\text{eff}} = \chi_{24} \sin \theta$ . Since a counterpart system,  $o \rightarrow o + e$  interaction, follows the same type of analysis, we limit our discussions only to the former case.

First, we consider the collinear phase matching case, which is schematically shown in Fig. 3. Any angle shown in Fig. 3 is defined positive in the counterclockwise direction.  $\theta_j$  is defined as an angle from the crystal axis  $\hat{z}$  to the respective wave vector  $\mathbf{k}_j$ , where the subscripts 1, 2, and 3 indicate the signal, idler, and pump, respectively. The definitions of  $\varphi_j$  and  $\alpha_j$  are those defined in section 2.2. As we mentioned previously, Eqs. (1) and (2) must always be satisfied. Rewriting in terms of wavelengths and indices of refraction,  $\lambda_j$ 's and  $n_j$ 's, respectively; they have the following form:

$$\frac{1}{\lambda_3} = \frac{1}{\lambda_1} + \frac{1}{\lambda_2} \quad (47)$$

and

$$\frac{n_3}{\lambda_3} = \frac{n_1}{\lambda_1} + \frac{n_2}{\lambda_2}. \quad (48)$$

Since the pump and idler waves are ordinary, their indices of refraction are easily calculated from the Sellmeier's equation given in Ref. [5]. However, for the extraordinary signal wave, the index of refraction is a function of the phase matching angle  $\theta_c$ , which is defined as the angle between the three collinear wave vectors

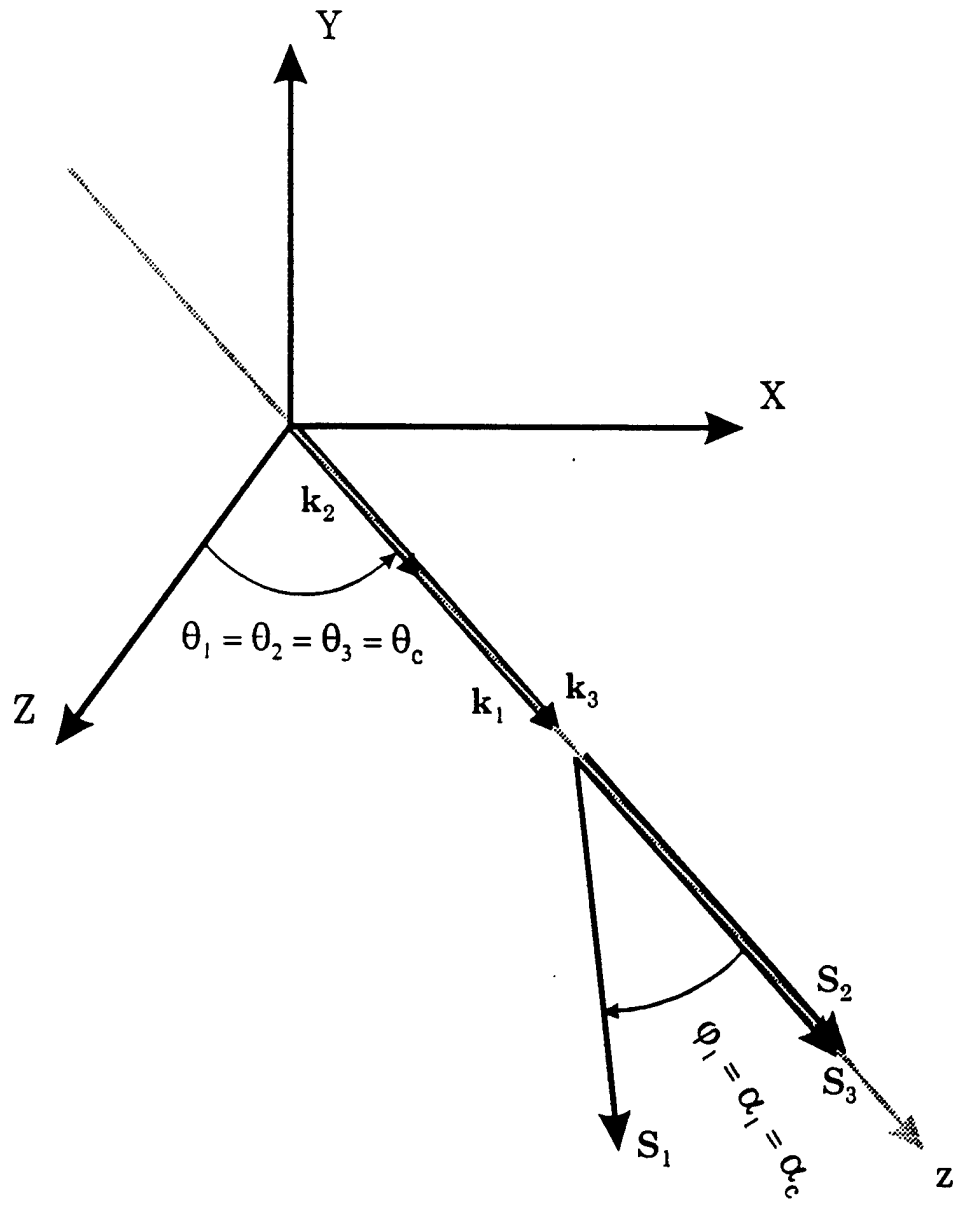


Figure 3: Schematic diagram of the collinear phase matching in KTP.

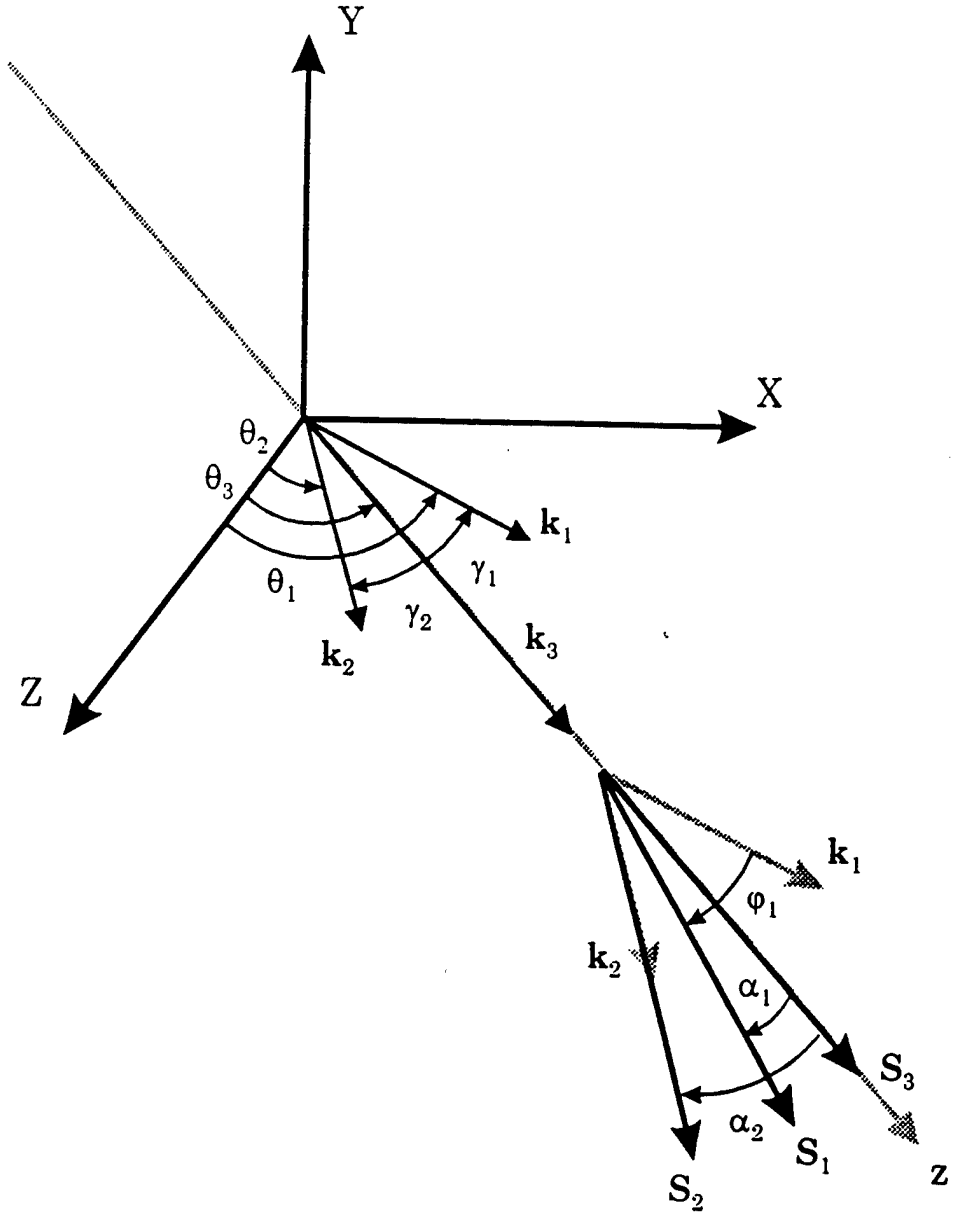


Figure 4: Schematic diagram of the noncollinear phase matching in KTP.

and the optical axis  $\hat{z}$ . Now Eq. (48) becomes

$$\frac{n_o(\lambda_3)}{\lambda_3} = \frac{n_e(\theta_c, \lambda_1)}{\lambda_1} + \frac{n_o(\lambda_2)}{\lambda_2} \quad (49)$$

where the subscripts  $o$  and  $e$  represent ordinary and extraordinary, respectively,  $n_o$  is the index of refraction along the  $\hat{y}$  crystal axis with corresponding wavelengths, and  $n_e$  is given by

$$n_e(\theta_c, \lambda_1) = \left[ \frac{1}{n_z^2} + \cos^2 \theta_c \left( \frac{1}{n_x^2} - \frac{1}{n_z^2} \right) \right]^{-1/2}. \quad (50)$$

Note that for collinear phase matching,  $\theta_1 = \theta_2 = \theta_3 = \theta_c$  where  $\theta_c$  is defined as collinear phase matching angle. As shown in Fig. 3, the Poynting vectors,  $\mathbf{S}_3$  and  $\mathbf{S}_2$ , for the pump and idler are collinear while the Poynting vector,  $\mathbf{S}_1$ , for the signal wave has deviated toward  $\hat{z}$  due to the birefringence of the nonlinear crystal. Again, invoking the definition of  $\alpha_j$  in section 2.2, we find that  $\gamma_1 = \gamma_2 = \gamma_3 = 0$  and  $\varphi_2 = \varphi_3 = 0$ . Since the signal wave is extraordinary,  $\varphi_1 \neq 0$  and  $\varphi_1$  is given by

$$\varphi_1 = \theta_c - \tan^{-1} \left( \frac{n_{x1}^2}{n_{z1}^2} \tan \theta_c \right). \quad (51)$$

This means that, for the collinear phase matching case, the angles of walk-off are:  $\alpha_1 = \varphi_1$  and  $\alpha_2 = \alpha_3 = 0$ . The walk-off angle  $\alpha_1$  is plotted in Fig. 5 (b). Note that as the phase-matching angle nears  $90^\circ$ , the noncritical phase matching angle, the walk off angle approaches zero.

Now we consider the noncollinear phase matching case. As shown in Fig. 4,  $\gamma_1$  and  $\gamma_2$  are no longer zero and have positive or negative values depending on their directions. KTP is a biaxial crystal with  $mm2$  symmetry. Since the values of  $n_x$  and  $n_y$  are very close to each other, we will assume KTP an uniaxial crystal for our analysis. Since we are considering a positive "uniaxial" KTP, we choose  $\gamma_1$  to

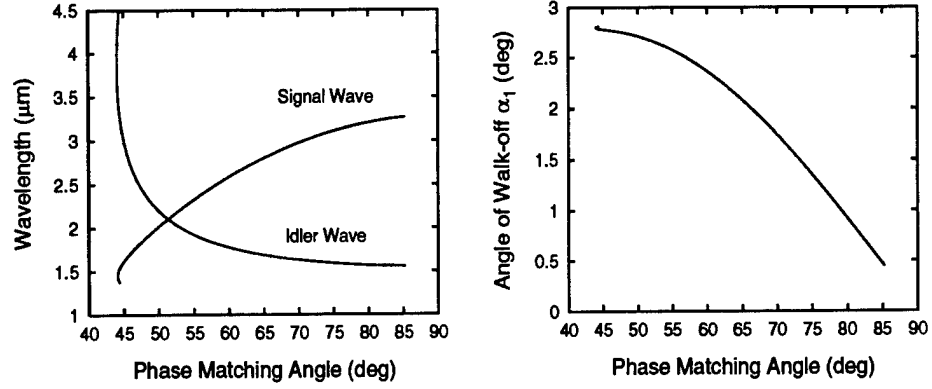


Figure 5: Phase matching angle and the angle of walkoff for  $\lambda_3 = 1.053 \mu\text{m}$ .

have positive values. With the phase matching directions and conditions we have described above,  $S_1$  will move closer to  $S_2$  and  $S_3$  for positive  $\gamma_1$  but will move away for negative  $\gamma_1$ . Therefore, for nonzero values of  $\gamma_1$  and  $\gamma_2$ , Eq. (49) has to be modified to include geometrical constraints producing this set of two equations to be satisfied

$$\frac{n_o(\lambda_3)}{\lambda_3} = \frac{n_e(\theta_1, \lambda_1)}{\lambda_1} \cos \gamma_1 + \frac{n_o(\lambda_2)}{\lambda_2} \cos \gamma_2 \quad (52)$$

$$\frac{n_e(\theta_1, \lambda_1)}{\lambda_1} \sin \gamma_1 + \frac{n_o(\lambda_2)}{\lambda_2} \sin \gamma_2 = 0. \quad (53)$$

As we mentioned earlier, the effective gain,  $G_{\text{eff}}$ , largely depends on the value of  $l_{\text{eff}}$ , whose value in turn largely depends on the six characteristic length parameters,  $l_{sb}$ ,  $l_{sc}$ ,  $l_{sw}$ ,  $l_{tb}$ ,  $l_{tc}$ , and  $l_{tw}$ . Out of these length parameters, when the spatial effects are dominant over the temporal ones,  $l_{sw}$  becomes the most important parameter in determining the value of  $l_{\text{eff}}$ . As we can see in Eq. (11), the value of  $l_{sw}$  is mostly affected by the relative deviation of any pair of  $\alpha_j$ 's. Therefore, to maximize  $l_{sw}$ , we only need to find a set of  $\alpha_j$ 's, which satisfy Eqs. (1) and (2), that produce the maximum  $l_{sw}$ . The maximization of  $l_{sw}$  leads to the maximization of  $l_{\text{eff}}$ ; therefore, the maximum value of  $l_{sw}$  is directly related to the maximization of the parametric

efficiency. The details of a numerical simulation are fully discussed in section 3.0.

## 3.0 Numerical Simulation

### 3.1 Collinear Phase Matching

In this section, we present numerical results to demonstrate the concepts derived from the preceding theoretical analysis and to get a quantitative sense of the key parameters. For this purpose, we choose a few practically meaningful values for each experimental parameter to show how the spatial and temporal effects vary and what influence they have on the effective gain of the parametric interaction.

We consider the parametric interaction in a KTP crystal with pump pulse at three different pump wavelengths: the fundamental of the Nd:YLF laser at  $1.053 \mu\text{m}$ , its second harmonic at  $527 \text{ nm}$ , and the spectral center of the Ti:sapphire laser at  $780 \text{ nm}$ . The  $o \rightarrow o + e$  phase matching for  $\omega_3 \rightarrow \omega_1 + \omega_2$  with pump and signal polarized in the crystal  $y$ -direction and idler polarized in the  $zx$ -plane is considered. Alternatively, if the roles of signal and idler are exchanged, the same condition applies to  $o \rightarrow e + o$  phase matching with pump and idler polarized in the  $y$ -direction and signal polarized in the  $zx$ -plane. For both cases, we have  $\phi = 0^\circ$  and  $\chi_{\text{eff}} = \chi_{24} \sin \theta$ . Therefore, the responsible nonlinear coefficient is  $\chi_{24}$ , or  $d_{24}$ . Recent measurement of  $d_{24}$  yielded values of  $3.3 \text{ pm/V}$  [54],  $3.64 \text{ pm/V}$  [55], and  $4.1 \text{ pm/V} \pm 10\%$  [16] at  $1.064 \mu\text{m}$  wavelength, which are all lower than the previously reported value of  $7.6 \text{ pm/V}$  [5]. In the following calculations, we take  $d_{24} = 3.64 \text{ pm/V}$  for  $\lambda_3 = 1.053 \mu\text{m}$  and use the Miller's rule to account for its dispersion at other wavelengths. For the principal indices of refraction, we use the Sellmeier equation with the coefficients given in Ref. [5]. They are used to calculate the group indices and the group-velocity dispersion coefficients,



as well as the phase-matching angles, in each case. In Appendix A, the values of these characteristic parameters are plotted with respect to the wavelength for easy look-up reference. With the three different pump wavelengths and with the signal and idler wavelengths extending to the long-wavelength end of the transmission window of KTP, we will be considering a combined spectral range from 527 nm to 4.5  $\mu\text{m}$ .

For calculations that require specification of the pulse beam parameters, two representative pump beam waist sizes of  $w_{30} = 100$  and 20  $\mu\text{m}$  and three representative input pump pulsewidths of  $\Delta t_{30} = 5$  ps, 500 fs, and 50 fs are considered for each pump wavelength. When the specification of crystal length is necessary, such as in the calculation of the parametric efficiency coefficient, we consider three representative crystal lengths of  $l_c = 1, 5,$  and 10 mm. Since the spatial effects have been discussed in great detail in Ref. [5], the consideration here on the spatial effects focuses mainly on their contrast to and interplay with the temporal effects. To reduce the number of free parameters, we consider only the case when  $r_{s1} = r_{s2} = 1$  and  $r_{t1} = r_{t2} = 1$ . This allows us to keep the amount of data at a manageable level without missing the key features of the various characteristics to be discussed.

### 3.1.1 Beam and Pulse Broadening

Both spatial and temporal effects contribute to parametric interaction among ultrashort pulses through broadening and walk-off. The actual impact on the parametric gain is determined by the combination of these effects characterized by the six characteristic lengths. To gain a very intuitive appreciation of the importance

of spatial and temporal broadening effects and to serve for later reference, we show in Fig. 6(a) and (b) the percentage of spatial and temporal broadening, respectively, as a function of wavelength for focused pulse beams of different beam waist sizes and different pulsewidths, after they travel 5 mm through a KTP crystal with their fields polarized along one of the three principal axes of KTP. A beam at 4  $\mu\text{m}$  wavelength focused to 20  $\mu\text{m}$  at the beam waist diverges very quickly and broadens about 10 times over 5 mm in KTP while the broadening of a less-focused beam with a beam waist of 100  $\mu\text{m}$  is broadened by less than 9% over the same distance. In contrast, a nonchirped pulse of 500 fs full-width at half-maximum pulsewidth suffers less than 0.5% broadening over 5 mm in KTP while substantial broadening is observed at both ends of the spectrum for a nonchirped pulse of 50 fs pulsewidth.

### 3.1.2 Spatial and Temporal Characteristic Lengths

The spatial effects and the temporal effects are each characterized by three characteristic lengths. The physical meaning of each of these characteristic lengths has been mentioned in section 2.0. In this section, we show their numerical values and discuss their physical implications.

We see from Eqs. (9)-(11) that the spatial characteristic lengths can be normalized with respect to the pump beam waist size. In Fig. 7 (a), (b), and (c), we show the values of  $l_{sb}/w_{30}^2$ ,  $l_{sc}/w_{30}^2$ , and  $l_{sw}/w_{30}$ , respectively, as a function of signal wavelength for the three different pump wavelengths considered. Similarly, the temporal characteristic lengths can be normalized with respect to the pump pulsewidth, as can be seen from Eqs. (19)-(21). The values of  $l_{tb}/\Delta t_{30}^2$ ,  $l_{tc}/\Delta t_{30}^2$ ,

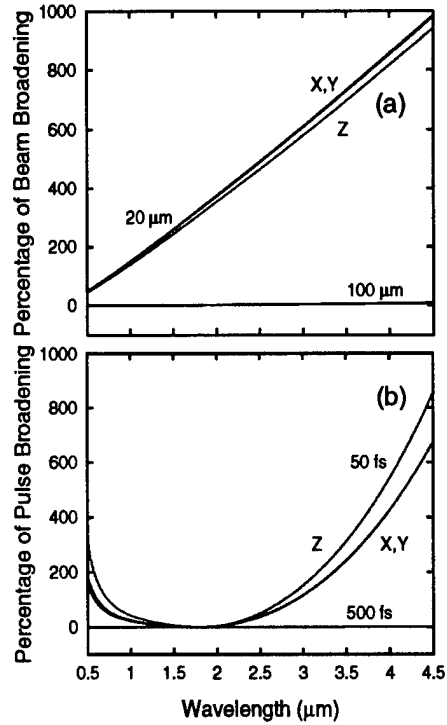


Figure 6: Percentage of (a) spatial beam broadening for focused beams of 20  $\mu\text{m}$  and 100  $\mu\text{m}$  initial beam waists and (b) temporal pulse broadening for nonchirped pulses of 50 fs and 500 fs initial pulse widths as a function of wavelength after traveling 5 mm through a KTP crystal with field polarization along one of the principal axes.

and  $l_{tw}/\Delta t_{30}$  are shown in Fig. 8 (a), (b), and (c), respectively, as a function of signal wavelength for the three different pump wavelengths. In Fig. 8 (b), the data for pump wavelength at 527 nm is not shown since in this case  $l_{tc}/\Delta t_{30}^2$  has either a negative value smaller than  $-21 \text{ m/ps}^2$  in some parts of the spectrum or, in other parts of the spectrum, a positive value larger than  $48 \text{ m/ps}^2$ . Therefore,  $l_{tc}$  for the 527 nm pump wavelength can be considered infinity for any practical purpose. In each of these plots, the solid curves show the data for  $o \rightarrow o + e$  phase matching with the signal being the  $o$ -wave while the dashed curves show those for  $o \rightarrow e + o$  phase matching with the signal being the  $e$ -wave. Note that each pair of corresponding  $o \rightarrow o + e$  and  $o \rightarrow e + o$  curves crosses at the degeneracy point, as expected.

For a given crystal length, the characteristic lengths determine the effective interaction length through Eq. (37), which in turn determines the parametric efficiency coefficient,  $b$ , through Eq. (33). To see the significance of each characteristic length, we examine the contributions of the spatial and the temporal effects to the effective length  $l_{\text{eff}}$  in Eq. (37). For the convenience of discussion, we recast Eq. (37) in the following form

$$l_{\text{eff}} = \int_0^{l_c} \sigma(z) dz = \int_0^{l_c} \sigma_s(z) \sigma_t(z) dz \quad (54)$$

where the integrand  $\sigma(z) = \sigma_s(z) \sigma_t(z)$  contains the contribution of the spatial effects:

$$\sigma_s(z) = \left[ 1 + \frac{(z - f_s)^2}{l_{sb}^2} \right]^{-1/2} \exp \left[ -\frac{(z - f_s)^2}{l_{sw}^2} \frac{1 + (z - f_s)^2/l_{sb}^2}{1 + (z - f_s)^2/l_{sb}^2} \right] \quad (55)$$

and the contribution of the temporal effects:

$$\sigma_t(z) = \left( 1 + \frac{z^2}{l_{tb}^2} \right)^{-1/4} \exp \left[ -\frac{(z - f_t)^2}{l_{tw}^2} \frac{1 + z^2/l_{tb}^2}{1 + z^2/l_{tb}^2} \right] \quad (56)$$

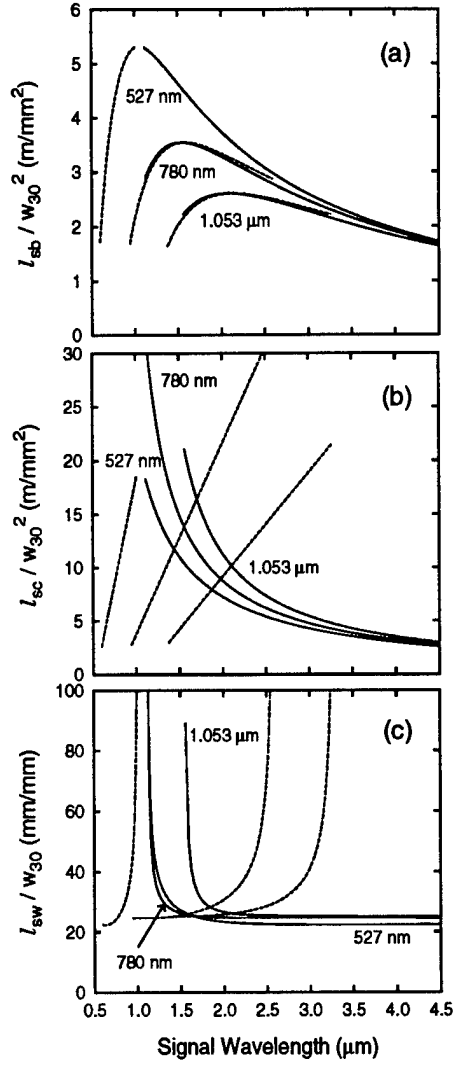


Figure 7: Spatial characteristic lengths normalized to pump beam waist as a function of signal wavelength for three different pump wavelengths at 1.053 μm, 780 nm, 527 nm using collinear phase matching geometry. The solid curves are for  $o \rightarrow o+e$  phase matching and the dashed curves are for  $o \rightarrow e+o$ .

From the functional form of  $\sigma_s(z)$  and  $\sigma_t(z)$ , it can be seen that the significance of each characteristic length increases as its value decreases. However, the significance of each characteristic length differs from one another. The function  $\sigma_s(z)$  depends most strongly on  $l_{sw}$  while  $\sigma_t(z)$  depends most strongly on  $l_{tw}$ . The spatial characteristic length  $l_{sb}$  shows its effect only when its absolute value is comparable to or smaller than that of  $l_{sw}$ . Similarly, the effect of the temporal characteristic length  $l_{tb}$  is observable only when the value of  $|l_{tb}|$  is comparable to or smaller than that of  $l_{tw}$ . The significance of  $l_{sc}$  and  $l_{tc}$  is subtler and less direct. It is determined by the relationship between their values and those of  $l_{sb}$  and  $l_{tb}$ , respectively. This can be seen from Eqs. (55) and (56) and will be further discussed later. Since  $l_{sb}$  and  $l_{sc}$  scale with  $w_{30}^2$  but  $l_{sw}$  is linearly proportional to  $w_{30}$ , the relative significance of  $l_{sb}$  and  $l_{sc}$  increases as the beam waist size decreases with tight focus. This can be seen from the fact that  $l_{sb} > 17$  mm,  $l_{sc} > 30$  mm, and  $l_{sw} > 2$  mm for  $w_{30} = 100$   $\mu$ m, but  $l_{sb} > 0.68$  mm,  $l_{sc} > 1.2$  mm and  $l_{sw} > 0.4$  mm for  $w_{30} = 20$   $\mu$ m, from reading the curves in Fig. 7. Similarly, the relative importance of  $l_{tb}$  and  $l_{tc}$  increases as the pulsewidth decreases. From reading the curves in Fig. 8, we find that  $|l_{tb}| > 100$  mm,  $|l_{tc}| > 130$  mm, and  $l_{tw} > 1.3$  mm for  $\Delta t_{30} = 500$  fs, but  $|l_{tb}| > 1$  mm,  $|l_{tc}| > 1.3$  mm, and  $l_{tw} > 0.13$  mm for  $\Delta t_{30} = 50$  fs. For pump wavelength at 780 nm, we can even find the situation that  $|l_{tb}| < l_{tw}$  in some parts of the spectrum when  $\Delta t_{30} = 50$  fs. However, only when the beam focus becomes very tight or the pulse becomes very short do the broadening effects set in to complicate the matter. Even then, the walk-off effects still remain important.

Therefore, the relative importance between the spatial and temporal effects

is mainly determined by the relationship between the values of the spatial and temporal walk-off lengths. The spatial effects dominate if  $l_{sw} < l_{tw}$  while the temporal effects dominate if  $l_{tw} < l_{sw}$ . If  $l_{sw}$  and  $l_{tw}$  have comparable values, the spatial and temporal effects are compounded. Because  $l_{sw}$  and  $l_{tw}$  depend linearly on  $w_{30}$  and  $\Delta t_{30}$ , respectively, the relationship between them can be translated into the relationship between  $w_{30}$  and  $\Delta t_{30}$ .

From the data in Figs. 7 (c) and 8 (c), one can deduce the value of  $\Delta t_{30}/w_{30}$  for the condition  $l_{sw} = l_{tw}$  when the spatial and temporal effects are equally important. This value is plotted in Fig. 9 as a function of signal wavelength for the three different pump wavelengths under consideration. This figure can be used directly to determine whether the spatial or the temporal effects dominate in a given experimental situation. If the value of  $\Delta t_{30}/w_{30}$  lies above a particular curve in Fig. 9, then  $l_{sw} < l_{tw}$  and the spatial effects dominate for the combination of experimental parameters corresponding to that curve. If it lies below the curve, then  $l_{tw} < l_{sw}$  and the temporal effects dominate. For example, for pump wavelength at  $1.053 \mu\text{m}$ , if  $\Delta t_{30} = 500 \text{ fs}$  and  $w_{30} = 100 \mu\text{m}$ , the temporal effects dominate for signal wavelength in the short range of  $\lambda_1 < 1.85 \mu\text{m}$  in the case of  $o \rightarrow o + e$  phase matching, but the spatial effects dominate for  $\lambda_1 < 2.45 \mu\text{m}$  in the case of  $o \rightarrow e + o$ . In contrast, over the entire spectral range of interest for  $w_{30} = 100 \mu\text{m}$ , the temporal effects dominate if  $\Delta t_{30} = 50 \text{ fs}$ , but the spatial effects dominate if  $\Delta t_{30} = 5 \text{ ps}$ .

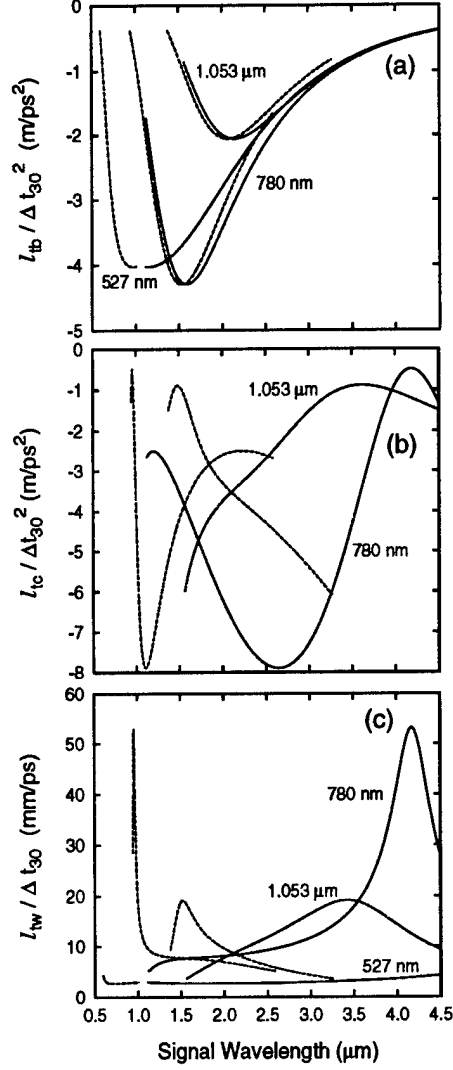


Figure 8: Temporal characteristic lengths normalized to pump pulsewidth waist as a function of signal wavelength for three different pump wavelengths at 1.053  $\mu\text{m}$ , 780 nm, 527 nm. The data of  $l_{tc}/\Delta t_{30}^2$  for 527 nm pump wavelength have very large absolute values outside of the scale for (b) and are not shown. The solid curves are for  $o \rightarrow o + e$  phase matching and the dashed curves are for  $o \rightarrow e + o$ .



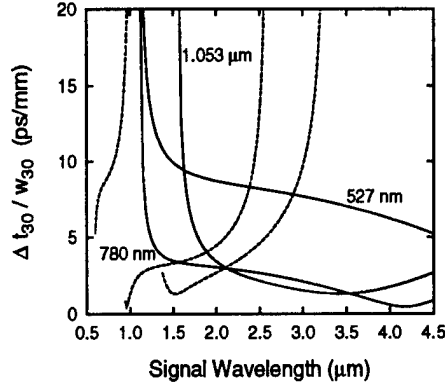


Figure 9: Ratio of pump pulsewidth to pump beam waist when spatial and temporal walk-off lengths are equal as a function of signal wavelength for three different pump wavelengths at 1.053  $\mu\text{m}$ , 780 nm, 527 nm using collinear phase matching geometry. The solid curves are for  $o \rightarrow o + e$  phase matching and the dashed curves are for  $o \rightarrow e + o$ .

### 3.1.3 Spatial and Temporal Overlap

It has been discussed in Ref. [5] that maximum parametric gain is obtained when the three interacting beams are focused in a manner such that their beam waists overlap at the same location and that this common focal point is located at the center of the nonlinear crystal. Therefore, in Eq. (2.5) only one common parameter  $f_s$  is used for all three beams. It is also clear that for maximum parametric gain, the three interacting pulses should be synchronized. This has led us to use again only one common parameter  $f_t$  in Eq. (2.13) for all three pulses. The question here is the relation between  $f_t$  and  $f_s$  for the most efficient parametric interaction among the ultrashort pulses.

This question can be answered by examining the relationship between  $\sigma_s(z)$  and  $\sigma_t(z)$ , defined in Eqs. (55) and (56), respectively. Note that  $\sigma_s(z)$  is independent of the temporal characteristics of the pulses and its shape and peak location are completely determined by the parameters  $w_{30}$  and  $f_s$ . In contrast,  $\sigma_t(z)$  is

independent of the spatial characteristics of the beams and its shape and peak location are completely determined by the parameters  $\Delta t_{30}$  and  $f_t$ .

Maximum parametric efficiency is obtained when  $l_{\text{eff}}$  is maximized. This occurs when the peaks of  $\sigma_s(z)$  and  $\sigma_t(z)$  coincide at the center of the crystal so that the area under  $\sigma(z)$  is maximized. It can be shown that the peak of  $\sigma_s(z)$  appears at  $z = f_s$ , which is the location of the common focal point of the three beams. However, for all cases of interest here, the peak of  $\sigma_t(z)$  appears at approximately  $z = f_t(1 + l_{tw}^2/4l_{tb}^2)^{-1}$ , which is ahead of the location  $z = f_t$  where the temporal peaks of the three pulses overlap. This is caused by the effect of pulse broadening in the crystal. Therefore, we should choose

$$f_s = l_c/2 \quad \text{and} \quad f_t \approx f_s \left(1 + \frac{l_{tw}^2}{4l_{tb}^2}\right) = \frac{l_c}{2} \left(1 + \frac{l_{tw}^2}{4l_{tb}^2}\right) \quad (57)$$

for maximum parametric efficiency. These optimal values of  $f_s$  and  $f_t$  are used for all the following calculations except otherwise noted.

The concept discussed here is demonstrated in Fig. 10 with an example of  $\lambda_3 = 1.053 \mu\text{m}$  and  $\lambda_1 = 3 \mu\text{m}$  in the case of  $o \rightarrow o + e$  phase matching for  $l_c = 5 \text{ mm}$  and different values of  $\Delta t_{30}$  and  $w_{30}$ . Shown in Fig. 10(a) is the situation when the peaks of  $\sigma_s(z)$  and  $\sigma_t(z)$  coincide at the center of the crystal. For a given combination of  $\Delta t_{30}$  and  $w_{30}$ , the temporal effects dominate and set the limit for the parametric efficiency if  $\sigma_t(z)$  has a narrower distribution than  $\sigma_s(z)$ . The same can be said for the spatial effects if  $\sigma_s(z)$  is narrower than  $\sigma_t(z)$ . For the case of  $\Delta t_{30} = 500 \text{ fs}$  shown in this particular example, the spatial effects dominate for both  $w_{30} = 100$  and  $20 \mu\text{m}$ . For  $\Delta t_{30} = 50 \text{ fs}$ , the temporal effects dominate when  $w_{30} = 100 \mu\text{m}$  but the spatial effects dominate when  $w_{30} = 20 \mu\text{m}$ . This can be verified from reading the corresponding  $o \rightarrow o + e$  curve for  $1.053 \mu\text{m}$  pump

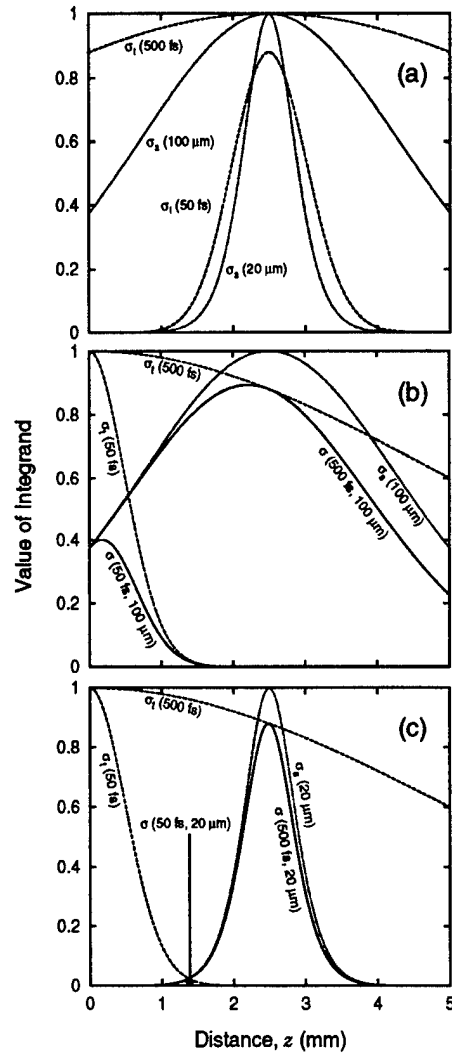


Figure 10: Distributions of the spatial contribution,  $\sigma_s$  (dotted curves), the temporal contribution,  $\sigma_t$  (dashed curves), and the total integrand,  $\sigma$  (solid curves), of the integral for the effective interaction lengths as a function of distance in a 5-mm KTP crystal for pump at  $1.053 \mu\text{m}$  and signal at  $3 \mu\text{m}$  wavelength with  $o \rightarrow o + e$  phase matching. Different combinations of pump beam waists of  $20 \mu\text{m}$  and  $100 \mu\text{m}$  with pump pulsewidths of  $50 \text{ fs}$  and  $500 \text{ fs}$  are shown. In (a), both beam overlap and pulse synchronization coincide at the center of the crystal. In (b) and (c), beam overlap occurs at the center but pulses are synchronized at the surface of the crystal.

wavelength in Fig. 9. Also seen in Fig. 10(a) is the fact that the peak of  $\sigma_t(z)$  for  $\Delta t_{30} = 50$  fs is reduced to a value somewhat smaller than 0.9. This is due to the effect of temporal pulse broadening. In this case,  $l_{tb} = -3$  mm while  $l_{tw} = 0.75$  mm. Even though the value of  $|l_{tb}|$  is still larger than that of  $l_{tw}$ , this effect is already observable after the pulses travel a distance of 2.5 mm to the center of the crystal.

Figures 10(b) and (c) demonstrate what happens when the beams are focused at a common focal point located at the center of the crystal but the pulses are temporally synchronized at the location of the input surface of the crystal. In these examples,  $f_s = l_c/2 = 2.5$  mm and  $f_t = 0$ . As can be seen, the area under  $\sigma(z)$  is reduced because the peaks of  $\sigma_s(z)$  and  $\sigma_t(z)$  are no longer located at the same location. This results in a reduced value for  $l_{\text{eff}}$  and a correspondingly reduced parametric efficiency. This reduction becomes more severe as the pulsewidth becomes shorter, as can be seen from comparing the  $\sigma(z)$  curve for the 50 fs pulse to that for the 500 fs pulse in Fig. 10(b). It also becomes more severe as the beam waist size becomes smaller, as can be seen from comparing Fig. 10(c) to Fig. 10(b) for the difference between  $w_{30} = 20$   $\mu\text{m}$  and  $w_{30} = 100$   $\mu\text{m}$ . Note that the peak of  $\sigma_t(z)$  for  $\Delta t_{30} = 50$  fs shown in Figs. 10(b) and (c) is not reduced because the pulses are not broadened when they overlap at the input surface of the crystal.

### 3.1.4 Effective Interaction Length and Optimal Crystal Length

The effective interaction length gives a measure of the useful length of a nonlinear crystal in a parametric process involving ultrashort pulses. As can be seen from Eq. (2.37), it is always less than the physical length,  $l_c$ , of the crystal and approaches  $l_c$  only when the crystal is shorter than all spatial and temporal characteristic

lengths. When  $l_c$  is sufficiently large, the effective interaction length is completely determined by the six spatial and temporal characteristic lengths.

We first consider the situation when  $|l_{sb}|, |l_{tb}| \gg l_{sw}$  and  $|l_{tb}|, |l_{tc}| \gg l_{tw}$  so that both the spatial beam broadening and temporal pulse broadening are negligible. In this case, the effective interaction length can be approximated by

$$\begin{aligned} l_{\text{eff}} &\approx \int_0^{l_c} \exp \left[ -\frac{(z - f_s)^2}{l_{sw}^2} \right] \exp \left[ -\frac{(z - f_t)^2}{l_{tw}^2} \right] dz \\ &\approx \int_0^{l_c} \exp \left[ -\frac{(z - l_c/2)^2}{l_w^2} \right] dz \\ &= \sqrt{\pi} l_w \text{erf} \left( \frac{l_c}{2l_w} \right), \end{aligned} \quad (58)$$

where the optimal values of  $f_t \approx f_s = l_c/2$  as given by Eq. (57) are used and

$$l_w = (l_{sw}^{-2} + l_{tw}^{-2})^{-1/2} \quad (59)$$

is the net walk-off length with the compounded spatial and temporal walk-off effects. We see from Eq. (58) that when the broadening effects are negligible,  $l_{\text{eff}}$  increases with increasing crystal length and has a maximum value of  $\sqrt{\pi} l_w$ . We also know from the behavior of the error function (erf) that this increase becomes minimal as  $l_c$  is increased beyond a few times  $l_w$ . Therefore, there exists an optimal length,  $l_{\text{opt}}$ , beyond which very little benefit is gained by further increasing the crystal length. A good choice is  $l_{\text{opt}} = 3l_w$ , which yields an  $l_{\text{eff}}$  at 96.6% of its maximum value of  $\sqrt{\pi} l_w$  and a parametric efficiency coefficient,  $b$ , at 93.3% of its maximum value. To summarize, with no spatial and temporal broadening, a single compounded walk-off length,  $l_w$ , determines the maximum value for  $l_{\text{eff}}$  and the optimal crystal length:

$$l_{\text{eff}} = 0.966\sqrt{\pi} l_w \approx 1.7l_w = 0.571l_c \quad \text{for} \quad l_c = l_{\text{opt}} = 3l_w. \quad (60)$$

In our numerical examples with KTP, this result applies to the cases of  $\Delta t_{30} = 5$  ps and 500 fs when  $w_{30} = 100$   $\mu\text{m}$ .

We next consider the more complicated situation when spatial and/or temporal broadening effects are important. In this case, the values of  $|l_{sb}|$  and  $|l_{tb}|$  are comparable to or less than those of  $l_{sw}$  and  $l_{tw}$ , respectively. However, the situation further depends on the values of  $l_{sc}$  and  $l_{tc}$ .

The effect of spatial beam broadening is simple because experimentally one is always able to overlap the three interacting beams at their beam waists. This allows us to consider only the most efficient case of locating all three beam waists at  $f_s = l_c/2$ , resulting in a  $\sigma_s(z)$  of the form given in Eq. (55). It can be seen from this form that the peak value of  $\sigma_s(z)$  at  $z = f_s$  is always unity, irrespective of the values of  $l_{sb}$  and  $l_{sc}$ . Therefore, spatial beam broadening reduces the magnitude of  $\sigma_s(z)$  only at locations away from  $z = f_s$ . This can lead to a reduction of the value of the  $l_{\text{eff}}$  when  $l_{sw} \leq l_{tw}$  and when significant reduction of the magnitude of  $\sigma_s(z)$  occurs within the spatial beam walk-off distance. However, this is effective only when  $l_{sc} \approx l_{sb}$  and both have absolute values comparable to or less than  $l_{sw}$ . In case  $|l_{sc}| \gg |l_{sb}|$ , the reduction in the magnitude of  $\sigma_s(z)$  away from  $z = f_s$  is almost exactly compensated by the increase in the width of the distribution of  $\sigma_s(z)$ , resulting in a negligible effect on the value of  $l_{\text{eff}}$ .

The effect of temporal pulse broadening on the value of  $l_{\text{eff}}$  is rather complicated. This is due to the fact that we have assumed that the pulses have their minimum pulsewidths at the input surface of the crystal but are synchronized to temporally overlap at  $z = f_t$  for the peak of  $\sigma_t(z)$  to coincide with that of  $\sigma_s(z)$  for maximum efficiency. This assumption is based on the realistic consideration that

it is experimentally difficult, if not impossible, to tune the temporal widths and the frequency chirping of the pulses to compensate for the effect of group-velocity dispersion in order for each pulse to have its minimum pulsewidth at the center of the crystal where the pulses overlap both spatially and temporally. As a result, the form of  $\sigma_t(z)$  is not symmetric with respect to  $z = f_t$ . This is different from the case of  $\sigma_s(z)$ , as can be seen from Eqs. (55) and (56). This difference is not important when the broadening effects are negligible, but becomes significant when pulse broadening is substantial. Temporal pulse broadening reduces the magnitude of  $\sigma_t(z)$ , including its peak value. In addition, it also broadens the distribution of  $\sigma_t(z)$ . This can be seen from Eq. (56) that at the peak location,  $z = f_t$ , the distribution of  $\sigma_t(z)$  can be approximately characterized by an effective temporal walk-off distance

$$l'_{tw} = l_{tw} \left( \frac{1 + f_t^2/l_{tb}^2}{1 + f_t^2/l_{tb}l_{tc}} \right)^{1/2}, \quad (61)$$

where  $f_t$  is that given in Eq. (57). This is physical and reflects the fact that the pulses have broadened from their initial widths when they finally overlap temporally at  $z = f_t$ . The broadening in the distribution of  $\sigma_t(z)$  is particularly significant when  $|l_{tc}| \gg |l_{tb}|$ . Sometimes, it can overcompensate for the peak reduction as  $f_t$  increases. This can result in an unusual, but physical, phenomenon of increasing  $l_{\text{eff}}$  due to pulse broadening as the crystal length increases. This increase eventually stops when the increase in  $l'_{tw}$  with increasing  $l_c$  saturates or when the spatial walk-off effects starts to set the limit, whichever happens first.

The effect of temporal pulse broadening on  $\sigma(z)$ , thus that on  $l_{\text{eff}}$ , under different conditions discussed above is illustrated in Fig. 11. Shown in this figure are the distributions of  $\sigma(z)$  for three different crystal lengths at three different pump

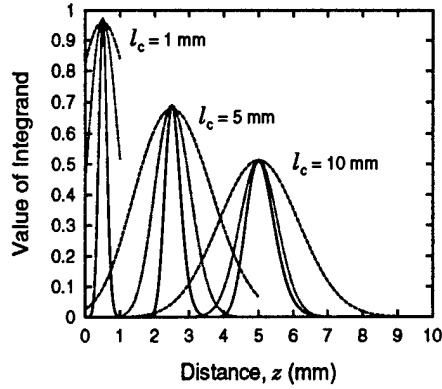


Figure 11: Distributions of the integrand,  $\sigma$ , of the integral for the effective interaction length as a function of distance for three different crystal lengths,  $l_c = 1$ , 5, and 10 mm, and three different pump wavelengths at  $1.053 \mu\text{m}$  (dotted curves), 780 nm (dashed curves), and 527 nm (solid curves), but the same signal wavelength at  $4 \mu\text{m}$  with  $o \rightarrow o + e$  phase matching.

wavelengths of  $1.053 \mu\text{m}$ , 780 nm, and 527 nm, but at the same signal wavelength of  $4 \mu\text{m}$ . The pump beam waist is  $w_{30} = 100 \mu\text{m}$  and the pump pulsewidth is  $\Delta t_{30} = 50$  fs. Therefore,  $\sigma(z) \approx \sigma_t(z)$  and the illustration clearly demonstrates the effect of temporal broadening on the value of  $l_{\text{eff}}$ . Under the given conditions, we have  $l_{tw} = 0.6, 1.76$ , and  $0.15$  mm,  $l_{tb} = -1.37, -1.38$ , and  $-1.35$  mm, and  $l_{tc} = -2.6, -2.2$ , and  $466$  mm, for  $\lambda_3 = 1.053 \mu\text{m}$ , 780 nm, and 527 nm, respectively. Because the value of  $l_{tb}$  is about the same for all three pump wavelengths, the reduction in the peak value of  $\sigma(z)$  due to pulse broadening is about the same for all of them at a particular crystal length. However, for  $\lambda_3 = 1.053 \mu\text{m}$  and 780 nm,  $l_{tc}$  and  $l_{tb}$  are of the same order of magnitude. Therefore, there is little broadening in the distribution of  $\sigma(z)$  and a decrease in  $l_{\text{eff}}$  measured by the area under  $\sigma(z)$  can be seen as  $l_c$  increases from 5 to 10 mm for these two pump wavelengths. In contrast, since  $|l_{tc}| \gg |l_{tb}|$  for  $\lambda_3 = 527$  nm, the distribution of  $\sigma(z)$  broadens faster than the decrease in its peak, resulting in an increased area under



Table 1: Variation of temporal characteristic lengths with pump wavelength for 50 fs pump pulsewidth and 4  $\mu\text{m}$  signal wavelength.

$\lambda_3$	$l_{tb}$	$l_{tc}$	$l_{tw}$	$l'_{tw}(l_c = 1 \text{ mm})$	$l'_{tw}(l_c = 5 \text{ mm})$	$l'_{tw}(l_c = 10 \text{ mm})$
1.053 $\mu\text{m}$	-1.37 mm	-2.6 mm	0.6 mm	0.62 mm	0.75 mm	0.80 mm
780 nm	-1.38 mm	-2.2 mm	1.76 mm	1.8 mm	2.08 mm	2.18 mm
527 nm	-1.35 mm	466 mm	0.15 mm	0.163 mm	0.33 mm	0.61 mm

$\sigma(z)$  and a corresponding increase in  $l_{\text{eff}}$  as  $l_c$  increases from 1 to 5 to 10 mm. In this particular example, Eq. (61) yields  $l'_{tw} = 0.163, 0.33$ , and  $0.61$  mm for  $l_c = 1, 5$ , and  $10$  mm, respectively. Using the dispersion data of KTP and starting with  $\Delta t_{30} = \Delta t_{10} = \Delta t_{20} = 50$  fs, the broadened pulsewidths of the pump, signal, and idler at the location  $z = f_t \approx l_c/2$  can be calculated for each value of  $l_c$ . These data can be used to calculate the real temporal walk-off distance of these broadened pulses at the location of their temporal overlap using Eq. (21). The results are  $l'_{tw} = 0.164, 0.36$ , and  $0.65$  mm for  $l_c = 1, 5$ , and  $10$  mm, respectively, in close agreement with the values obtained above using Eq. (61) and summarized in Table 3.1. The pulses have broadened substantially indeed. For  $l_c = 5$  mm,  $\Delta t_1 = 138$  fs,  $\Delta t_2 = 70$  fs, and  $\Delta t_3 = 77$  fs at  $z = l_c/2 = 2.5$  mm. For  $l_c = 10$  mm,  $\Delta t_1 = 262$  fs,  $\Delta t_2 = 109$  fs, and  $\Delta t_3 = 128$  fs at  $z = l_c/2 = 5$  mm.

We see from the above demonstration that in the presence of temporal pulse broadening the maximum value of  $l_{\text{eff}}$  can appear with a very large crystal length. In this situation, it is clear that the optimal crystal length is not simply the one that gives the highest value for  $l_{\text{eff}}$  unless the substantial broadening in the output pulsewidths associated with the use of a long crystal is of no concern, which then

defeats the purpose of using the ultrashort pump pulses in the first place. Therefore, the optimal crystal length is dictated by the amount of pulse broadening allowed. This depends on each specific situation and is hard to generalize.

### 3.1.5 Parametric Efficiency Coefficient

The effective field gain  $G_{\text{eff}}$  defined in Eq. (32) is the parameter which ultimately determines the performance of a parametric device generating or amplifying ultrashort optical pulses. This parameter depends on the energy of the pump pulse and, when gain saturation sets in at a given pumping level, also the energy of the signal pulse. A good parameter which measures the efficiency of a parametric device without referring to the specifics of the pump and signal energy levels is the parametric efficiency coefficient,  $b$ , given by Eq. (33). When the value of this coefficient is known for a particular experimental system, the value of  $G_{\text{eff}}$  at various pumping levels can be easily calculated using Eq. (32).

For a given crystal length and given pump pulsewidth and beam waist size, the value of  $l_{\text{eff}}$  is calculated using Eq. (37). It is then used to obtain the parametric efficiency coefficient using Eq. (33). The results are shown as a function of signal wavelength in Figs. 12, 13, and 14 for pump beam waist  $w_{30} = 100 \mu\text{m}$  and pump pulsewidths  $\Delta t_{30} = 5 \text{ ps}$ ,  $500 \text{ fs}$ , and  $50 \text{ fs}$ , respectively, and Figs. 15, 16, and 17 for  $w_{20} = 20 \mu\text{m}$  and the same three corresponding pump pulsewidths. The data for pump wavelengths at  $1.053 \mu\text{m}$ ,  $780 \text{ nm}$ , and  $527 \text{ nm}$  are shown in each figure for direct comparison. Shown in each plot are the data for different crystal lengths  $l_c = 1, 5, \text{ and } 10 \text{ mm}$ . A large value of  $b$  represents an efficient parametric device.

The general features of each curve in these figures reflect the characteristics of

the dominating characteristic lengths. This is most obvious for  $l_c = 10$  mm but becomes less significant for shorter crystal lengths. When  $l_c$  is large, the parametric efficiency coefficient is subject to the same limitations imposed by the spatial and temporal effects as those discussed above for the maximum value of  $l_{\text{eff}}$  because  $l_{\text{eff}}$  approaches its maximum value in this case. However, when  $l_c$  is relatively small,  $l_{\text{eff}}$  may be limited more by the physical length of the crystal than by the limiting characteristic lengths. The latter situation appears most when both  $w_{30}$  and  $\Delta t_{30}$  are large while  $l_c$  is small, as in the cases of  $l_c = 1$  mm for  $w_{30} = 100$   $\mu\text{m}$  and  $\Delta t_{30} = 5$  ps and 500 fs shown in Figs. 12 and 13.

If temporal pulse broadening is not important, an increase in crystal length towards the value of  $l_{\text{opt}}$  defined in Eq. (60) definitely improves the parametric efficiency. This improvement continues but gradually slows down when  $l_c$  approaches  $l_{\text{opt}}$ . Beyond this, the parametric efficiency saturates. This is true even when the effect of spatial beam broadening is present although in this case the optimal crystal length is somewhat longer than that given by Eq. (60), as is discussed earlier. This phenomenon can be seen from comparing the data for  $l_c = 5$  mm and those for  $l_c = 10$  mm in the cases of  $\Delta t_{30} = 5$  ps and 500 fs shown in Figs. 12 and 13, respectively, for  $w_{30} = 100$   $\mu\text{m}$  and in Figs. 15 and 16 for  $w_{30} = 20$   $\mu\text{m}$ . If the temporal broadening effect is important, as is the case with  $\Delta t_{30} = 50$  fs, increasing the crystal length can result in either an increase or decrease of efficiency depending on the initial crystal length and the relative values of the temporal characteristic lengths. This can be understood from the dependence of  $l_{\text{eff}}$  on  $l_c$  discussed earlier. Therefore, the characteristics seen in Fig. 14 and 17 can be understood in light of the phenomena illustrated in Fig. 11.

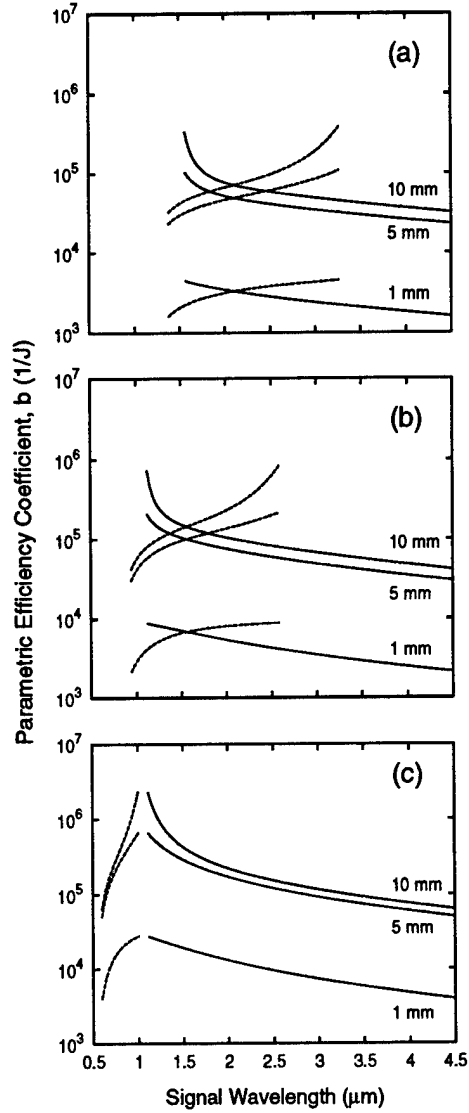


Figure 12: Parametric efficiency coefficient in KTP as a function of signal wavelength in the case of  $w_{30} = 100 \mu\text{m}$  and  $\Delta t_{30} = 5 \text{ ps}$  for three different pump wavelengths at (a)  $1.053 \mu\text{m}$ , (b)  $780 \text{ nm}$ , and (c)  $527 \text{ nm}$  using collinear phase matching geometry. The solid curves are for  $o \rightarrow o + e$  phase matching and the dashed curves are for  $o \rightarrow e + o$ .

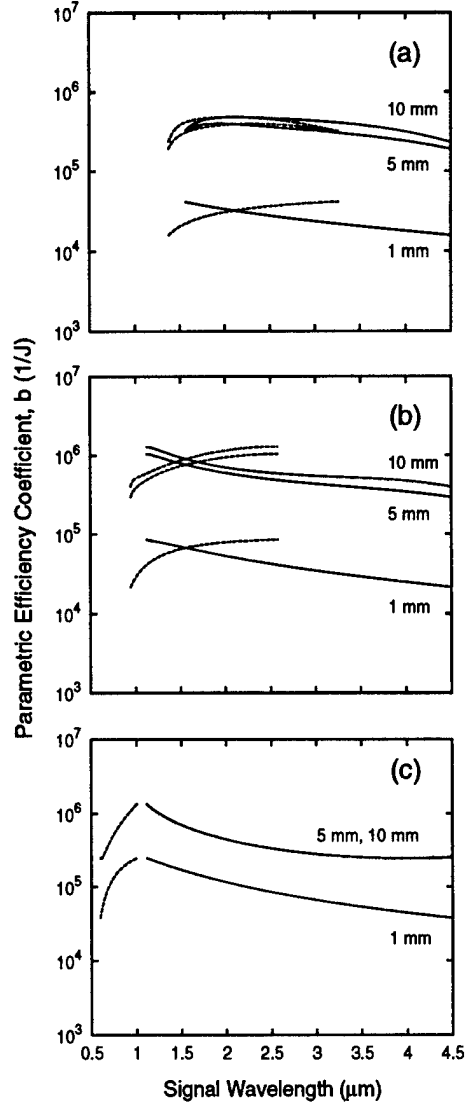


Figure 13: Parametric efficiency coefficient in KTP as a function of signal wavelength in the case of  $w_{30} = 100 \mu\text{m}$  and  $\Delta t_{30} = 500 \text{ fs}$  for three different pump wavelengths at (a)  $1.053 \mu\text{m}$ , (b)  $780 \text{ nm}$ , and (c)  $527 \text{ nm}$  using collinear phase matching geometry. The solid curves are for  $o \rightarrow o + e$  phase matching and the dashed curves are for  $o \rightarrow e + o$ .

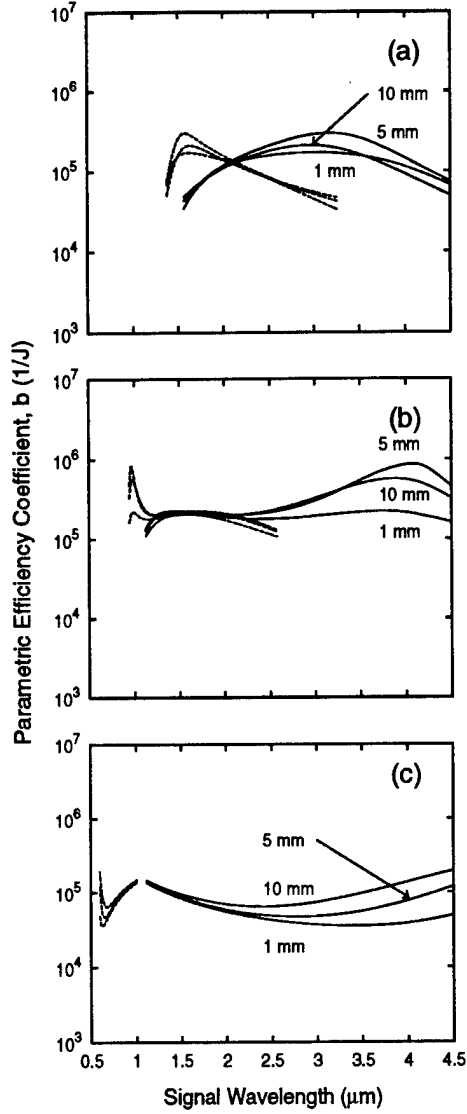


Figure 14: Parametric efficiency coefficient in KTP as a function of signal wavelength in the case of  $w_{30} = 100 \mu\text{m}$  and  $\Delta t_{30} = 50 \text{ fs}$  for three different pump wavelengths at (a)  $1.053 \mu\text{m}$ , (b)  $780 \text{ nm}$ , and (c)  $527 \text{ nm}$  using collinear phase matching geometry. The solid curves are for  $o \rightarrow o + e$  phase matching and the dashed curves are for  $o \rightarrow e + o$ .

There are general trends for the dependence of the parametric efficiency on the pump parameters, such as pump wavelength, pump pulsewidth, and pump beam waist. However, there are exceptions for the dependence on each parameter. These exceptions result from the competition of different spatial and temporal effects and can be explained by comparing the relative importance of the competing effects.

As a general trend, the parametric efficiency increases as the pump wavelength becomes shorter when other parameters are kept the same. This is mainly due to the fact that the net frequency dependence of  $a'$  defined in Eq. (34) is approximately  $a' \propto \omega_1 \omega_2 \propto 1/\lambda_1 \lambda_2$ . As the pump wavelength  $\lambda_3$  becomes shorter, the idler wavelength  $\lambda_2$  corresponding to a particular signal wavelength  $\lambda_1$  also becomes shorter. This effectively increases the value of  $a'$ , thus increasing that of the parametric efficiency coefficient if other factors remain unchanged. However, other factors do change adversely in certain cases. This is seen in the comparison between Figs. 13(b) and (c) for  $\Delta t_{30} = 500$  fs and in that between Figs. 14(b) and (c) for  $\Delta t_{30} = 50$  fs, where the value of the parametric efficiency coefficient drops as the pump wavelength decreases from 780 nm to 527 nm. The reason for this anomaly is that  $l_{tw}$  for  $\lambda_3 = 527$  nm is substantially smaller than that for  $\lambda_3 = 780$  nm, as can be seen from Fig. 8(c). Therefore, when the pulsewidth is reduced to a level at which the temporal walk-off effect becomes dominant, the reduction in the effective interaction length for  $\lambda_3 = 527$  nm more than offsets the gain in  $a'$  with respect to  $\lambda_3 = 780$  nm, resulting in a reduced efficiency.

In general, the parametric efficiency also increases as the pump pulsewidth or the pump beam waist is reduced. This is intuitively expected from Eq. (33). However,  $l_{eff}$  also depends on  $w_{30}$  and  $\Delta t_{30}$  through the dependence of the spatial

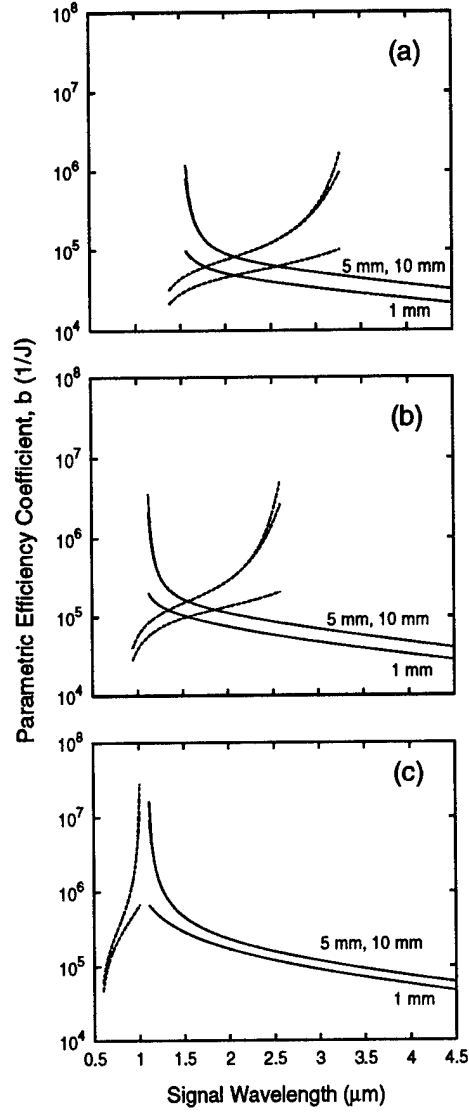


Figure 15: Parametric efficiency coefficient in KTP as a function of signal wavelength in the case of  $w_{30} = 20 \mu\text{m}$  and  $\Delta t_{30} = 5 \text{ ps}$  for three different pump wavelengths at (a)  $1.053 \mu\text{m}$ , (b)  $780 \text{ nm}$ , and (c)  $527 \text{ nm}$  using collinear phase matching geometry. The solid curves are for  $o \rightarrow o + e$  phase matching and the dashed curves are for  $o \rightarrow e + o$ .



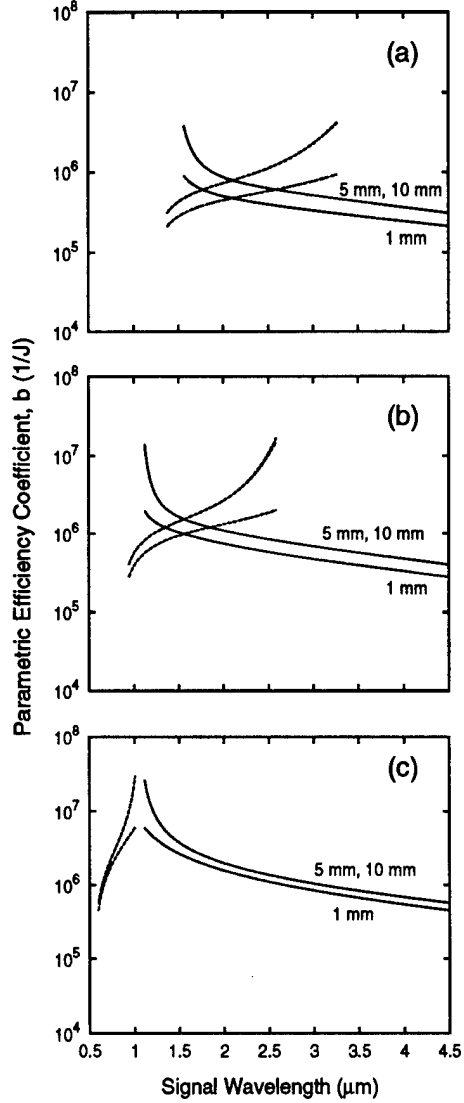


Figure 16: Parametric efficiency coefficient in KTP as a function of signal wavelength in the case of  $w_{30} = 20 \mu\text{m}$  and  $\Delta t_{30} = 500 \text{ fs}$  for three different pump wavelengths at (a)  $1.053 \mu\text{m}$ , (b)  $780 \text{ nm}$ , and (c)  $527 \text{ nm}$  using collinear phase matching geometry. The solid curves are for  $o \rightarrow o + e$  phase matching and the dashed curves are for  $o \rightarrow e + o$ .

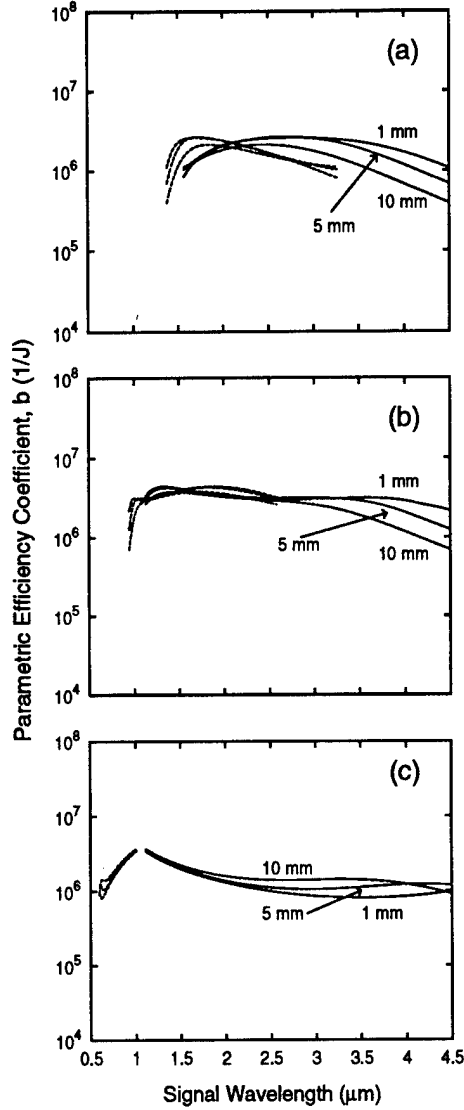


Figure 17: Parametric efficiency coefficient in KTP as a function of signal wavelength in the case of  $w_{30} = 20 \mu\text{m}$  and  $\Delta t_{30} = 50 \text{ fs}$  for three different pump wavelengths at (a)  $1.053 \mu\text{m}$ , (b)  $780 \text{ nm}$ , and (c)  $527 \text{ nm}$  using collinear phase matching geometry. The solid curves are for  $o \rightarrow o + e$  phase matching and the dashed curves are for  $o \rightarrow e + o$ .

and temporal characteristic lengths on these two parameters. Therefore, only when  $l_{\text{eff}}$  is not strongly limited by the characteristic lengths can one expect this general trend to be true. This clearly favors the situation of a short crystal because  $l_{\text{eff}}$  becomes more limited by the physical length  $l_c$  and less limited by the characteristic lengths. For the dependence of  $b$  on  $\Delta t_{30}$ , we can expect that deviation from the general trend of increasing  $b$  with decreasing  $\Delta t_{30}$  appears more often as the pulsewidth becomes shorter and the crystal length becomes longer. This can be seen by comparing Figs. 13 and 14. As for the dependence of  $b$  on  $w_{30}$ , we can expect that the general trend of increasing  $b$  with decreasing  $w_{30}$  holds more true and approaches the ideal quadratic dependence of  $b \propto 1/w_{30}^2$  for smaller  $\Delta t_{30}$  and smaller  $l_c$ . Deviation from this trend is expected to occur in the case of large  $\Delta t_{30}$  and large  $l_c$ , as can be seen from comparing the corresponding curves between Figs. 12 and 15 for  $l_c = 10$  mm and  $\Delta t_{30} = 5$  ps.

### 3.2 Noncollinear Phase Matching

Up to this point, all previous discussions on numerical simulations only considered the collinear phase matching geometry in KTP crystal. As we have mentioned previously, for certain experimental conditions, noncollinear phase matching will enhance the parametric efficiency. In this section, we will briefly discuss the method for maximizing the parametric coefficient,  $b$ , and compare the values of  $b$  of the collinear case with that of the noncollinear case. The change in the values of the characteristic lengths from the collinear case to the noncollinear case is also briefly discussed.

### 3.2.1 Maximization of Parametric Efficiency Coefficient for Noncollinear Phase Matching Cases

As we have discussed in section 2.5, to increase the parametric efficiency,  $l_{sw}$  needs to be maximized. In order for us to maximize  $l_{sw}$ , we first found a collinear phase matching angle, defined as  $\theta_c$ , for a given set of the signal, idler, and pump wavelengths that satisfy Eq. (1). As we have mentioned previously,  $\alpha_j = \gamma_j + \varphi_j$ . For collinear phase matching,  $\gamma_1 = \gamma_2 = \gamma_3 = 0^\circ$  while the values of  $\varphi_j$ 's depend on the polarization of the corresponding waves. Considering Type II,  $o \rightarrow e + o$  phase matching conditions,  $\varphi_2 = \varphi_3 = 0^\circ$  and  $\varphi_1$  is calculated by substituting  $\theta_c$  and  $\lambda_1$  into Eq. (51). Substituting corresponding values of  $\gamma_j$ 's and  $\varphi_j$ 's in the definition of  $\alpha_j$ 's yields that  $\alpha_2 = \alpha_3 = 0^\circ$  and  $\alpha_c = \alpha_1 = \varphi_1$ , as shown in Fig. 5.

For the noncollinear phase matching geometry, we scan  $\theta_1$  from  $\theta_c$  to  $\theta_c + |\alpha_c|$  in small increments. For a fixed set of the signal, idler, and the pump wavelengths with  $\gamma_3 = 0^\circ$ , the calculations show that  $n_e(\theta_1) < n_e(\theta_c)$  where  $\theta_1 < \theta_c$ . Therefore, we did not need to scan  $\theta_1$  from  $\theta_c - |\alpha_c|$  to  $\theta_c$  because there is no possible noncollinear phase matching solution for any values of  $\gamma_1$  and  $\gamma_2$ . Therefore, for a given value of  $\theta_1$ , we solved Eqs. (52) and (53) and determined the values of  $\gamma_1$  and  $\gamma_2$ . It is possible to have two sets of  $\gamma_1$  and  $\gamma_2$  that satisfy Eqs. (52) and (53) because of geometrical symmetry. In other words, for a given set of solutions,  $\gamma_1$  and  $\gamma_2$ , the respective signs of  $\gamma_1$  and  $\gamma_2$  can be reversed and Eqs. (52) and (53) are still satisfied. For Type II,  $o \rightarrow e + o$  phase matching geometry in KTP, the negative  $\gamma_1$  was not considered because of the reasons stated in section 2.5. With the known values of  $\theta_1$ ,  $\gamma_1$ ,  $\gamma_2$ , and  $\gamma_3$ ,  $\theta_3$  and  $\theta_2$  are calculated from  $\theta_3 = \theta_1 - \gamma_1$

and  $\theta_2 = \theta_3 + \gamma_2$ , respectively. From these values of  $\theta$ 's, the values of  $\varphi$ 's are determined. Since we only considered Type II,  $o \rightarrow e + o$  phase matching geometry in KTP, only  $\varphi_1$  was calculated using Eq. (51).  $\alpha_j$ 's are calculated by substituting corresponding values of  $\varphi$ 's and  $\gamma$ 's in  $\alpha_j = \varphi_j + \gamma_j$ . For each increment of  $\theta_1$ ,  $l_{sw}$  was calculated with the corresponding  $\alpha$ 's. Finally, we only chose the set of solutions that produces the maximum  $l_{sw}$ , and then we used it to calculate the characteristic lengths and the parametric efficiency coefficient.

To clarify the procedure, we chose two representative cases,  $\lambda_1 = 2 \mu\text{m}$  and  $3.25 \mu\text{m}$ , for the pump wavelength  $1.053 \mu\text{m}$  with  $o \rightarrow e + o$  phase matching geometry. As shown in Fig. 5, these two cases were chosen because they are at the opposite ends of the signal wavelength range, where the shorter signal wavelength results in a relatively substantial walk off-angle,  $\alpha_1 = 2.72^\circ$ , and the longer wavelength results in a relatively small walk-off angle,  $\alpha_1 = 0.62^\circ$ . To further discuss the method, the changes in  $\alpha$ 's,  $\gamma$ 's, and the corresponding values of  $l_{sw}$  are plotted for  $\lambda_1 = 2 \mu\text{m}$  in Fig. 18 and for  $\lambda_1 = 3.25 \mu\text{m}$  in Fig. 19, respectively. In general, the maximum value of  $l_{sw}$  occurs where  $\alpha_1$  and  $\alpha_2$  are equal to each other for this minimizes the value of the denominator in Eq. (11). This type of maximization in noncollinear phase matching will increase the value of  $l_{sw}$  roughly about 2 to 3 times that of  $l_{sw}$  for the collinear phase matching.

### 3.2.2 Characteristic Lengths for Noncollinear Phase Matching

As we examine the equations for the spatial characteristic lengths, Eqs. (9), (10), and (11), we notice that only  $l_{sc}$  and  $l_{sw}$  are affected by the phase-matching geometry. As shown in Fig. 20, the values of  $l_{sb}$  do not change but  $l_{sc}$  and  $l_{sw}$

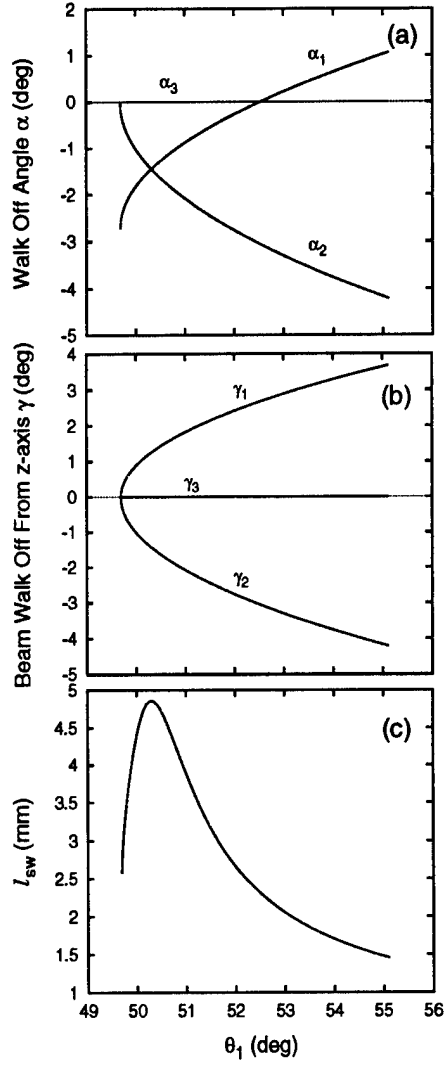


Figure 18: Changes in  $\alpha$ 's,  $\gamma$ 's, and the value of  $l_{sw}$  at  $\lambda_1 = 2.00 \mu\text{m}$  and  $\lambda_3 = 1.053 \mu\text{m}$  for  $o \rightarrow e + o$  phase matching as  $\theta_1$  varies from  $\theta_c$  to  $\theta_c + 2\alpha_c$ .

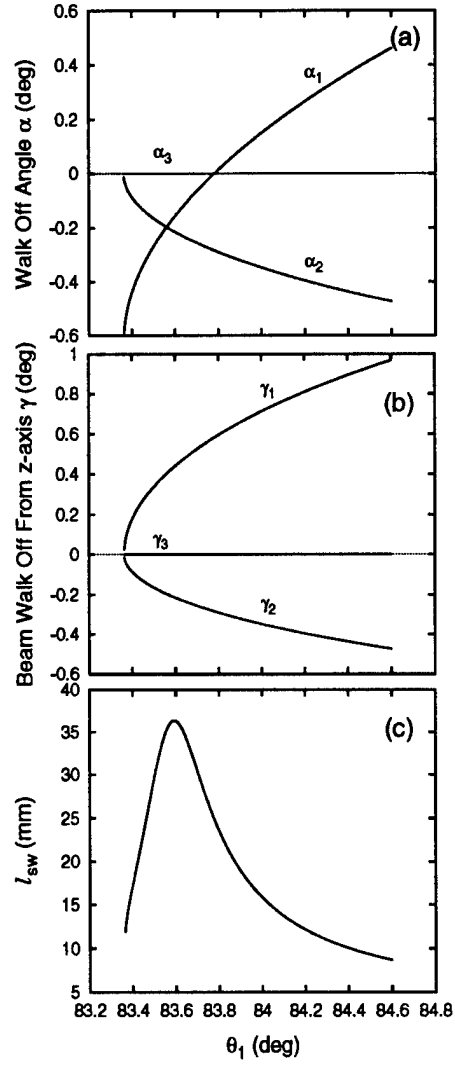


Figure 19: Changes in  $\alpha$ 's,  $\gamma$ 's, and the value of  $l_{sw}$  at  $\lambda_1 = 3.25 \mu\text{m}$  and  $\lambda_3 = 1.053 \mu\text{m}$  for  $o \rightarrow e + o$  phase matching as  $\theta_1$  varies from  $\theta_c$  to  $\theta_c + 2\alpha_c$ .

do. Compared to the values of  $l_{sw}$ 's for the collinear phase matching geometry in Fig. 7 (c), that of  $l_{sw}$ 's for the noncollinear in Fig. 20 (c) are generally 2 to 3 times greater. It is also interesting to see that the plot of  $l_{sc}$  normalized with respect to the pump beam waist is strikingly similar to that of  $l_{sb}$ . As we mentioned before,  $l_{sb}$  is a length parameter characterizing the effect of spatial beam broadening due to diffraction while  $l_{sc}$  is a characteristic length of the combined effect of beam broadening and beam walk-off. Since the beam walk-off had been compensated with the noncollinear phase matching geometry, the values of  $l_{sc}$  shown in Fig. 20 (b) naturally approach those of  $l_{sb}$  shown in Fig. 20 (a).

The effects of noncollinear phase matching on the characteristic lengths can be summarized in Fig. 21 which is a counterpart to Fig. 9. As expected, all curves for the noncollinear phase matching were shifted up compare to the ones in the collinear phase matching geometry. This in essence increases the spatial dominance roughly by a factor of two. The region above the curves in Fig. 21, once again, is the region of spatial dominance where the temporal effects do not limit the parametric efficiency. This implies that noncollinear phase matching is only useful for the region above the curves in Fig. 21. This implication is realized when comparing the parametric efficiency coefficients in the following section.

### 3.2.3 Parametric Efficiency Coefficient for Noncollinear Phase Matching

The effects of maximizing the parametric efficiency coefficient using the noncollinear phase matching geometry can be summarized in two sentences. One is that there was a substantial increase in the parametric efficiency coefficient, unless



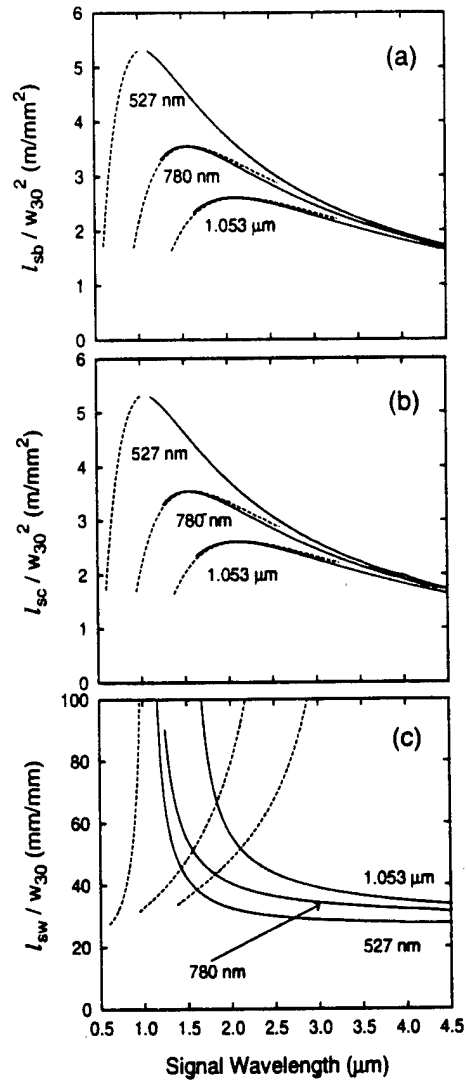


Figure 20: Spatial characteristic lengths normalized to pump beam waist as a function of signal wavelength for three different pump wavelengths at 1.053 μm, 780 nm, 527 nm using noncollinear phase matching geometry. The solid curves are for  $o \rightarrow o + e$  phase matching and the dashed curves are for  $o \rightarrow e + o$ .

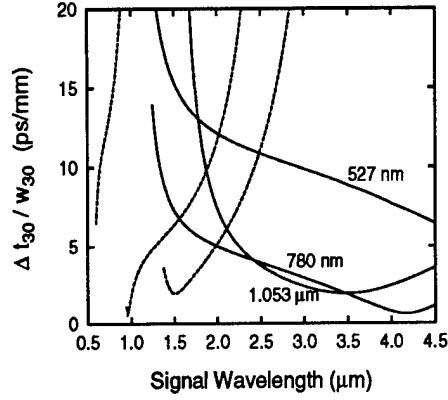


Figure 21: Ratio of pump pulsewidth to pump beam waist when spatial and temporal walk-off lengths are equal as a function of signal wavelength for three different pump wavelengths at 1.053  $\mu\text{m}$ , 780 nm, 527 nm using noncollinear phase matching geometry. The solid curves are for  $o \rightarrow o + e$  phase matching and the dashed curves are for  $o \rightarrow e + o$ .

limited by the crystal length, for conditions where the spatial effects are dominant. The other is that there is no substantial gain in implementing noncollinear phase matching for the systems in which the temporal effects are dominant.

Before we start discussing the effects of noncollinear phase-matching on the parametric efficiency, pertinent issues in the calculation of  $b$  should be addressed. In short, for Type II phase-matching conditions assumed in the previous section, the value of  $\theta$  to be used to calculate  $\chi_{\text{eff}}$  is  $\theta_e$ .  $\theta_e$  is defined as the angle between  $z$ -axis and the direction of the wave propagation for an extraordinary wave. In collinear phase-matching, the value of  $\theta$  substituted in calculating the value of  $\chi_{\text{eff}}$  was simply  $\theta_c$  because  $\theta_e = \theta_c$ . For noncollinear phase-matching, however,  $\theta_e = \theta_1$  for  $o \rightarrow e + o$  interaction and  $\theta_e = \theta_2$  for  $o \rightarrow o + e$  interaction. In summary, the change in the values of  $\chi_{\text{eff}}$  from the collinear case to the noncollinear case is very slight because the deviation of calculated  $\theta_1$ (or  $\theta_2$ ) from  $\theta_c$  is very small and is always less than  $\alpha_c$ .

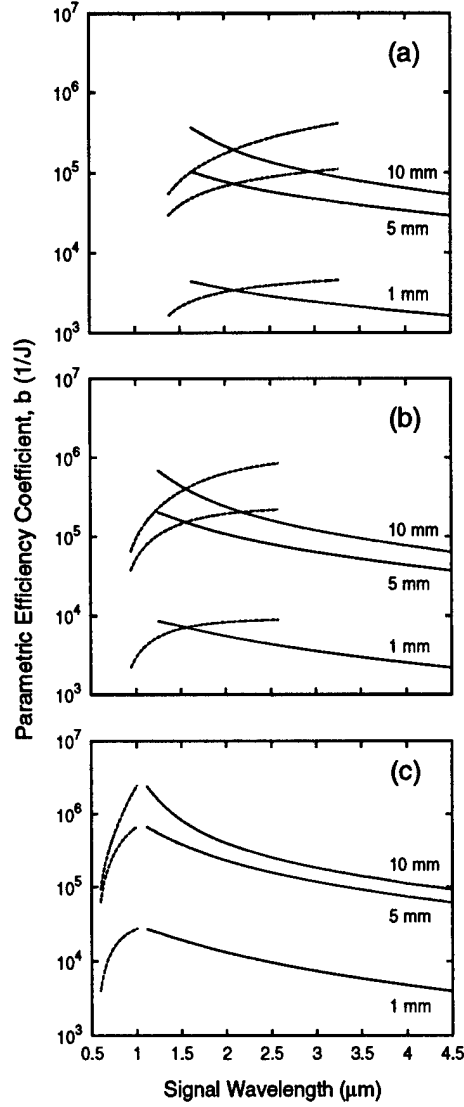


Figure 22: Parametric efficiency coefficient in KTP as a function of signal wavelength in the case of  $w_{30} = 100 \mu\text{m}$  and  $\Delta t_{30} = 5 \text{ ps}$  for three different pump wavelengths at (a)  $1.053 \mu\text{m}$ , (b)  $780 \text{ nm}$ , and (c)  $527 \text{ nm}$  using noncollinear phase matching geometry. The solid curves are for  $o \rightarrow o + e$  phase matching and the dashed curves are for  $o \rightarrow e + o$ .

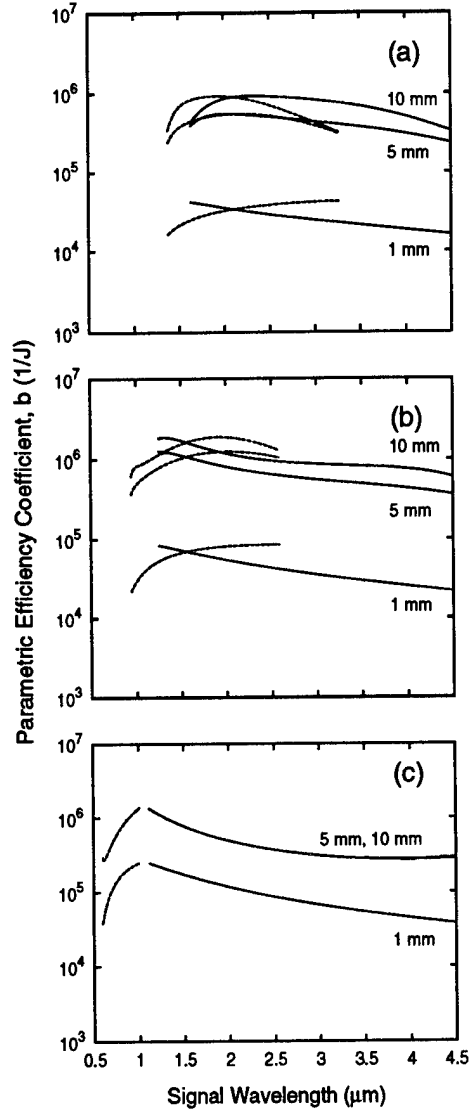


Figure 23: Parametric efficiency coefficient in KTP as a function of signal wavelength in the case of  $w_{30} = 100 \mu\text{m}$  and  $\Delta t_{30} = 500 \text{ fs}$  for three different pump wavelengths at (a)  $1.053 \mu\text{m}$ , (b)  $780 \text{ nm}$ , and (c)  $527 \text{ nm}$  using noncollinear phase matching geometry. The solid curves are for  $o \rightarrow o + e$  phase matching and the dashed curves are for  $o \rightarrow e + o$ .

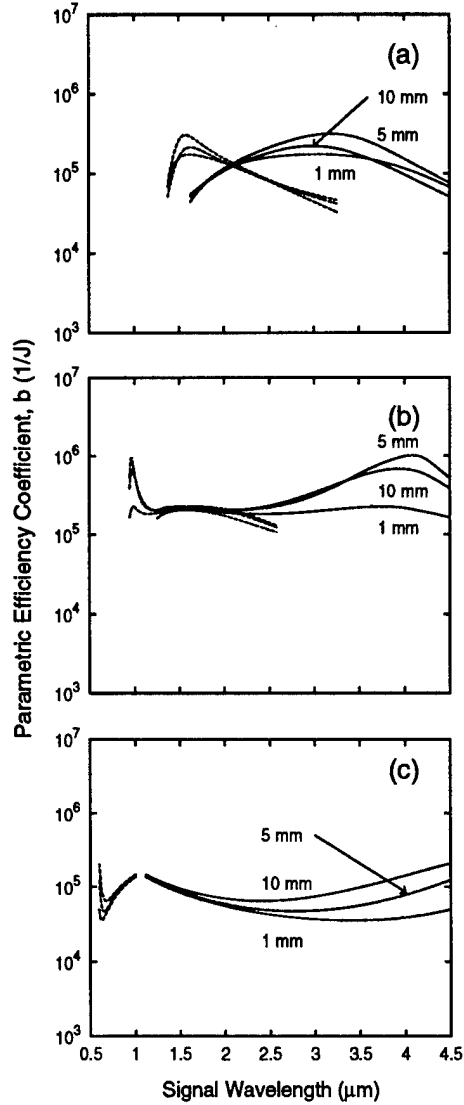


Figure 24: Parametric efficiency coefficient in KTP as a function of signal wavelength in the case of  $w_{30} = 100 \mu\text{m}$  and  $\Delta t_{30} = 50 \text{ fs}$  for three different pump wavelengths at (a)  $1.053 \mu\text{m}$ , (b)  $780 \text{ nm}$ , and (c)  $527 \text{ nm}$  using noncollinear phase matching geometry. The solid curves are for  $o \rightarrow o + e$  phase matching and the dashed curves are for  $o \rightarrow e + o$ .

As shown in Figs. 22, the parametric efficiency coefficient has increased 2 to 3 times that of the collinear case in Figs. 12 for the crystal lengths of 5 and 10 mm. Naturally, the parametric efficiency coefficient for the crystal length of 1 mm has not increased much because in this case the parametric interaction length is limited by the physical length of the crystal. The effects of the noncollinear phase-matching geometry on the parametric efficiency become less pronounced as we compare the cases of  $w_{30} = 100 \text{ } \mu\text{m}$  and  $\Delta t_{30} = 500 \text{ fs}$  in Fig. 23. The increase in the value of the parametric efficiency is virtually zero for  $l_c = 1 \text{ mm}$  and is much less for  $l_c = 5$  and  $10 \text{ mm}$  than the  $\Delta t_{30} = 5 \text{ ps}$  cases. As we compare the region where the temporal effects are dominant, shown in Fig. 24 in comparison to Fig. 14, the increase in the value of  $b$  is scarce and noncollinear phase matching geometry is not necessary under these circumstances.

Moreover, the effects of noncollinear phase matching geometry is even more pronounced in the case where  $w_{30} = 20 \text{ } \mu\text{m}$  and  $\Delta t_{30} = 5 \text{ ps}$ . As shown in Fig. 25 in comparison with Fig. 15, the values of  $b$  have increased substantially even for the case of  $l_c = 1 \text{ mm}$ . Even for the cases of  $\Delta t_{30} = 500 \text{ fs}$  and  $\Delta t_{30} = 50 \text{ fs}$ , shown in Figs. 26 and 27, respectively, in comparison with Figs. 16 and 17, there is still some increase in the values of  $b$  in virtually all different cases except for the case of  $w_{30} = 20 \text{ } \mu\text{m}$ ,  $\Delta t_{30} = 50 \text{ fs}$ , and  $\lambda_3 = 527 \text{ nm}$  where the temporal effects are most dominant.

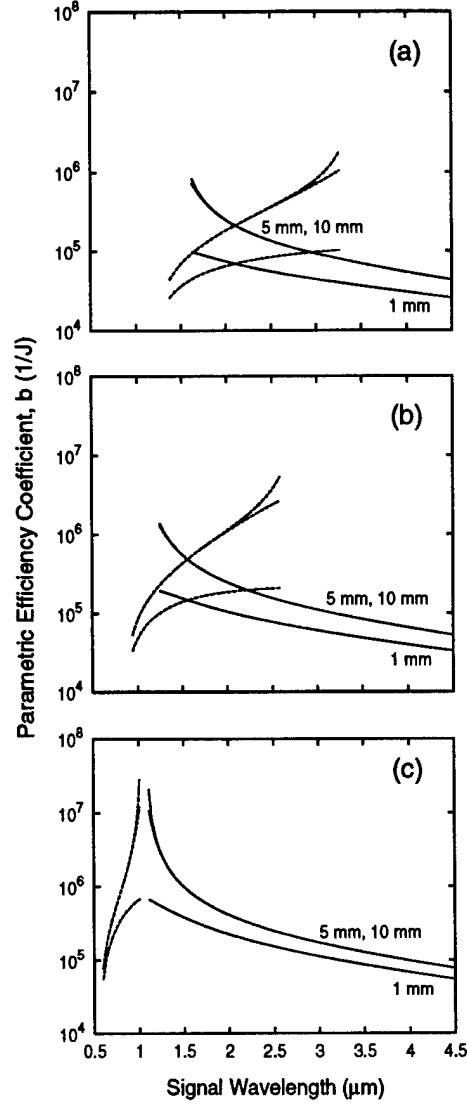


Figure 25: Parametric efficiency coefficient in KTP as a function of signal wavelength in the case of  $w_{30} = 20 \mu\text{m}$  and  $\Delta t_{30} = 5 \text{ ps}$  for three different pump wavelengths at (a)  $1.053 \mu\text{m}$ , (b)  $780 \text{ nm}$ , and (c)  $527 \text{ nm}$  using noncollinear phase matching geometry. The solid curves are for  $o \rightarrow o + e$  phase matching and the dashed curves are for  $o \rightarrow e + o$ .

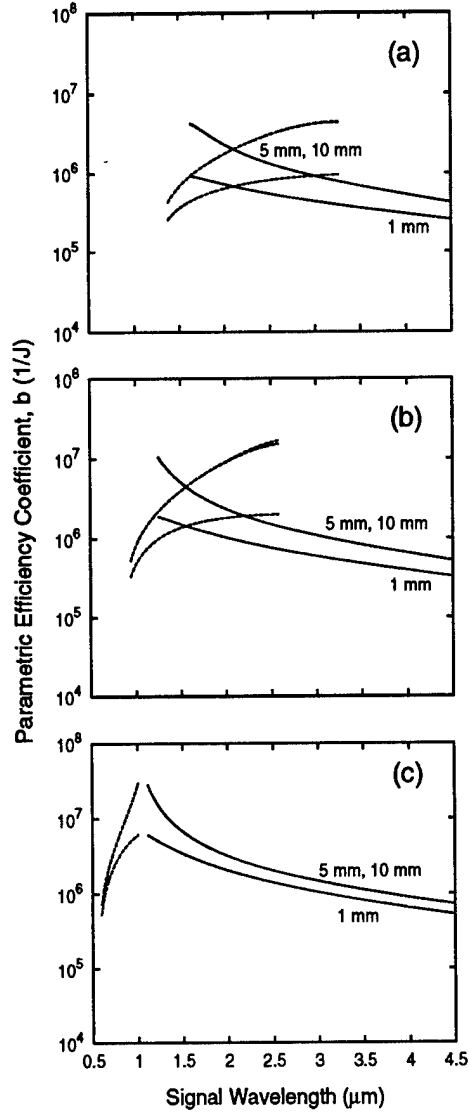


Figure 26: Parametric efficiency coefficient in KTP as a function of signal wavelength in the case of  $w_{30} = 20 \mu\text{m}$  and  $\Delta t_{30} = 500 \text{ fs}$  for three different pump wavelengths at (a)  $1.053 \mu\text{m}$ , (b)  $780 \text{ nm}$ , and (c)  $527 \text{ nm}$  using noncollinear phase matching geometry. The solid curves are for  $o \rightarrow o + e$  phase matching and the dashed curves are for  $o \rightarrow e + o$ .



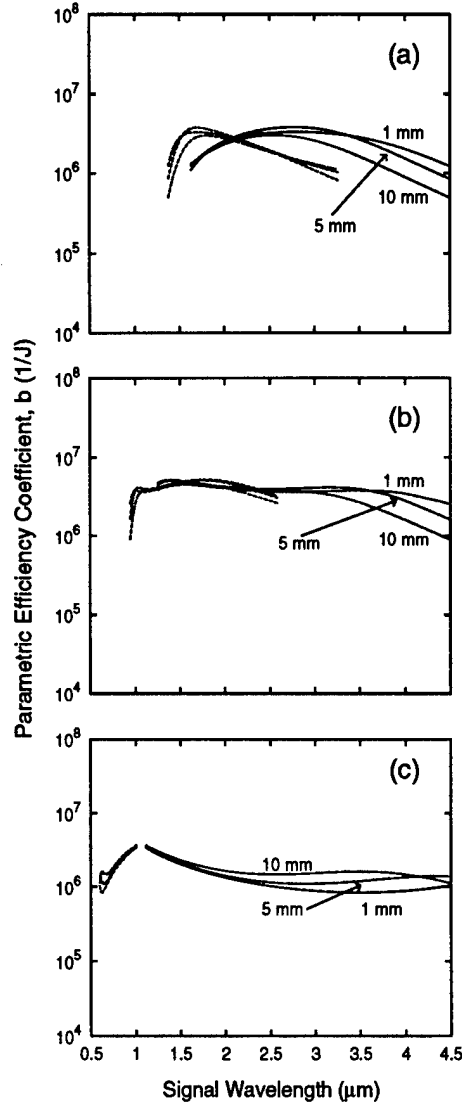


Figure 27: Parametric efficiency coefficient in KTP as a function of signal wavelength in the case of  $w_{30} = 20 \mu\text{m}$  and  $\Delta t_{30} = 50 \text{ fs}$  for three different pump wavelengths at (a)  $1.053 \mu\text{m}$ , (b)  $780 \text{ nm}$ , and (c)  $527 \text{ nm}$  using noncollinear phase matching geometry. The solid curves are for  $o \rightarrow o + e$  phase matching and the dashed curves are for  $o \rightarrow e + o$ .

## 4.0 Pump Laser System

Continuous wave (cw) mode-locked laser systems which generate repetitive short optical pulses with high peak power can be used in many scientific applications, e.g., pumping sources for synchronously pumped optical parametric oscillators (OPO), time-resolved spectroscopy, and electro-optic sampling. Therefore, the noise characteristics of cw mode-locked laser systems are very important in the study of ultrafast phenomena. In this section, the experimental setup and the noise characteristics of the pump laser system are discussed. The pump laser system used in the experiments is a Nd:YLF laser system which can be operated in two different mode-locking schemes: active mode-locking and additive-pulse mode-locking (APM). The differences of the noise characteristics between these two systems under cavity length detuning are also compared.

### 4.1 Experimental Setup

Figure 28 shows the schematic diagram of the experimental setup. The laser main cavity is a flashlamp-pumped Quantronix 416 Nd:YLF laser and the external cavity is formed by a beam splitter with a reflectivity of 90%, a 60-cm long optical fiber as the nonlinear medium, and a concave mirror as the retroreflector. When the external cavity is blocked, the laser can be actively mode-locked to generate pulses with 30 ps full width at half maximum (FWHM) pulsewidth at a repetition rate of 76 MHz while the useful average output power is 9 W. When the external cavity is unblocked, nearly transform-limited pulses with 6.4 ps FWHM pulsewidth at a repetition rate of 76 MHz can be generated by the self-starting APM process with an average output power of 9 W [56, 57]. Figure 29 shows the autocorrelation trace

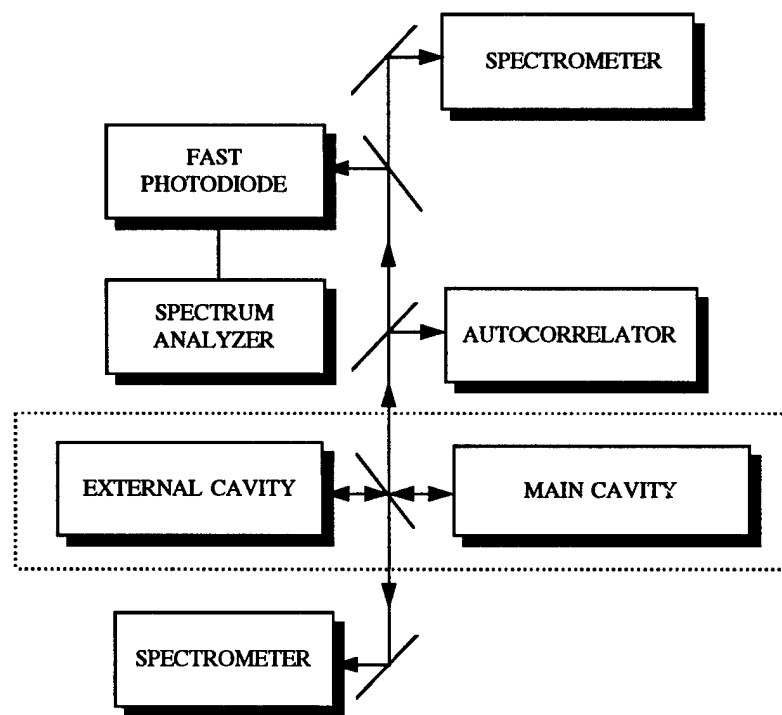


Figure 28: Schematic of the pump laser system and the measurement setup. Inside the dashed box is the pump laser.

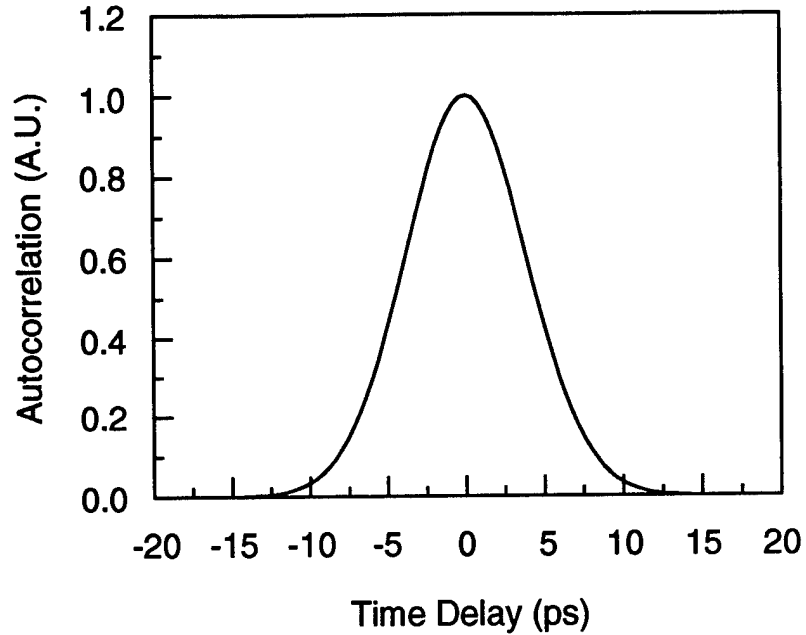


Figure 29: The autocorrelation trace of the APM Nd:YLF laser pulse.

of the APM pulse. Figure 30 shows the spectrum of the APM pulse. The FWHM spectral width is 0.3 nm. The time-bandwidth product is 0.52 assuming Gaussian pulse shape.

The tips of the fiber used in the external cavity were carefully polished with an angle to avoid reflection into the main cavity. In order to achieve the APM operation, the length of the external cavity has to be matched to that of the laser main cavity. A photodetector with 70 ps response time was used at the rear end of the laser to monitor the alignment of external cavity. The photodetector was attached to a sampling oscilloscope. When the coupling of the external cavity was

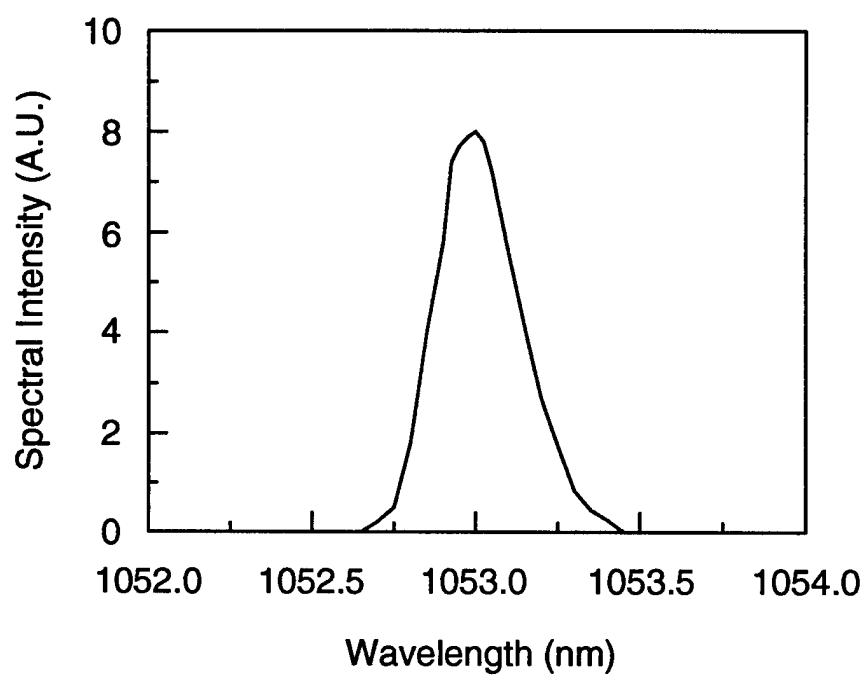


Figure 30: The spectrum of the APM Nd:YLF laser pulse.

optimized, the active mode-locker was turned on. Two pulses would be observed on the sampling oscilloscope. One pulse was the pulse generated by the main cavity and the other one was the pulse reflected back from the external cavity. By adjusting the position of the microscope objective lens and that of the input fiber tip, the alignment of the cavity length can be achieved. About 10% of the reflected power from the external cavity was used for second harmonic generation(SHG), the SHG signal was sent to a feedback circuit for active servo control of the main cavity length to maintain stable APM operation[57]. To avoid the mechanical vibrations from the water cooling system, the laser head is directly bolted down to the optical table[56].

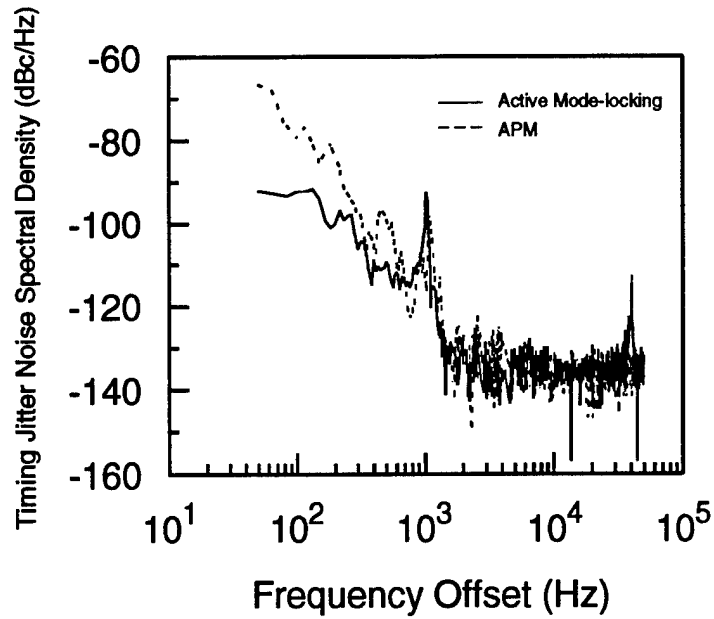
## 4.2 Noise Characteristics

In this section we describe the characterization of the noise behavior of our Nd:YLF laser systems using the power spectrum techniques. The power spectrum techniques [58, 59, 60, 61, 62, 63] are used to measure the laser amplitude noise and timing jitter (fluctuations in the arrival time of the pulses). Under the approximations that the timing jitter is small, that the amplitude noise and timing jitter are not correlated, and that the pulsewidth has no fluctuation, the power spectral densities of the laser pulse amplitude noise and pulse repetition timing jitter can be deduced from the power spectra measured with a photodetector and a spectrum analyzer. In the noise measurement the output pulses were sent to an autocorrelator for pulsewidth measurement and a *p-i-n* photodetector for noise spectrum measurement. The *p-i-n* photodetector, which has a 3-dB bandwidth larger than 3 GHz, was connected to a Hewlett-Packard 8560A spectrum analyzer.

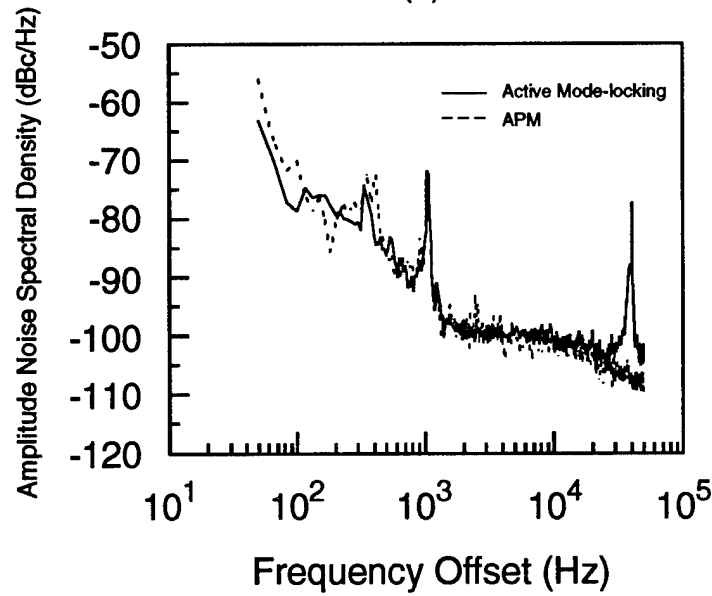
When the laser is operated in the APM mode, the optical spectrum of the reflected light from the external cavity was examined by a monochromator to determine the cavity length detuning[57].

We have measured the noise spectra of the actively mode-locked system and the APM laser system under zero cavity-length detuning. The noise power spectra of the 1st and 30th harmonics are measured. The resolution bandwidth,  $B$ , of the spectrum analyzer is 30 Hz for a frequency offset less than 5 kHz and is 300 Hz for an offset above 5 kHz. The single-sideband timing jitter noise spectra for both APM and active mode-locking are shown in Fig. 31(a). The timing jitter noise is seen to be higher when the laser is operated under APM than when it is under active mode-locking. The timing jitter noise in both cases rolls off rapidly at the frequency of about 1.5 kHz. Therefore, the timing jitter noise is dominated by the low-frequency components. The rms timing jitter,  $\sigma_J$ , for the laser is found to be 1.1 ps in the case of active mode-locking and 7.3 ps in the case of APM for the frequency range from 50 Hz to 1.5 kHz. The higher timing jitter in the APM case can be understood by the interferometrical nature of the APM process. The 7.3 ps rms timing jitter of the APM laser is smaller than the 14 ps rms result of the self-mode-locked Ti:sapphire laser[63] and is comparable to the 5-10 ps rms result of the CPM laser[64]. The 1.08 ps rms timing jitter of the actively mode-locked laser is considerably small since there is no active servo control of the cavity length. The small noise is due to the good isolation of laser head from mechanical vibrations.

The amplitude noise spectra[59], again for both active mode-locking and APM cases, are shown in Fig. 31(b). The amplitude noise spectral density of the actively mode-locked case is similar to that of the APM case except that there is a noise



(a)



(b)

Figure 31: (a) The single-sideband timing jitter noise spectra and (b) the single-sideband amplitude noise spectra of the Nd:YLF laser in both active mode-locking and APM operation modes in units of decibels below the carrier in a 1-Hz bandwidth.



peak at about 40 kHz in the active mode locking case. The rms amplitude fluctuation,  $\sigma_A$ [59], for both cases are calculated to be 0.83% and 0.85%, respectively, for the frequency range from 50 Hz to 1.5 kHz. The noise peak at 40 kHz is the relaxation oscillation frequency of this Nd:YLF laser. This peak appears in the case of active mode-locking but is absent in the case of APM. APM laser systems with a long fluorescence lifetime are prone to relaxation oscillation or self-Q-switching[65]. This has been the major difficulty of achieving stable APM operation in Nd:YAG and Nd:YLF lasers in comparison to lasers with shorter fluorescence lifetime, such as the Ti:sapphire laser. It can be seen from this measurement that the relaxation oscillation of our APM has been completely suppressed under stable operation conditions.

Actively mode-locked laser and APM laser have different noise characteristics under cavity length detuning. Figure 32 shows the noise power spectral densities  $L_{30}(f)$  of the 30th harmonic under cavity length detuning for both active mode-locking and APM cases. The cavity length mismatch is 100  $\mu\text{m}$  in both cases. In the active mode-locking case, relaxation oscillation begins to dominate the noise spectrum; consequently, the power spectrum method is no longer suitable for measuring the amplitude noise and timing jitter noise in this case since the small signal approximation is no longer valid. In contrast, relaxation oscillation is still suppressed under cavity length detuning in APM case. Stable APM operation can be maintained over a cavity detuning range from  $-400 \mu\text{m}$  to  $300 \mu\text{m}$ .

Figures 33(a) and (b), respectively, show the rms timing jitter  $\sigma_J$  and the rms amplitude noise  $\sigma_A$  of the APM laser measured over the cavity detuning range. The rms noise is calculated for the frequency range from 50 Hz to 1.5 kHz. A positive

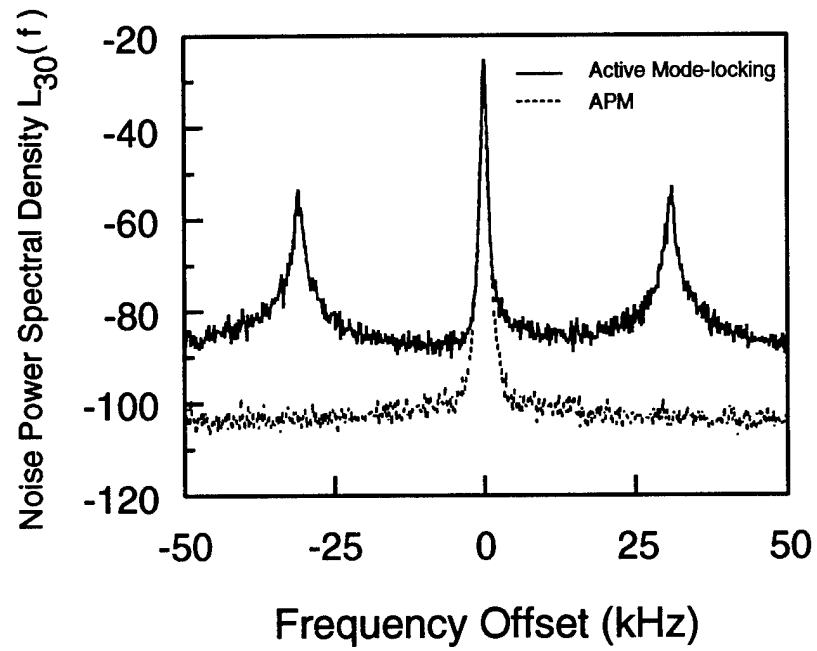
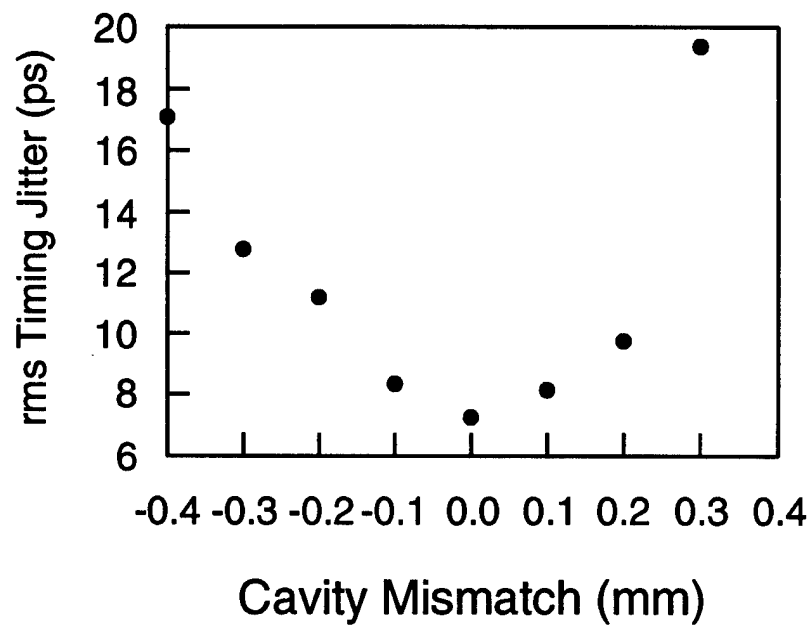
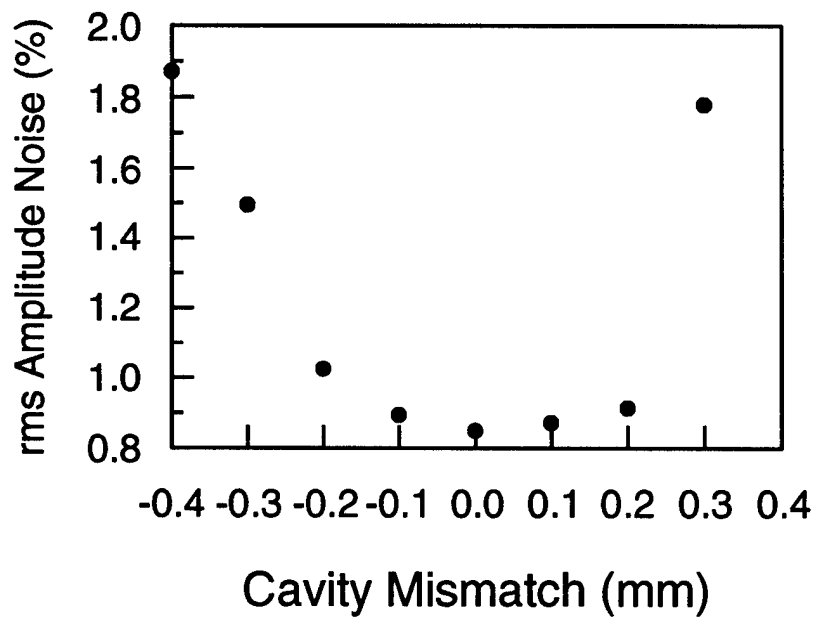


Figure 32: The noise power spectra of the 30th harmonic of the Nd:YLF laser under a cavity length detuning of  $100 \mu\text{m}$  for both active mode-locking and APM cases.



(a)



(b)

Figure 33: (a) The rms timing jitter and (b) the rms amplitude noise of the APM Nd:YLF laser as a function of cavity mismatch.

cavity mismatch means the external cavity is longer than the main cavity. Note that both the rms timing jitter and the rms amplitude noise have their minimum at zero cavity detuning, although the pulsewidth is not shortest at zero detuning [57]. The rms amplitude noise is less sensitive to the cavity mismatch than the rms timing jitter. Also the range of cavity mismatch is not symmetric. Although the pulsewidth gets shorter when cavity mismatch is varied from positive to negative values[57], it is better to operate the APM laser at the zero detuning point if precise pulse arrival time is required in the experiments.

In summary, the timing jitter and the amplitude noise of a Nd:YLF laser in both active mode-locking and APM modes have been characterized by using power spectrum techniques. The rms timing jitter of the APM mode under zero cavity detuning is about six times larger than that of the active mode-locking mode since APM is a passive mode-locking process with interferometrical nature. The amplitude noise characteristics of these two mode-locking schemes are similar. Most of the timing jitter and amplitude noise in both cases are in the frequencies below 1.5 kHz. The low-frequency noise characteristics of this laser system implies that when this laser is used to synchronously pump the optical parametric oscillators(OPO), the timing jitter of this laser system should not affect the efficiency of OPO since there is no gain storage time in OPOs and the build-up time of OPO is on the order of microseconds. Relaxation oscillation have been observed in the actively mode-locking case. Under cavity detuning, the noise spectra of the actively mode-locked laser are dominated by the relaxation oscillation. In contrast, relaxation oscillation is completely suppressed in the APM mode even under cavity detuning situation. The complete suppression of relaxation oscillation in the noise

spectra of the APM operation explains why our APM Nd:YLF laser has been so stable despite the fact that Nd:YLF laser has a fluorescence lifetime as long as 480  $\mu$ s.

Recently, we theoretically derived and experimentally demonstrated a method to further characterize the pulsewidth fluctuation noise of the cw mode-locked laser pulses. The method is given as an appendix at the end of this report.

## 5.0 AgGaS<sub>2</sub> Based Optical Parametric Oscillator

Among all the nonlinear crystals, AgGaS<sub>2</sub> has been known for its large transmission window which covers 0.5 to 13.2  $\mu\text{m}$  and its high nonlinearity. However, due to its low damage threshold, it is difficult to build a synchronously pumped OPO based on this crystal. Recently, Cheung *et al.* [16] first demonstrated a singly resonant AgGaS<sub>2</sub> OPO pumped by a continuous wave mode-locked Nd:YAG laser. Cheung's OPO produced wavelength-tunable optical pulses at 1.3  $\mu\text{m}$  and 5.5  $\mu\text{m}$  wavelength range. In this section, we discuss the efforts of the construction of a synchronously pumped OPO based on AgGaS<sub>2</sub> which was intended to produce wavelength-tunable optical pulses at 10-11  $\mu\text{m}$  range. Some experimental results are presented.

### 5.1 Nonlinear Crystal

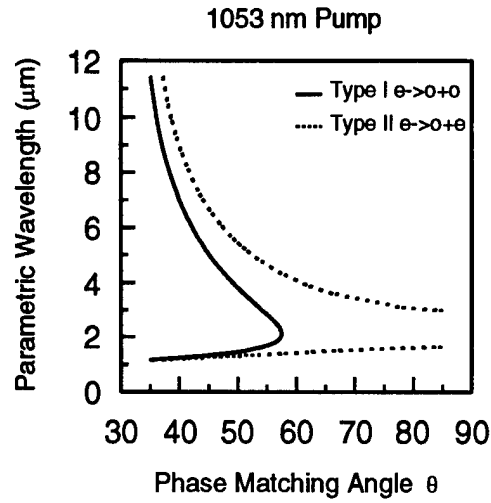
The nonlinear crystals used in this experiment are two  $5 \times 5 \times 10$  mm AgGaS<sub>2</sub> crystals. These AgGaS<sub>2</sub> crystals are cut at  $\theta = 38.01^\circ$  and  $\phi = 0^\circ$  for type II phase matching  $e \rightarrow o + e$ . The effective nonlinear coefficient  $d_{\text{eff}}$  is

$$d_{\text{eff}} = d_{14} \sin 2\theta \cos 2\phi. \quad (62)$$

The signal wavelength is 1.169  $\mu\text{m}$  and the idler wavelength is 10.6  $\mu\text{m}$  for the Nd:YLF pump wavelength of 1.053  $\mu\text{m}$ .

Figure 34 shows the calculated tuning curves for both Type I and II phase matching. It can be seen from Fig. 34 that there is a gap between 1.7  $\mu\text{m}$  and 2.71  $\mu\text{m}$  for Type II phase matching. However, for the same signal wavelength used in our experiment the Type I phase matching has a lower effective nonlinear

## AgGaS<sub>2</sub> Phase Matching Curve



$$\text{Type I : } d_{\text{eff}} = d_{14} \sin \theta \sin 2\phi = d_{14} \sin \theta$$

$$\text{Type II : } d_{\text{eff}} = d_{14} \sin 2\theta$$

Figure 34: Calculated tuning curves for Type I(Solid line) and Type II (Dotted line) phase matching of AgGaS<sub>2</sub> for the pump wavelength of 1053 nm

coefficient  $d_{\text{eff}}$  which is

$$d_{\text{eff}} = d_{14} \sin \theta \sin 2\phi, \quad (63)$$

where  $\theta$  is  $35.8^\circ$  and  $\phi$  can be chosen to be  $45^\circ$ .

In comparison with Cheung's experiment, our OPO is in a less favorable situation because our signal and idler are far away from the degeneracy point and the crystal has a large absorption coefficient around the idler range of 10-11  $\mu\text{m}$ . Transmission through both crystals at pump and signal wavelengths is measured to be 92%(92.8%) and 92% (92.9%), respectively. These values are roughly 4% less than those in Cheung's experiment. The poor transmission could lead to a higher threshold for the OPO. The gain bandwidth has been estimated to be 0.36 nm by using the equation

$$\delta\omega = \frac{2\pi c/l}{n_1 - \lambda_1(\frac{\partial n_1}{\partial \lambda})_{\lambda_1} - n_2 + \lambda_2(\frac{\partial n_2}{\partial \lambda})_{\lambda_2}}. \quad (64)$$

The angular tolerance is calculated to be 2.09 mrad for the signal wavelength at 1.16  $\mu\text{m}$ . The dispersion between pump and signal is calculated to be 1.65 ps/cm and that between pump and idler is calculated to be 9.67 ps/cm.

The pumping threshold can be estimated from the threshold condition[44]

$$g_{\text{th}}^2 l_c^2 = \frac{8\Gamma_2 n_2 l}{c} \quad (65)$$

where

$$g_{\text{th}}^2 = \frac{16\pi^2 \omega_1 \omega_2}{n_1 n_2 c^2} \chi_{\text{eff}}^2 E_{\text{th}}^2 \quad (66)$$

$$= \frac{16\pi^2 \omega_1 \omega_2}{n_1 n_2 c^2} \chi_{\text{eff}}^2 \frac{2\pi}{n_3 c} I_{\text{th}}, \quad (67)$$

$$\Gamma_2 = \frac{c}{n_2} \frac{1}{2l} \ln \frac{1}{RT}, \quad (68)$$

$$\chi_{\text{eff}} = \chi_{14} \sin 2\theta, \quad (69)$$



$l_c$  is the crystal length,  $l$  is the cavity length,  $R$  is the reflectivity of the output coupler, and  $T$  is the transmittance of the crystal at the signal wavelength. From the equation above, we can find the relationship between the threshold intensity and all the physical parameters in our case:

$$I_{th} \propto n_1 n_2 n_3 \lambda_1 \lambda_2 \frac{1}{\sin^2 2\theta} \ln \frac{1}{RT}. \quad (70)$$

Using the estimation above, for the same pump pulsewidth the power threshold for our OPO is about 1.9 times higher than that in Cheung's experiment, *i.e.*, the average power threshold of our OPO would be 5.7 W and 1.2 W for pulses with pulsewidths of 30 ps and 6.4 ps at the repetition rate of 76 MHz, respectively.

## 5.2 Experimental Setup

Figure 35 shows the experimental setup of the AgGaS<sub>2</sub> OPO. The pump source is a Quantronix 416 Nd:YLF laser which can be operated in two modes: (1) cw actively mode-locked mode which can generate 30 ps pulses at 76 MHz with an average power of 9.5 W (2) Additive-pulse mode-locked mode which can generate 6 ps pulses at 76 MHz with an average power of 10 W. A half-wave plate was used to control the incident pump polarization. Two lenses of 50 and 100 cm focal length were used to mode-match the pump with the signal in the OPO cavity. The  $1/e^2$  beam spot size of the pump at the crystal could be varied from 150 to 200  $\mu\text{m}$ . A 1:10 chopper was used to modulate the pump in order to prevent the possible damage to the crystal. The OPO cavity was a bow-tie ring cavity which consisted of two curved mirrors and two flat mirrors to reduce loss and retro-reflect. The radius of curvature of the curved mirrors was 120 cm. The beam waist of the signal

### AgGaS<sub>2</sub> OPO setup

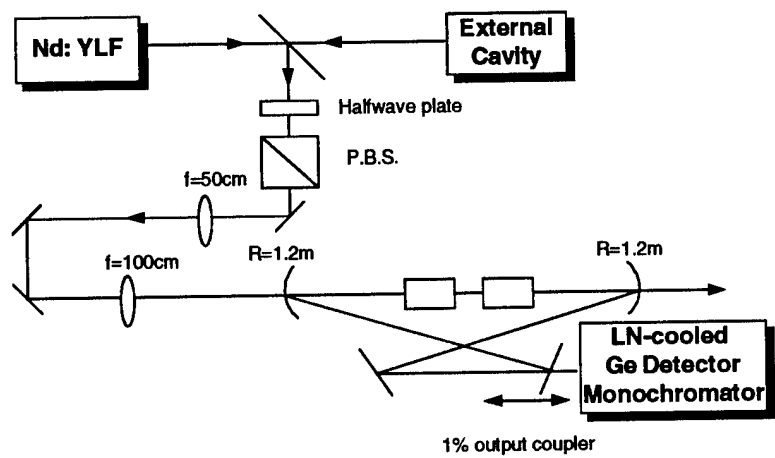


Figure 35: The experimental setup of the silver thiogallate OPO

could be varied from 110 to 330  $\mu\text{m}$  by changing the separation between the two curved mirrors from 120.5 cm to 160 cm. The two curved mirrors were coated to have high transmission (HT) at the 1.053  $\mu\text{m}$  pump wavelength and high reflection (HR) at the 1.169  $\mu\text{m}$  signal wavelength. One flat mirror was also HR coated at the signal wavelength. The other flat mirror was a 99% output coupler for the signal. Although the curved mirror was HT coated at the pump wavelength, only 7.5 W of pump could be delivered to the crystal due to the losses from all the optical components. The crystals were mounted on rotational stages in order to tune their angles. Both single crystal and double crystal configurations have been tried.

### 5.3 Results

The OPO cavity was aligned by monitoring the parametric fluorescence which was detected by a liquid-nitrogen cooled Ge detector and lock-in amplifier combination. A WO1414 low pass filter and a tilted 1.064  $\mu\text{m}$  HR mirror were used to filter out the pump wavelength. The parametric fluorescence could be tuned from 1.16  $\mu\text{m}$  to 1.185  $\mu\text{m}$  by tuning the crystal angle. A multiple pass versus single pass enhancement factor of 7 has been observed. However, no oscillation has been achieved either using the actively mode-locked laser pulses or using the APM laser pulses. The cavity length was also measured by a 1.16  $\mu\text{m}$  pulse train which was the second order Raman signal from a 400 m polarization preserving fiber pumped by the 1.053  $\mu\text{m}$  pump. As we discussed above, the average power threshold of our OPO should be higher than that in Cheung's experiment because the higher loss in our crystals and the intrinsic lower parametric gain.

In order to have better understanding of the parametric process in this crystal, we tried to setup a difference frequency generation (DFG) experiment by mixing the 1.053  $\mu\text{m}$  and the 1.16  $\mu\text{m}$  second order Raman from the fiber in the crystal. The pump was first sent through the crystal and a ZeGe beam splitter which transmitted almost 75% of the pump and reflected 70% of the 10.6  $\mu\text{m}$ . After the beam splitter, the pump was coupled into the fiber by using the microscope object lens and two lenses with focal length of 75 cm and 30 cm, respectively. 3 W of pump was coupled into the fiber. After the fiber, the light was sent through a delay line which consists of two prisms and a motorized translation stage. Time domain synchronization was achieved by monitoring the pump and Raman pulses on a sampling oscilloscope. The idler wavelength is 11.41  $\mu\text{m}$  and the average idler power is estimated by the following equation

$$P_3 = \frac{32\pi^5}{c\lambda_3^2 n_1 n_2 n_3} \chi_{\text{eff}}^2 z^2 \frac{P_1 P_2}{A} \quad (71)$$

where 1, 2, and 3 correspond to the signal, idler, pump and  $P$  is the peak power,  $n$  is the index of refraction,  $\lambda$  is the wavelength,  $z$  is the crystal length, and  $A$  means the spot area. The nonlinear coefficient  $\chi_{\text{eff}}$  can be represented by the  $d_{\text{eff}}$  as followed

$$\chi_{\text{eff}}(\text{esu}) = 2 \times d_{\text{eff}}(\text{mks}) \times \frac{3 \times 10^4}{4\pi}. \quad (72)$$

With pump power of 7.5 W and 1.16  $\mu\text{m}$  power of 500 mW, 7 mW of 11.41  $\mu\text{m}$  mid-infrared can be generated by a 1 cm crystal with the pump and signal spot size of 160  $\mu\text{m}$ . However, the bandwidth of the 1.16  $\mu\text{m}$  Raman light is around 10 nm which is almost 30 times larger than the gain bandwidth of the crystal. Therefore, at most 200  $\mu\text{W}$  mid-infrared light can be obtained by DFG. Due to the limitation

of the available equipment in our laboratory, the mid-infrared  $11.41\ \mu\text{m}$  light is detected by a Gentec pyroelectric joule meter and lock-in amplifier. However, the sensitivity of this detection system is calibrated to be only  $16\ \mu\text{W}$  by using the  $1\ \mu\text{m}$  light. No mid-infrared signal has been observed. There are two possible reasons why we did not observe the mid-infrared signal. First, the detection system is not sensitive enough and is too noisy. Second, in the calculation above, loss of the crystal and dispersion have not been taken into account.

Although  $\text{AgGaS}_2$  provides a possibility to extend the tunable optical source to mid-infrared range, due to the intrinsic disadvantage of the parametric process and the strong absorption at the idler wavelength range, crystals with better quality and more powerful pump sources are needed to explore the mid-infrared region. Injection seeded OPO could be a possible solution if a narrower linewidth seed source is available.

## 6.0 Picosecond KTP Optical Parametric Oscillator

The design and characteristics of a  $\text{KTiOPO}_4$  singly resonant optical parametric oscillator synchronously pumped by the second harmonic of an additive-pulse mode-locked Nd:YLF laser are discussed in this section. The pump pulses at 527 nm wavelength have a pulsewidth of 4.5 ps, a repetition rate of 76 MHz, and an average power up to 4 W. Above the threshold of 900 mW average pump power, continuous tuning is demonstrated from 851 to 938 nm in the signal branch and from 1200 to 1381 nm in the idler branch. At three times the threshold, 3.2 ps signal pulses with an average power of 83 mW and 2.4 ps idler pulses with an average power of 280 mW are obtained. High-order transverse mode characteristics and multiple-wavelength oscillation are also discussed.

### 6.1 Introduction

Among the existing synchronously pumped OPOs,  $\text{KTiOPO}_4$  (KTP) is the most commonly used crystal for the nonlinear gain medium because of its high nonlinear coefficient. Edelstein *et al.*[17] and Wachman *et al.*[66] first demonstrated a KTP-based singly resonant mode-locked OPO synchronously pumped inside a colliding-pulse mode-locked dye laser. A doubly resonant KTP OPO pumped by the second-harmonic of a cw mode-locked diode-laser-pumped Nd:YLF laser was reported by Ebrahimzadeh *et al.*[7]. The first externally synchronously pumped OPO was demonstrated by Mak *et al.*[19] where the pump laser used was a hybridly mode-locked dye laser. McCarthy *et al.*[8] and Grässer *et al.*[10] reported singly

resonant KTP OPOs synchronously pumped by the second harmonic of diode-laser-pumped additive-pulse mode-locked (APM) and actively mode-locked Nd:YLF lasers. The KTP crystals were both cut in the  $xy$ -plane for quasi-noncritical phase matching, and the wavelength tuning range is roughly 940-1180 nm. With the development of self-mode-locked Ti:sapphire laser, many KTP OPOs have been reported[20, 21, 9, 24], which covered  $\sim 1050$ -1370 nm and  $\sim 1780$ -2870 nm spectral range. Chung *et al.*[11] and Grässer *et al.*[10] demonstrated cw mode-locked KTP OPOs synchronously pumped by a compressed actively mode-locked Nd:YAG laser and an actively mode-locked Nd:YLF laser, respectively. The output can be tuned over 1570-1590 nm and 3210-3300 nm.

In this section, the characteristics of a singly resonant KTP OPO synchronously pumped by the second harmonic of a flashlamp-pumped APM Nd:YLF laser are discussed. The KTP crystal was cut in the  $xz$ -plane which potentially allows the wavelength tuning range to cover most of the transparency window of the KTP crystal from 600 to 4500 nm. The uniqueness of our pump system is that we can generate  $\sim 4.5$  ps mode-locked pulses at 527 nm with an average power up to 4 W, thus overcoming the high threshold of the OPO with KTP in this particular phase matching plane. In Section 6.2 the experimental layout is discussed. In Section 6.3 the general characteristics of the OPO is presented. Comparison between the experimental results and previous theoretical simulations[4, 5] is made. In Section 6.4, we discuss the characteristics of high-order transverse mode and multiple-wavelength oscillation in the OPO. Discussions and summary are given in Section 6.5.

## 6.2 Experimental Setup

A schematic diagram of the OPO setup is shown in Figure 1. The pump source is a flashlamp-pumped APM Nd:YLF laser at 1053 nm wavelength with 9 W of average output power at a repetition rate of 76 MHz and a pulsewidth of 6.4 ps[56]. These pulses were frequency-doubled using a hydrothermally-grown KTP cut in the  $xy$ -plane at  $\phi = 35^\circ$ . The crystal dimensions of the KTP are  $3 \times 3 \times 5$  mm. Pulses at 527 nm with a pulsewidth of 4.5 ps and an average power up to 4 W were generated for pumping the OPO. Figure 36 and Fig. 37 show the autocorrelation trace and the spectrum of the 527 nm pulse, respectively. The FWHM spectral width is 0.13 nm and the time-bandwidth product is 0.64 assuming Gaussian pulse shape.

However, long-term operation of the second-harmonic generation(SHG) at such high power is still quite difficult due to the gray track problem of the KTP crystal. Therefore, we chopped the fundamental beam of the Nd:YLF laser with a 10:1 duty cycle for the protection of the SHG KTP crystal during most of the experiment. Two lenses of 12.5 cm focal length were used to couple the pump into the OPO cavity. The pump Gaussian beam waist in the crystal was about  $20 \mu\text{m}$  and the confocal parameter was approximately equal to the OPO KTP crystal length of 5 mm.

The resonator of the OPO was chosen to be a ring cavity in order to reduce the signal loss and the retro-feedback problem. The radius of curvature of the two curved mirrors was 20 cm. The Gaussian beam waist of the signal beam was calculated to be  $26 \mu\text{m}$  in order to give the same confocal parameters as the  $20 \mu\text{m}$  pump beam. The incidence angle on the curved mirror is  $\sim 2.5^\circ$ . The two curved mirrors have a reflectivity of 99.9% centered at the signal wavelength (890 nm) and



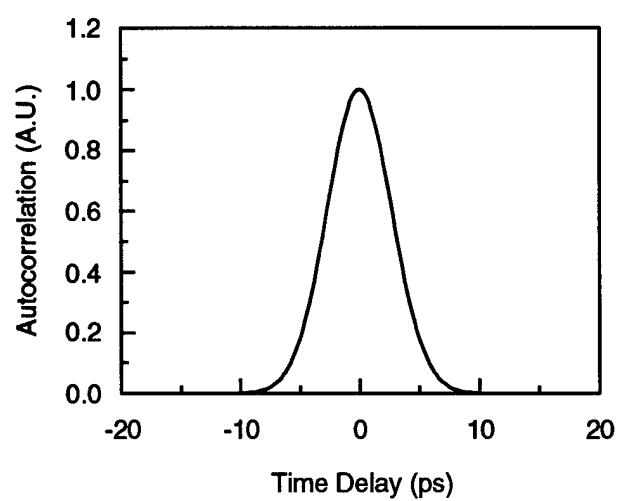


Figure 36: The autocorrelation trace of the 527 nm pump pulse

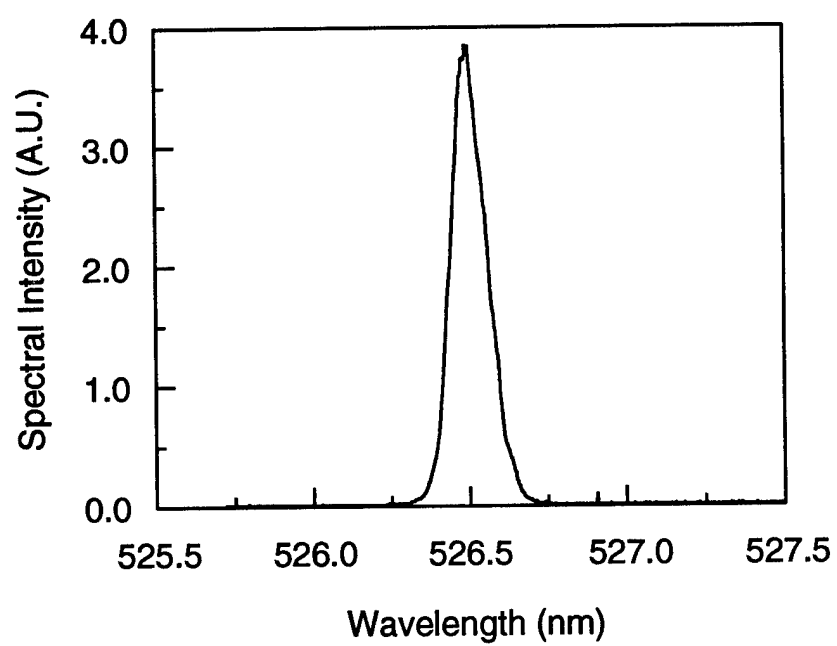


Figure 37: The spectrum of the 527 nm pump pulse

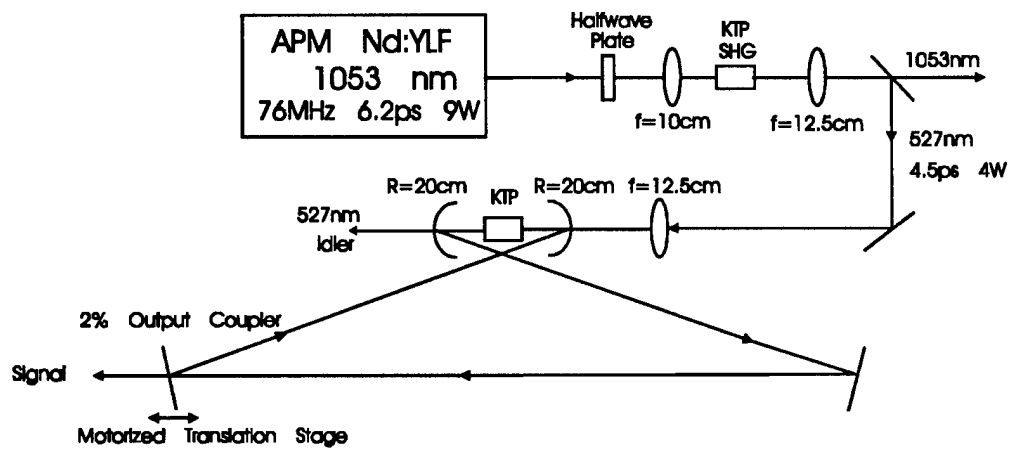


Figure 38: Schematic of the KTP OPO setup.

a transmissivity of 90% at the 527 nm pump wavelength. One of the two plane mirrors also has a reflectivity of 99.9% at the signal wavelength. The other plane mirror is a 2% output coupler which is mounted on a motorized translation stage for fine tuning of the cavity-length.

Collinear phase matching can be achieved in the  $xy$ ,  $xz$ , or  $yz$ -plane in KTP for the 527 nm pump wavelength. Figure 39 shows the parametric wavelength-tuning curves for KTP pumped at 527 nm (left) and 1053 nm (right) as a function of phase matching angle for different crystal cuts to phase match in the  $xy$ ,  $xz$ , and  $yz$ -planes, respectively. Among the three possibilities, phase matching in the  $xy$ -plane has a limited tuning range due to the low birefringence in this plane[14]. Phase matching in the  $xz$ - or  $yz$ -plane allows tuning over most of the transparency range of the KTP crystal, except that the tuning curve in the  $xz$ -plane has a gap near degeneracy point[67]. Another advantage of phase matching in the  $xz$  or  $yz$ -plane is that the signal wavelength change is more sensitive to the change in the phase matching angle in comparison with phase matching in the  $xy$ -plane. However, existing synchronously pumped KTP-based OPOs with the pump wavelength at 527 nm all have phase matching in the  $xy$ -plane[8, 10]. This is because phase matching in the  $xz$ - or  $yz$ -plane for widely tunable operation has a higher threshold for the OPO mainly due to the small effective interaction length as a result of the large Poynting-vector walk-off in these phase-matching planes[14]. We overcome this problem by using more intense pump radiation. Since the effective nonlinear coefficient of a given signal wavelength for the phase matching in the  $xz$ -plane is higher than that in the  $yz$ -plane[67], phase matching in the  $xz$ -plane was chosen for our experiment.

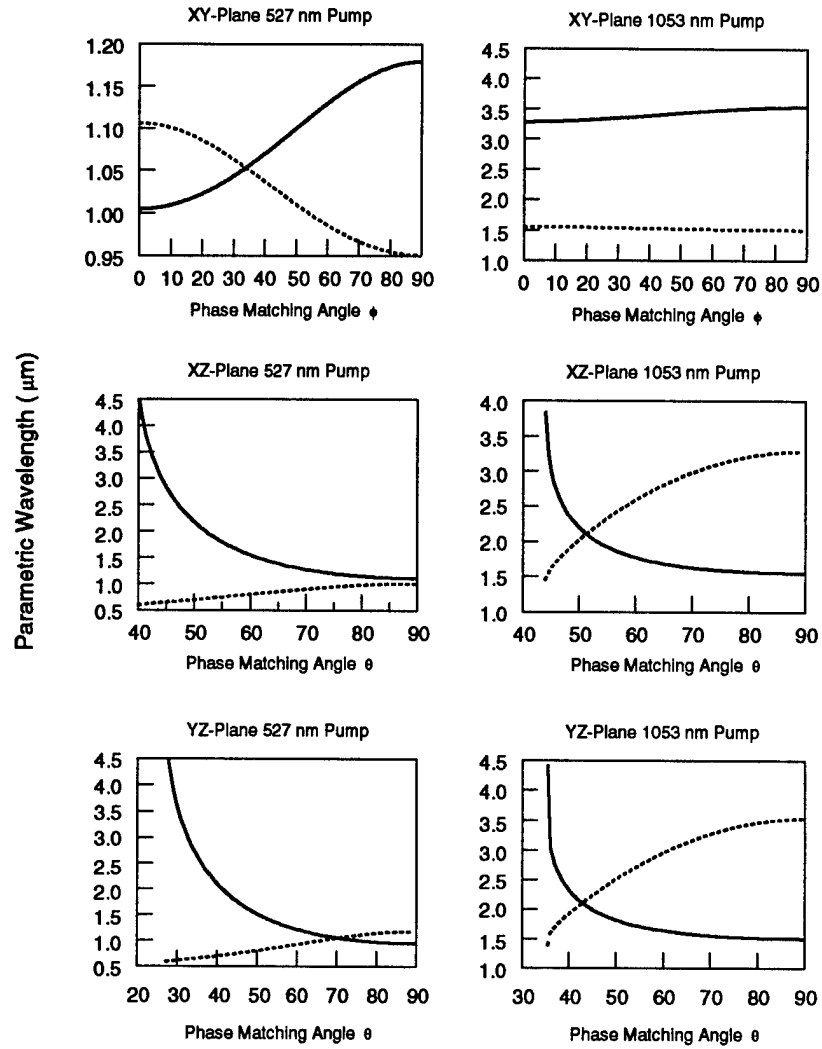


Figure 39: Parametric wavelength-tuning curves for KTP pumped at 527 nm(left) and 1053 nm(right) as a function of phase matching angle for different crystal cuts to phase match in the  $xy$ -,  $xz$ -, and  $yz$ -planes, respectively.

The OPO gain medium is a flux-grown KTP crystal which is cut in the  $xz$ -plane at  $\theta = 69^\circ$  and  $\phi = 0^\circ$  for type-II( $o \rightarrow e + o$ ) collinear phase matching, in which the 527 nm pump beam and the 1291 nm idler are polarized along the  $y$ -axis and the 890 nm signal is polarized in the  $xz$ -plane. The idler near 1300 nm wavelength range is useful for the study of the characteristics of the fiber-communication devices and systems. The crystal dimensions were  $3 \times 3 \times 5$  mm. The surfaces of the OPO KTP crystal were antireflection-coated at the signal wavelength. The reflection and absorption losses at 527 nm were measured to be 7% and 2.7%, respectively. The reflection and absorption losses at the signal and idler wavelengths were not measured due to the lack of available light sources. The effective nonlinear coefficient in the  $xz$ -plane is  $d_{24}\sin\theta$ . The nonlinear coefficient  $d_{24}$  was measured to be 4.1 pm/V from the spectral brightness of parametric fluorescence[68].

The alignment of the OPO was accomplished by monitoring the parametric fluorescence leaking from the output coupler with a liquid-nitrogen-cooled Ge detector mounted on a monochromator. The responsivity of the Ge detector is  $4 \times 10^8$  V/W. The alignment was started with angular adjustment of the mirrors. The four cavity mirrors were adjusted so that the parametric fluorescence was enhanced. After the angular adjustment was optimized, the position of the output coupler was changed by moving the translation stage to achieve oscillation.

### 6.3 Characteristics of OPO

The OPO output power versus pump power is shown in Fig. 40. The average power is defined as the average power during the opening time window of the chopper. No

change in the average power was observed when the duty cycle of the chopper was changed to 4:1 and 20:1. Due to the Fresnel losses of the optics and the reflection loss of the crystal, only 72.5% of the available pump power was sent into the OPO crystal.

With 2.9 W of 527 nm pump power sent into the OPO crystal, about 83 mW of signal and 288 mW of idler were generated at the output coupler and at the second curved mirror, respectively. The average pump power at threshold was 900 mW. According to recent theoretical analysis[69], the average pump power threshold was calculated to be about 760 mW. The higher power threshold observed in the experiment indicates a estimated total cavity loss of 2.4% per round trip, of which 2.0% was from the output coupler and 0.4% was possibly due to the three highly reflective mirrors and the losses from the KTP crystal. The total conversion efficiency was about 13 %. The total slope efficiency was approximately 19 %.

Figure 41 shows the total signal efficiency and the total idler efficiency versus the average pump power. The total signal efficiency and the total idler efficiency are defined as the percentage of the output signal power to the input pump power and that of the output idler power to the input pump power, respectively. The total signal efficiency peaks at about two times the threshold and then decreases with increasing pump power. The total idler efficiency is higher than the total signal efficiency and begins to saturate after the pump power is larger than about two times the threshold. Although the signal efficiency depends on the reflectivity of the output coupler, no attempt has been made to further improve the signal efficiency due to the lack of available output couplers with different reflectivities.

Figure 42 shows the percentage of pump depletion and the total conversion

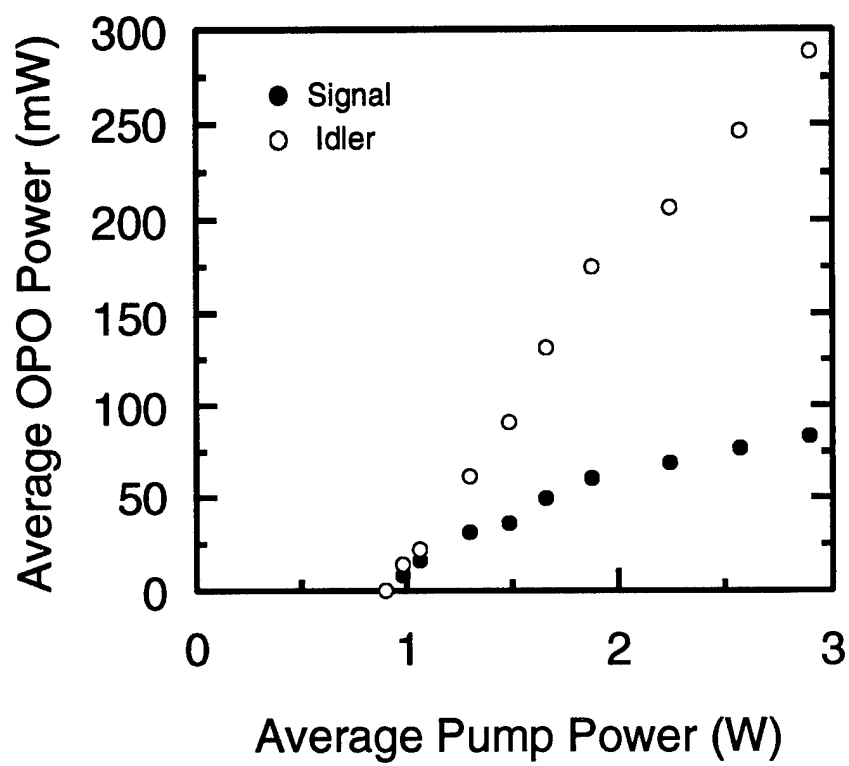


Figure 40: The average signal and idler output power versus the average pump power sent into the KTP crystal.



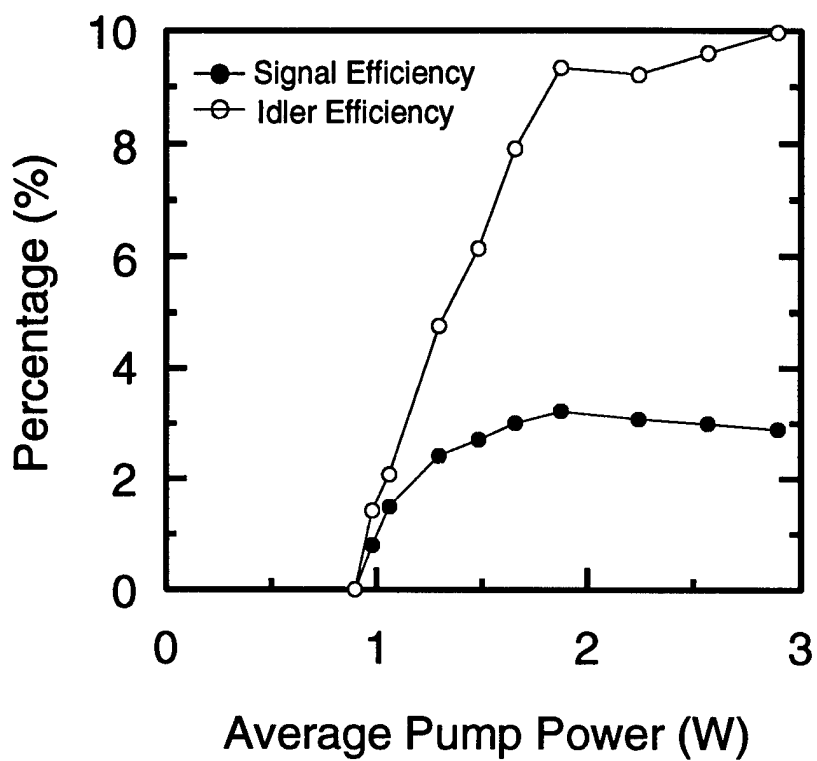


Figure 41: The total signal and idler efficiency versus the average power sent into the KTP crystal.

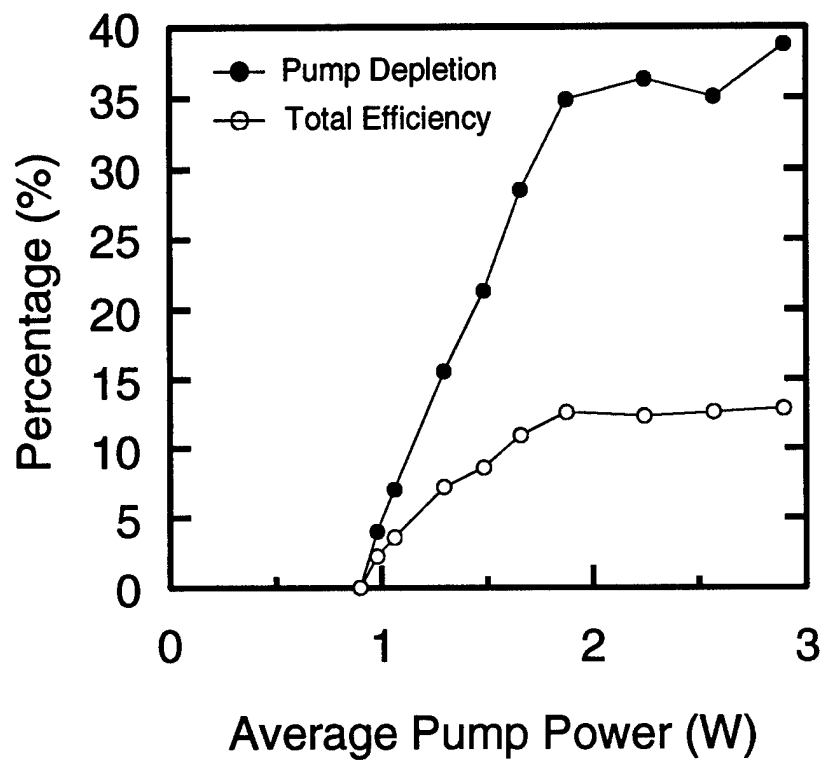


Figure 42: The percentage of pump depletion and total conversion efficiency versus the average power sent into the KTP crystal.

efficiency versus pump power. The amount of pump depletion was deduced by measuring the average power of the transmitted pump beam when the OPO oscillated and when the OPO was blocked from oscillation. The percentage of pump depletion and the total conversion efficiency both saturate after the pump power is larger than about two times the threshold. The highest pump depletion percentage was about 38 %, which implies the parametric conversion is very efficient inside the cavity. However, the highest total conversion efficiency was only 13 %. Absorption and scattering losses of the crystal and mirrors are the possible reasons leading to the low conversion efficiency. From the experimentally measured ratio of the output idler power to the output signal power, the additional intracavity signal loss can be estimated. The estimated additional intracavity signal loss at three times the threshold was 7 %, which is much larger than the 0.4 % additional intracavity signal loss estimated from the power threshold. The exact mechanism responsible for the discrepancies between the pump depletion and the total conversion efficiency is still under investigation.

The autocorrelation curves of the signal and idler pulses at highest OPO output power are shown in Figs. 43(a) and (b), respectively. The autocorrelation curves were better fitted by assuming a Gaussian pulse shape than a  $\text{sech}^2$  pulse shape. Assuming a Gaussian pulse shape, the signal pulse had a full-width at half-maximum(FWHM) pulsewidth of 3.2 ps and idler pulsewidth was 2.4 ps FWHM. The signal and idler spectra shown in Figs. 44(a) and (b), respectively, were measured with a monochromator of  $\sim 0.06$  nm resolution. The shape of spectra is not symmetric. The FWHM spectral widths were 0.5 nm and 1.1 nm for signal and

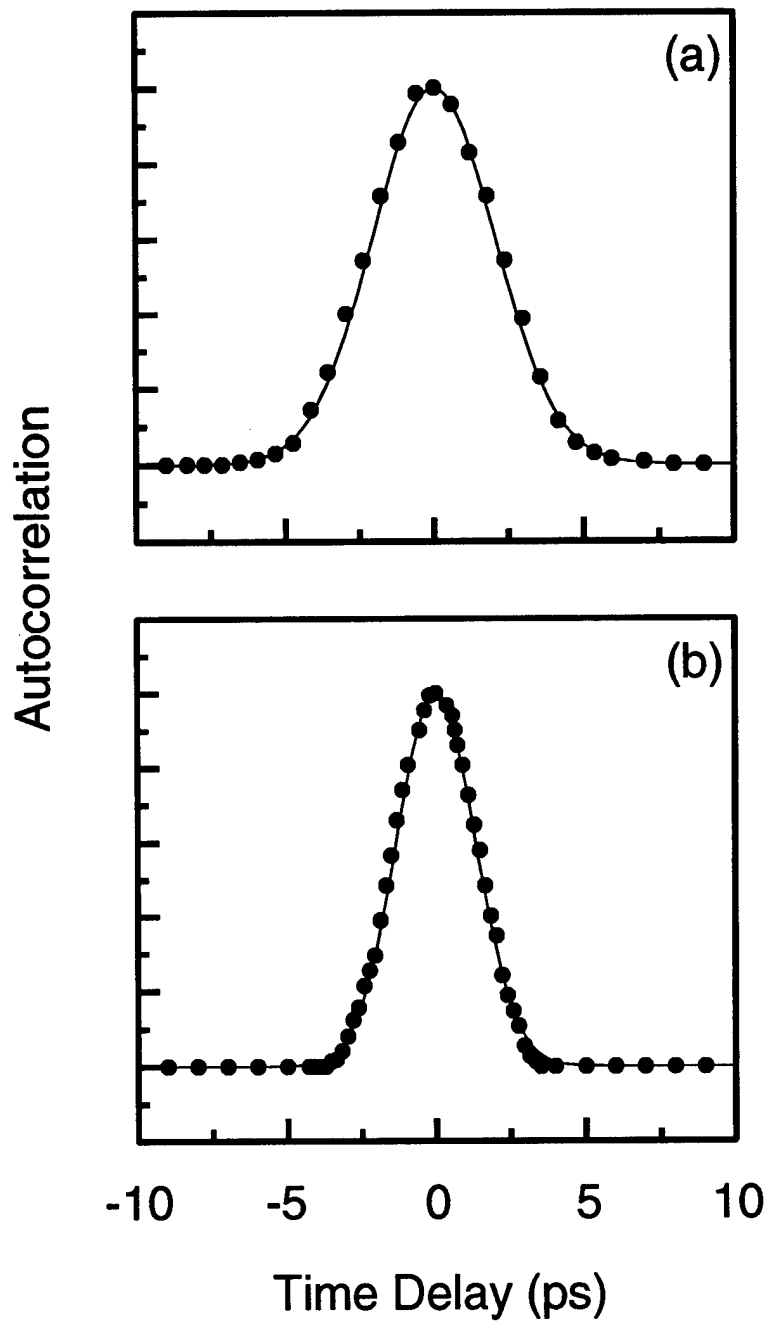


Figure 43: The background-free autocorrelation of (a) the signal pulses at the wavelength of 889 nm and (b) the idler pulses at wavelength of 1292 nm. The dots correspond to the experimental data; the solid line is the theoretical fitting curve assuming a Gaussian pulse shape.

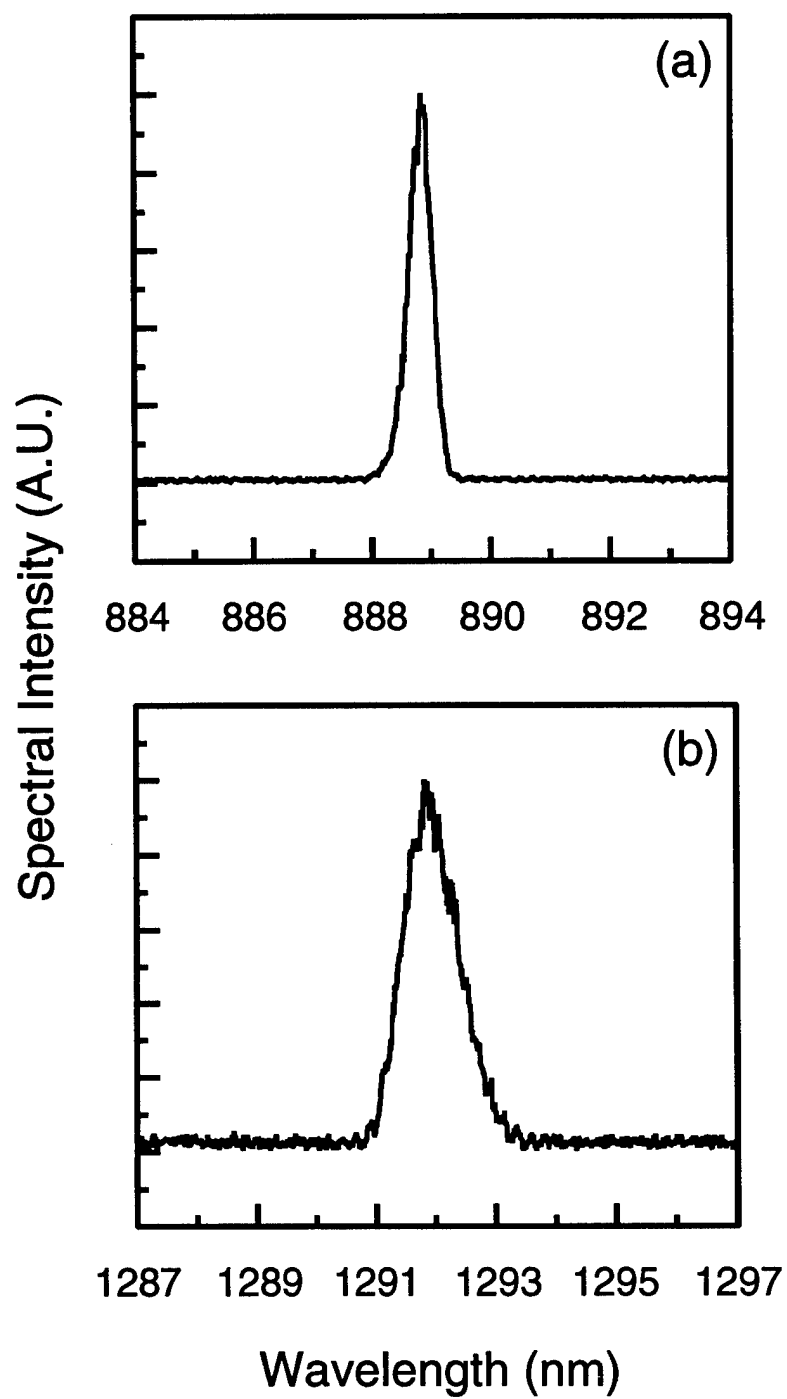


Figure 44: Spectrum of (a) the signal pulses at the wavelength of 889 nm and (b) the idler pulses at the wavelength of 1292 nm.

idler, respectively. The time-bandwidth product of the signal pulse is 0.61, corresponding to 1.39 times the transform-limited value for a Gaussian pulse shape, while that of the idler pulse is 0.47, which is only 1.07 times the transform limit. The spatial profile of the signal was a TEM<sub>00</sub> mode. Figure 45 shows the TEM<sub>00</sub> mode signal output power versus the OPO cavity length detuning when the OPO was operated at three times the threshold. In Figure 45, positive detuning means the OPO cavity is shorter than the pump laser cavity and the zero detuning point is chosen to correspond to the peak of the signal output power. The shape of the detuning curve is asymmetric. The 6.75  $\mu\text{m}$  FWHM detuning range, which corresponds to a 45 fs round-trip time mismatch, is in quantitative agreement with previous simulation[4].

The wavelength tuning of our OPO is achieved by rotating the KTP crystal about the  $y$ -axis. The calculated tuning curve and experimental data are both shown in Fig. 46. The experimental data are in good agreement with the calculated tuning curve[67]. We achieved 87 nm tuning range in the signal branch(851-938 nm) and 181 nm tuning range in the idler branch(1381-1200 nm) by rotating  $\sim 10^\circ$  internal angle. The tuning range was limited by the mirror coatings and the reduction of the effectiveness of the antireflection coatings of the OPO crystal caused by the crystal rotation. The wavelength tuning range is relatively large in comparison with the KTP OPO phase-matched in the  $xy$ -plane[8] due to the high birefringence of KTP in  $xz$ -plane.

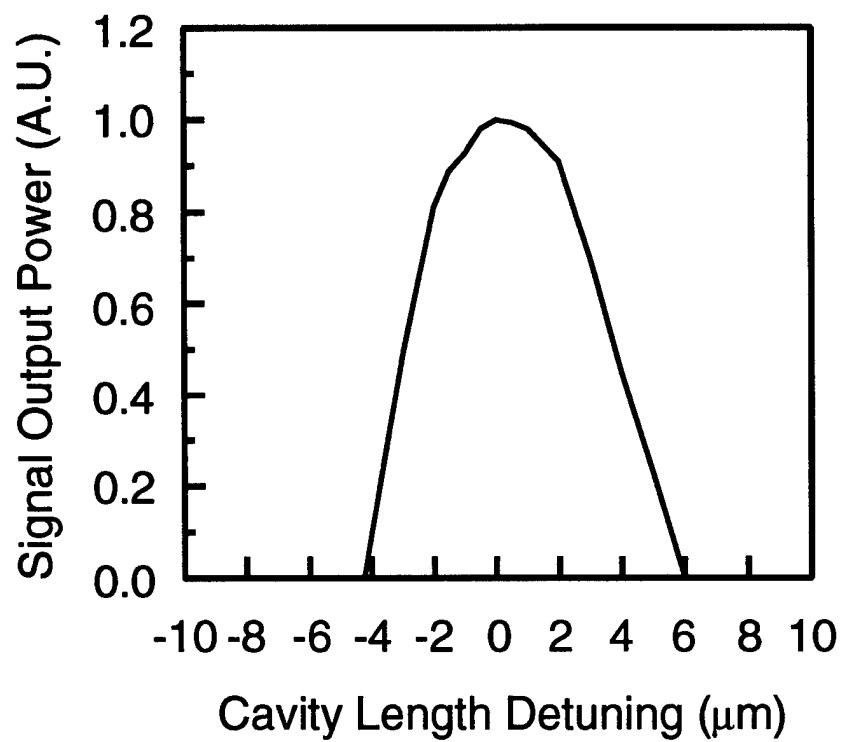


Figure 45: The single-wavelength TEM<sub>00</sub> mode signal output power as a function of cavity-length detuning.

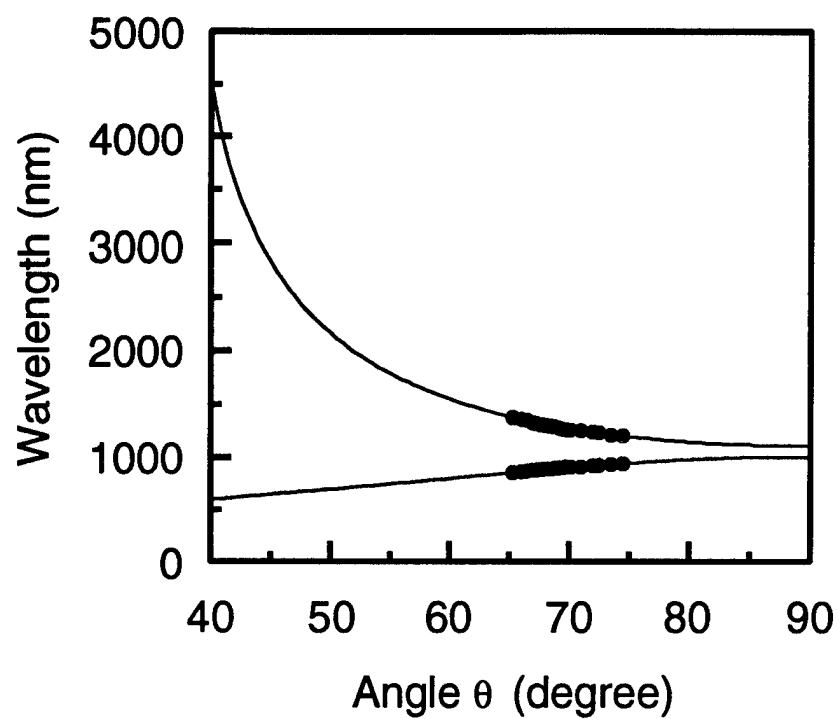


Figure 46: Tuning curve for KTP OPO phase-matched in  $xz$ -plane for a 527 nm pump. Thick bars correspond to the experimental data points. Solid lines are calculated tuning curves.



## 6.4 High-Order Transverse Mode and Multiple wavelength Oscillation

High-order transverse modes have been observed in an OPO by Mak *et al.*[19]. In OPOs there are several parameters which can affect the transverse mode of the signal, such as the spatial profile of the pump beam, the alignment of the cavity mirrors, the focal point of the pump beam, the position of the crystal inside the cavity, and the confocal parameters of the pump and signal beams. The spatial profile of the pump beam directly affects the spatial profile of the gain distribution. The alignment of the cavity mirrors determines the spatial mode of the signal and thus determines the coupling between the pump and signal beams. The focal point of the pump beam, the position of the crystal, and the confocal parameters of pump and signal beams also affect the coupling between the pump and signal.

In our OPO, high-order Cartesian transverse modes were also observed occasionally. The high-order transverse mode in our OPO is partially caused by the slightly elliptical profile of the pump beam and the astigmatism introduced by the folded ring cavity. The elliptical pump beam profile was caused by the walk-off of the 527 nm beam in the SHG KTP crystal. For example, Figure 47 shows the signal spectrums of  $TEM_{00}$  and  $TEM_{11}$  modes of the OPO output. The  $TEM_{11}$  mode was obtained intentionally by changing the angular alignment of the cavity mirrors. It is clear that the center wavelength is identical in these two cases. The calculated wavelength separation between  $TEM_{00}$  mode and  $TEM_{11}$  mode is 0.00037 nm, which is far smaller than the resolution of the monochromator used in the experiment. However, the FWHM spectral width becomes larger in the

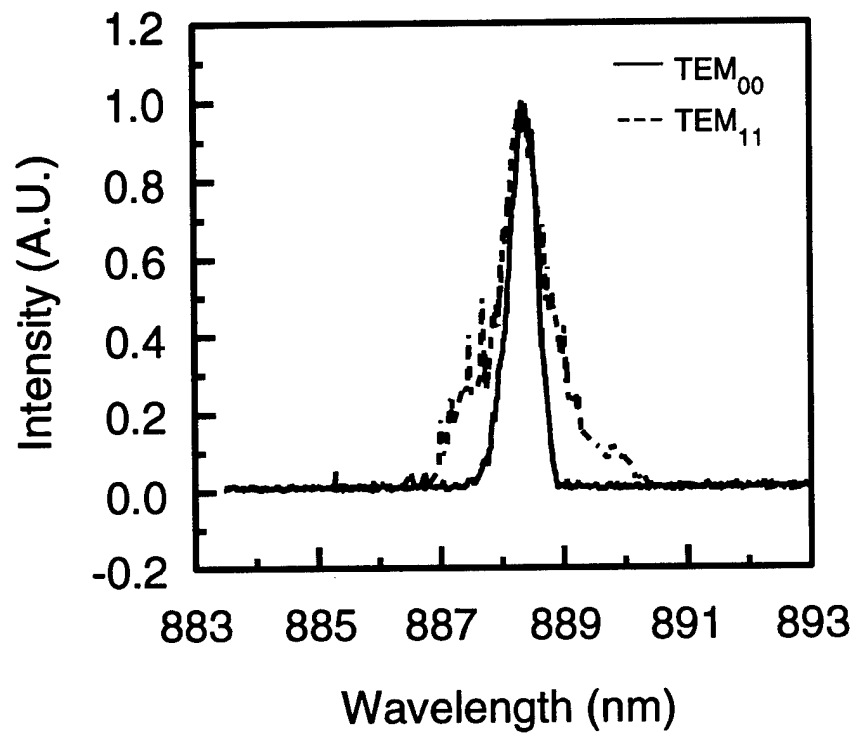


Figure 47: Spectra of the signal pulses with different transverse modes. The solid line represents the spectrum of a  $TEM_{00}$  mode and the dashed line corresponds to the spectrum of a  $TEM_{11}$  mode.

TEM<sub>11</sub> mode case, which is not expected in the normal laser system. The high-order transverse mode can be suppressed by inserting an aperture inside the cavity, but with up to 40 % decrease of the output power. However, the aperture was needed only when the high-order transverse mode was intentionally generated.

In conventional lasers, the lasing wavelength is determined by the energy separation between the lasing levels, which does not depend on the cavity alignment. However, the output wavelength of OPO is determined by the phase matching condition, which is dependent on the spatial arrangement of the pump beam, cavity mode, and angle of the crystal.

For instance, we found that under certain conditions the spectral width can be very broad while the spatial profile of the signal beam still maintains the circular shape of the TEM<sub>00</sub> mode. Figures 48(a), (c), and (e) show three different spectra of the signal under three different angular alignment conditions of the cavity mirrors at the same pumping level without tuning the crystal angle. Figures 48(b), (d), and (f) show the corresponding idler spectra. In Fig. ref:ktpmulti(a), two wavelength peaks were observed and the separation between these two signal peaks is about 2.5 nm which is much larger than the separation between the frequencies of different transverse modes. The difference between the phase-matching angles of these two peak wavelengths is 0.2 degree, or 5 mrad. This shows that two different crystal signal wavelengths oscillate simultaneously. The coexistence of two different signal wavelengths, and corresponding two different idler wavelengths, indicates that both satisfy the phase-matching condition inside the OPO. This is possible because of the large phase-matching bandwidth in our case. The slightly elliptical pump beam profile and the short effective interaction length are also

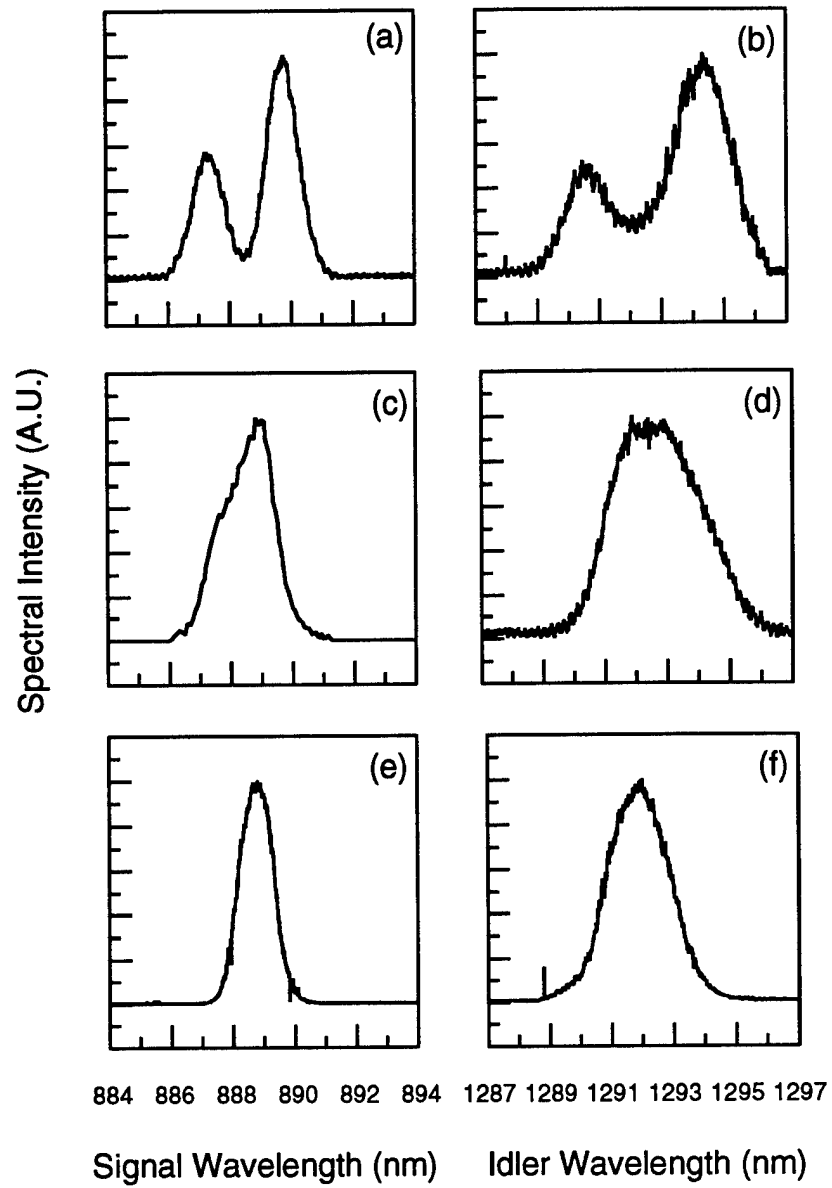


Figure 48: Spectra of the signal and idler pulses under different conditions of multiple-wavelength oscillation.

the possible reasons leading to the multiple-wavelength oscillation under specific alignment conditions.

In Fig. 48(c), the separation between the wavelengths becomes smaller such that it is hard to resolve the peak wavelengths. In Fig. 48(e), the spectrum becomes symmetrical and the FWHM spectral width is about 2 times the value of the  $TEM_{00}$  single wavelength case. No change of the pulsewidth was observed in all three cases.

The output power under the condition of multiple-wavelength oscillation is slightly higher than that of the single-wavelength  $TEM_{00}$  mode. The output power also becomes less stable in this case, which indicates the possibility of competition between different oscillating wavelengths. Figure 49 shows the signal output power versus the cavity detuning when the OPO was operated in the condition of Fig. 48(e). Clearly there are three peaks of the signal power in this detuning curve, which is the convolution of different single-wavelength detuning curves. The FWHM detuning range is about  $30\ \mu\text{m}$  which is about 3.4 times larger than that of the single-wavelength  $TEM_{00}$  mode case. Therefore, special care has to be taken when aligning the OPO cavity in order to avoid the multiple wavelength oscillation if narrow bandwidth is needed for the application.

## 6.5 Discussions and Summary

The threshold of an OPO is determined by setting the small signal gain equal to the total cavity loss. Therefore, the spatial and temporal effects which affect the small signal gain of the nonlinear medium are the limiting factors of the efficiency

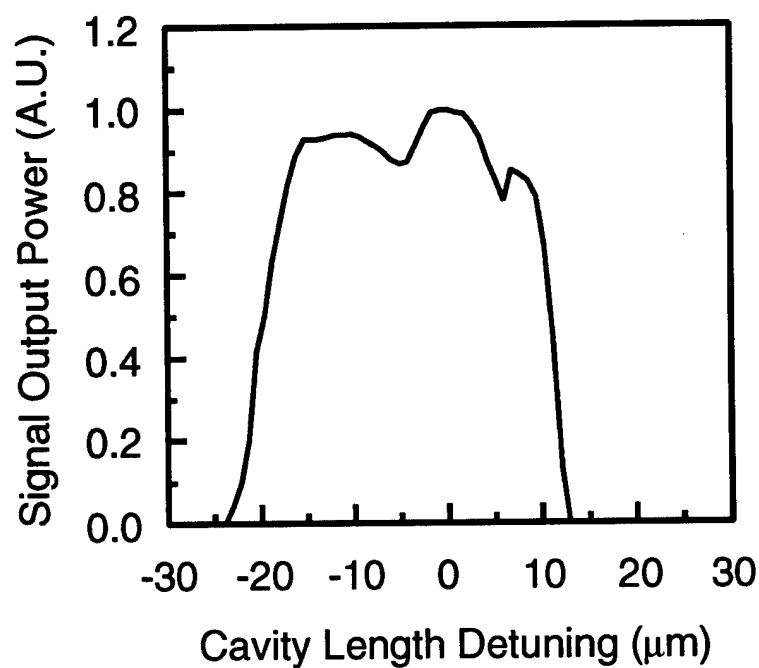


Figure 49: Signal output power as a function of cavity-length detuning under the condition of Fig. 4.10(e) and (f).

of the parametric interaction.

The spatial beam walk-off angle is calculated to be 36 mrad at the center of the spectral tuning range where  $\lambda_s = 890$  nm and  $\lambda_i = 1291$  nm. The spatial aperture length  $l_{sw}$ [69] is calculated to be 0.68 mm for a pump Gaussian beam waist of 20  $\mu$ m. The temporal aperture length  $l_{tw}$ [69] in our case is calculated to be 10.7 mm for the 4.5 ps pump pulsewidth. The net walk-off length  $l_w$  with compounded spatial and temporal walk-off effect is 0.68 mm. It is clear that the net walk-off length is dominated by the spatial walk-off effect. According to recent theoretical analysis[69], the optimal crystal length  $l_c$  is  $3l_w$  which is 2.04 mm in our case. Obviously, the spatial walk-off is the major limitation upon our OPO efficiency due to the high birefringence with the phase-matching in the  $xz$ -plane and the temporal walk-off is not important in our case.

The temporal pulse walk-off between the pump and signal pulses and that between the pump and idler pulses calculated from the center of the crystal assuming a useful interaction length of 2.04 mm are 0.27 ps and 0.99 ps, respectively. Since only the walk-off between the pump and the signal has the first order effect on the performance of the OPO[5], the temporal pulse walk-off is not the limiting factor for our OPO with the 4.5 ps pump pulses. The analysis above indicates that the 5 mm crystal is too long for our current OPO design. One way to fully utilize the 5 mm crystal is to enlarge the pump beam spot size and increase the signal spot size in the cavity. Since curved mirrors with larger radius of curvature are not available to us at this point, no attempt has been made to study the spatial walk-off limitation.

Other spatial and temporal effects are not the limiting factors in our case.

For example, the phase matching bandwidth  $\delta\lambda$  is calculated to be 3.67 nm at the signal wavelength of 890 nm assuming 2.04 mm crystal length, which is equal to the spectral width of a 0.31 ps transform-limited pulse assuming a Gaussian pulse shape. Therefore, the phase-matching bandwidth of this crystal is wide enough for the signal pulses. The pulse broadening effect due to group velocity dispersion is not significant until the pump pulsewidth becomes less than 100 fs for the parameters used in our study.

According to recent simulation[69], the threshold of this OPO will further decrease if we compress the pump pulse down to 500 fs. Although the temporal aperture length  $l_{tw}$  is decreased by a factor of 9 when the pump pulses are compressed to 500 fs,  $l_{tw}$  is still longer than the spatial aperture length  $l_{sw}$ . Therefore, the parametric process is still limited by the spatial walk-off. In the specific example of  $\lambda_s = 890$  nm and  $\lambda_i = 1291$  nm, the net walk-off length  $l_w$  is only slightly reduced from 0.68 mm for 4.5 ps pulses to 0.59 mm for 500 fs pulses while the peak power is increased by ninefold for the same average power. As a result, the threshold of the OPO is reduced by 6.4 times[69]. With new crystals and other sets of mirrors, generation of picosecond and femtosecond optical pulses with a wide tuning range should be achievable.

In summary, we demonstrated a KTP based synchronously pumped singly resonant OPO pumped with a frequency-doubled additive-pulse mode-locked Nd:YLF laser. Signal pulses 3.2 ps in duration, tunable from 851 to 938 nm, and idler pulses 2.4 ps in duration, tunable from 1200 to 1381 nm were obtained by angle tuning. The experimental results were compared with previous theoretical analyses. High-order transverse modes and multiple-wavelength oscillation in the OPO



were observed and discussed.

## 7.0 Parametric Generation of Femtosecond Optical Pulses

### 7.1 Introduction

Femtosecond optical pulses provide the ability to study ultrafast dynamic processes. However, the pulsewidth directly generated by a CW mode-locked laser is limited by the bandwidth of the gain medium. For Nd:YLF laser, the lower limit of the pulsewidth is 0.9 ps[70, 71]. Therefore, in order to generate femtosecond pulses from Nd:YLF laser, pulse compression technique is needed. The concept of optical pulse compression originated from chirp radar[72]. Due to the combined effects of self-phase modulation and group velocity dispersion in the fiber, the optical pulses are broadened spectrally and chirped temporally after propagation in the optical fiber. These pulses can be temporally compressed by use of the dispersive elements such as grating pairs[73] or prism pairs[74].

In this section, two ways of generating femtosecond optical pulses at 527 nm are presented. The first approach is by second harmonic generation of the compressed femtosecond optical pulses at 1053 nm. The second approach is to compress the picosecond optical pulses at 527 nm to subpicosecond regime. The experimental results and practical limitations of both approaches are discussed. The results of the threshold study of an optical parametric oscillator using femtosecond pulses are also included.

## 7.2 Second Harmonic Generation of Femtosecond Optical Pulses at 1053nm

The experimental setup for compression of APM Nd:YLF laser pulses is similar to that in Chee's experiments[75]. The input to the pulse compressor was the optical pulse train of 6.4 ps pulsewidth at 9.5 W of average power with a repetition rate of 76 MHz, which was obtained from the APM Nd:YLF laser. The fiber used in this experiment was a highly-birefringent single-mode fiber (YORK HB 1100/1). The index difference  $\Delta n$  between core and cladding was characterized to be 0.006, the birefringent index difference  $\delta n$  between two axes of the fiber was  $2.4 \times 10^{-4}$ , and the average core diameter was 6  $\mu\text{m}$ . The length of the fiber was 85 cm. Although the fiber tips were carefully polished to have an angle, an optical isolator inserted between two halfwave plates was used before the input end of the fiber to eliminate the optical feedback from the fiber end surface. A lens with a focal length of 30 cm and a 10 $\times$  microscope objective lens (F-L10B) were used to couple light into the fiber. Typical coupling efficiency into the fiber was 40%. The average power coupled into the fiber was about 3.8 W. Less than 10% of the power was converted to Raman wavelength. The input polarization was aligned along the fast axis of the fiber to maintain linearly polarized output. The output from the fiber was collimated by a 20 $\times$  microscope objective lens. The spectral widths of the optical pulses were measured by a monochromator with a resolution of 0.06 nm.

Figure 50 shows the broadened spectrum of the pulse emerging from the fiber. The FWHM spectral width of the output pulse was 8 nm. The spectral width of the input pulse was 0.3 nm. The substantially broadened spectrum was caused by the self-phase modulation of the pulse in the fiber. The sharp peak in the center of the

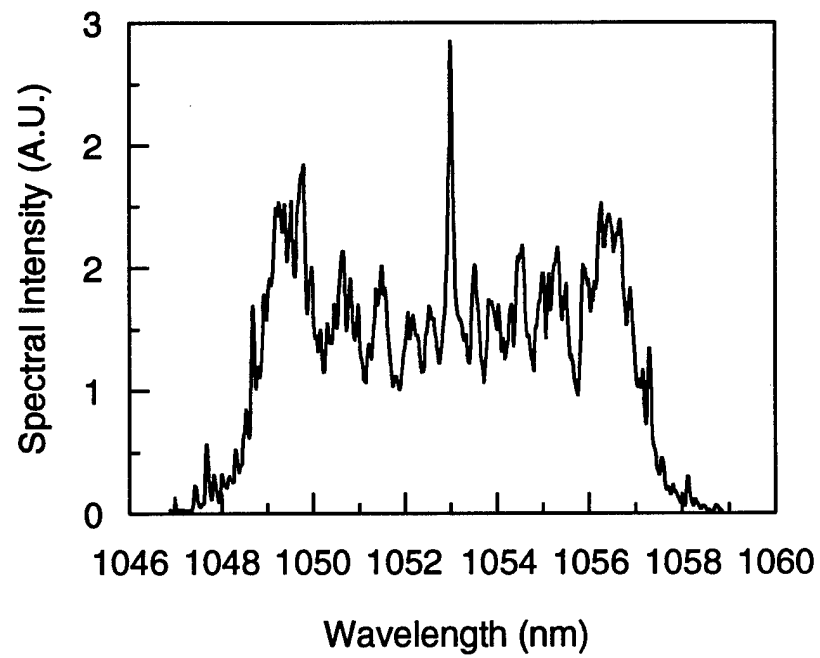


Figure 50: Broadened spectrum of the pulse emerging from the 85 cm length of fiber.

spectrum is the cw power of the Nd:YLF laser, which is due to incomplete mode-locking of the APM process. These spectrally broadened pulses were temporally compressed by a dispersive delay line which is a combination of a grating and a right-angle prism, as is shown in Fig. 51. The grating had a groove frequency of 1150 lines/mm (American Holographic AH-PC-1500-P1). The angles of incidence and diffraction  $\gamma$  and  $\gamma'$  were approximately 40 and 30 degrees, respectively. The diffracted beam was reflected by a right-angle prism to the grating with a lateral shift. The right-angle prism was mounted on a translation stage in order to adjust the separation between the grating and prism. The pulsewidth of the compressed pulse was monitored with an autocorrelator using noncollinear second-harmonic generation with a resolution of 50 fs.

Figure 52 shows the autocorrelation trace of the compressed pulse while the separation between the prism and the grating was 4.5 cm. The 690 fs FWHM of the autocorrelation trace corresponds to a pulsewidth of 450 fs with a time-bandwidth product of 1.07 assuming  $\text{sech}^2$  pulse shape. The diffraction efficiency of the grating was only 75% for p-polarization at 1053 nm wavelength because the grating was optimized for use at 1550 nm wavelength. With the reflection losses from the uncoated prism, the throughput efficiency was limited to  $\sim 40\%$  and only 1.4 W average power was available in the compressed pulses. Since the optical beam only passed through the grating twice, the astigmatism due to the spectral dispersion was not eliminated in this case. The spatial profile was a  $45^\circ$  tilted elliptical shape.

For second harmonic generation, the compressed 450 fs optical pulses at 1053 nm were focused into a KTP crystal using a lens with a 5-cm focal length. Due to

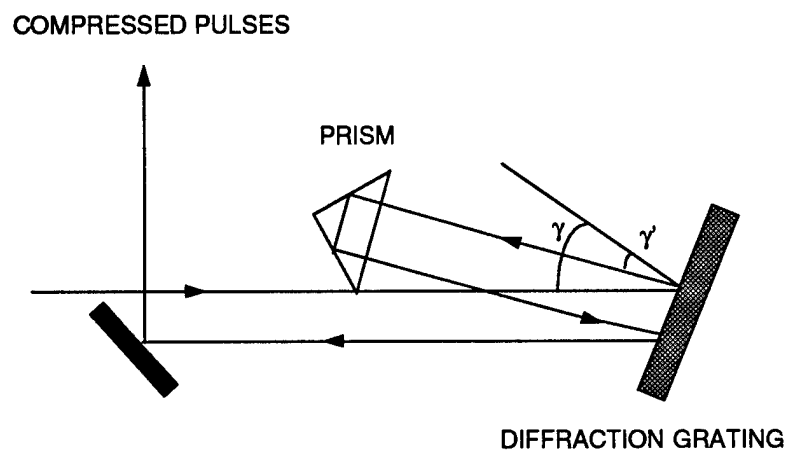


Figure 51: The arrangement of a grating-prism dispersive delay line

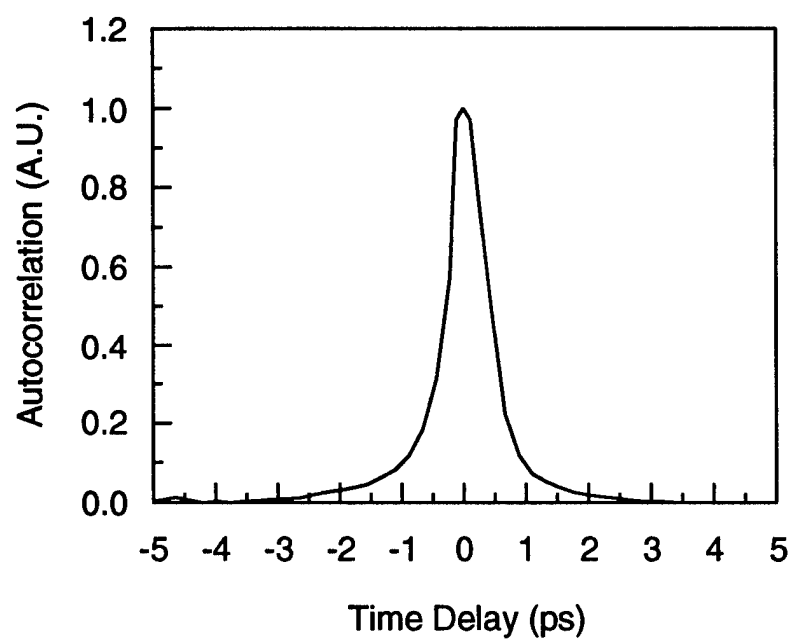


Figure 52: Autocorrelation trace of the compressed 1053 nm pulse

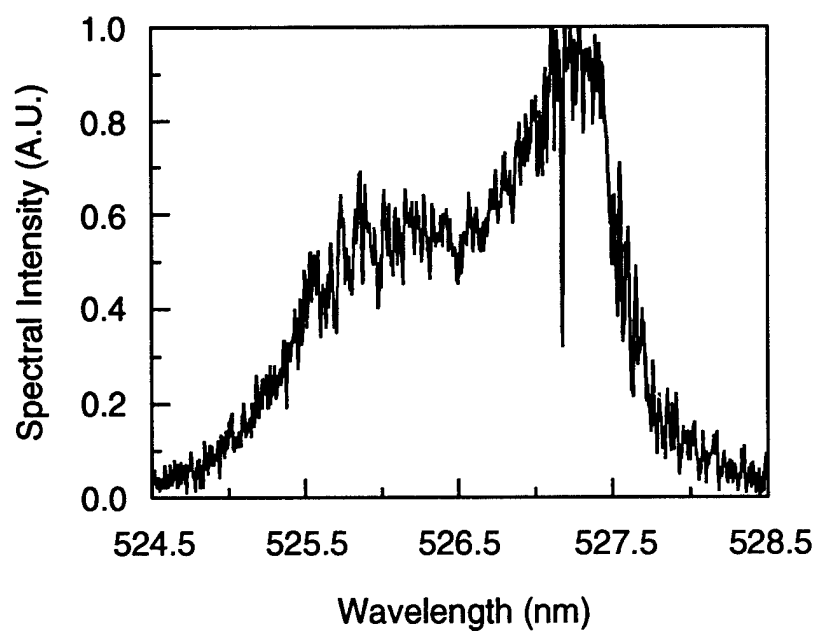


Figure 53: The spectrum of the 527 nm pulses generated by second harmonic generation of 450 fs pulses at 1053 nm



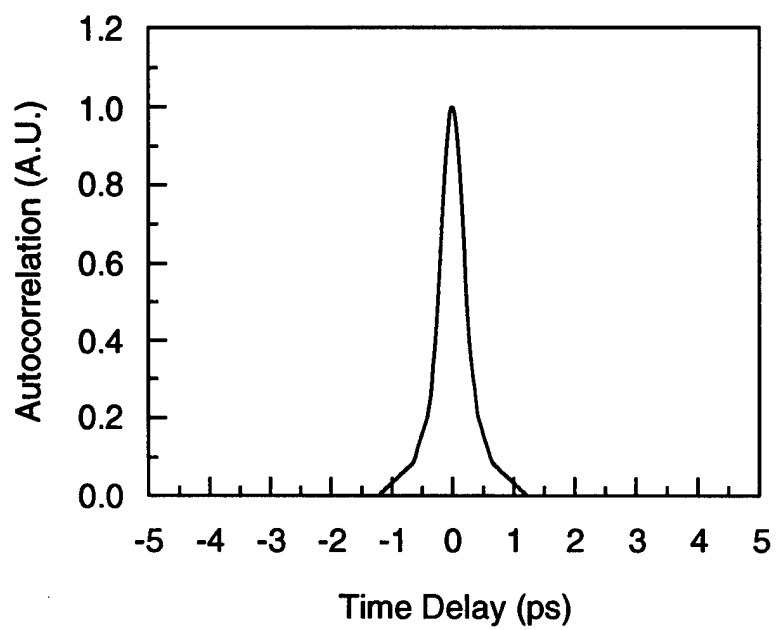


Figure 54: The autocorrelation trace of the 527 nm pulses generated by second harmonic generation of 450 fs pulses at 1053 nm

the losses of all the mirrors and the lens, only 1 W of average power was sent into the crystal. The dimension of the KTP crystal is  $3 \times 3 \times 5$  mm. Figure 53 shows the optical spectrum of the 527 nm pulses generated by the second harmonic generation of the 450 fs pulses at 1053 nm. The FWHM spectral width was 2 nm. The cw background observed in the spectrum of 1053 nm APM Nd:YLF pulses was eliminated in the SHG spectrum. Figure 54 shows the autocorrelation trace of 527 nm pulses. The 520 fs FWHM of the autocorrelation trace corresponds to a pulsewidth of 340 fs with a time-bandwidth product of 0.73 assuming  $\text{sech}^2$  pulse shape. However, the average power of the 527 nm pulses was only 150 mW and the conversion efficiency was only 15%. This low conversion efficiency was mainly due to the astigmatism of the beam profile. The highly chirped 1053 nm pulses may also limit the conversion efficiency.

### 7.3 Pulse Compression of Picosecond Pulse at 527 nm

The frequency-doubled 4.5 ps pulse at 4 W of average power was obtained from the second harmonic generation of the APM Nd:YLF pulses. These frequency-doubled pulses were coupled into a slightly multi-mode fiber using a  $20\times$  microscope objective lens. The core diameter of the fiber is 4  $\mu\text{m}$ . No optical isolator was needed since the SHG crystal was a very good optical isolator. Typical coupling efficiency was 35%. Up to 1.4 W of average power was coupled into the fiber. The tips of the fiber were cleaved cleanly without polishing the surface. The output beam was collimated by another  $20\times$  microscope objective lens.

A 2 m long fiber was first used in the experiment. However, almost 35% of the power coupled into the fiber was converted to Raman Stokes. Figure 55 shows the

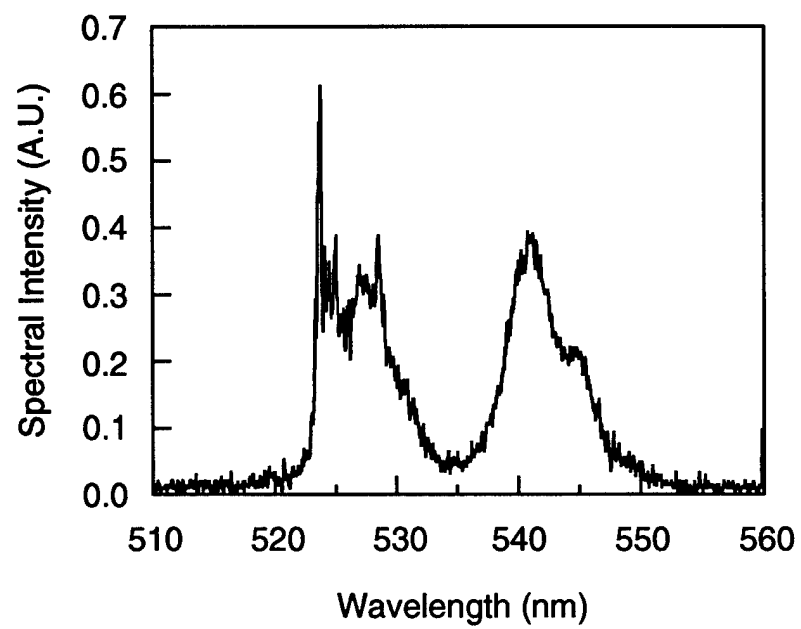


Figure 55: The spectrum of the output pulse emerging from the 2 m length of fiber.

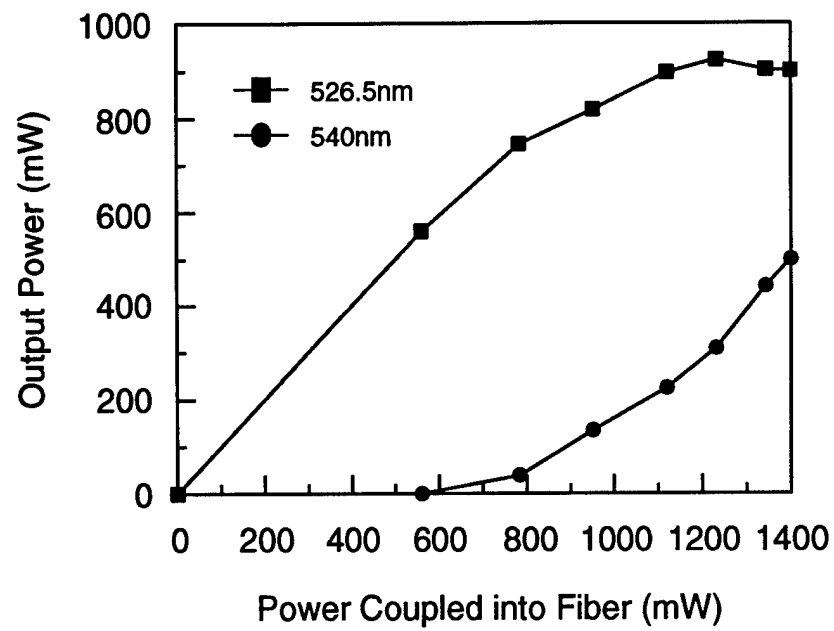


Figure 56: Average output power of the 527 nm and the first Raman Stokes emerging from a 2 m long fiber as a function of the average power coupled into the fiber

optical spectrum of the output from a 2 m long fiber. It is interesting to notice that the spectrum of Raman Stokes reflects the Raman gain profile of the fiber and the spectrum between the 527 nm pump and 540 nm Raman Stokes is possibly caused by four wave mixing in the fiber. The shape of spectrum indicates that the pulse spectrum was substantially broadened due to self-phase modulation before the Raman effect started. Figure 56 shows the average output power of 527 nm and 540 nm Raman Stokes emerging from a 2 m long fiber as a function of the average power coupled into the fiber. The Raman threshold was at about an average power level of 560 mW coupled into the fiber and the output 527 nm power was clamped to a power level of 900 mW.

In order to reduce the Raman conversion, a 65 cm long fiber was then used in the experiment. The Raman threshold was increased to about 1 W average power coupled into the fiber. About 220 mW was converted into Raman Stokes. Figure 57 shows the optical spectrum of the output pulse emerging from the 65 cm long fiber. The FWHM spectral width of the output pulse was 4.5 nm. Due to the lack of available grating at 527 nm wavelength range, a prism pair was used as the dispersive delay line. Figure 58 shows the arrangement of the prism pair dispersive delay line. The prism used in the experiment was the Brewster's angle dispersing prism made by Optical For Research(ABS-15). The light was retroreflected through the prism pair. The Raman Stokes component was blocked from reflecting back. The separation between the apex of the prisms was adjusted to achieve pulse compression.

Figure 59 shows the autocorrelation trace of the 527 nm compressed pulses while the separation between prism apex was 75 cm. The 690 fs FWHM of the

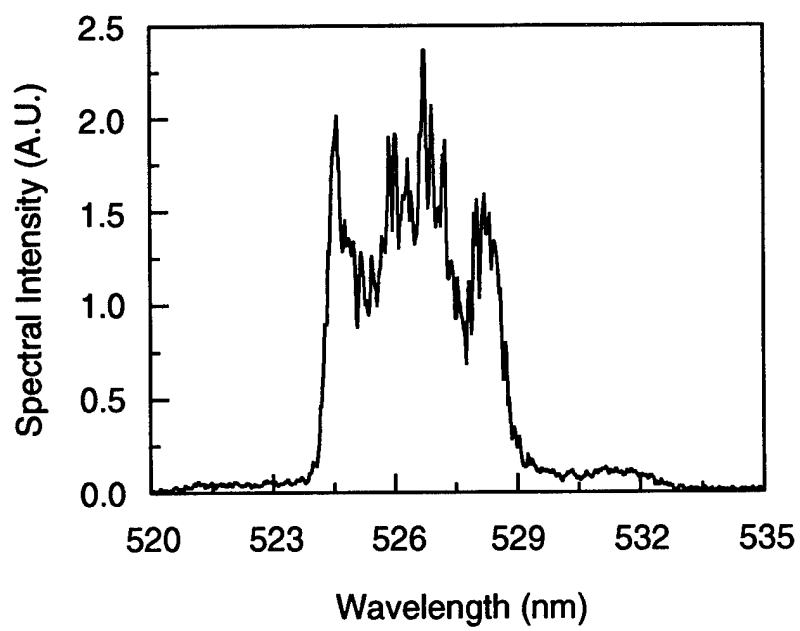


Figure 57: The spectrum of the output pulse emerging from a 65 cm long fiber.

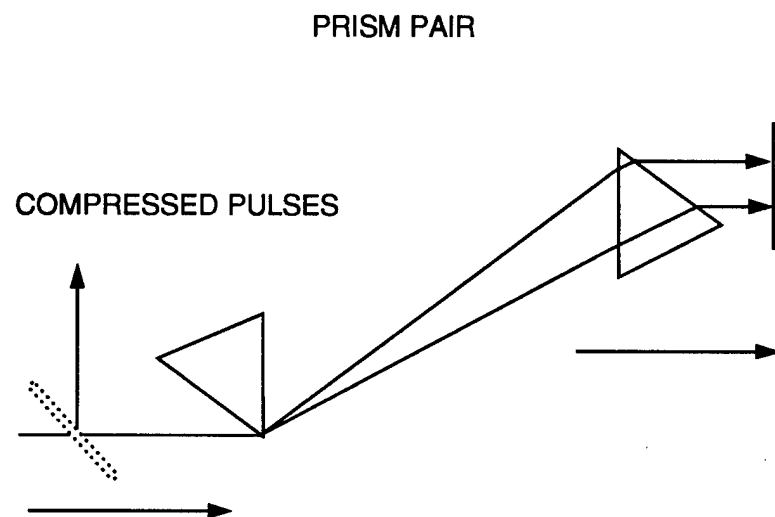


Figure 58: The configuration of the prism pair dispersive delay line

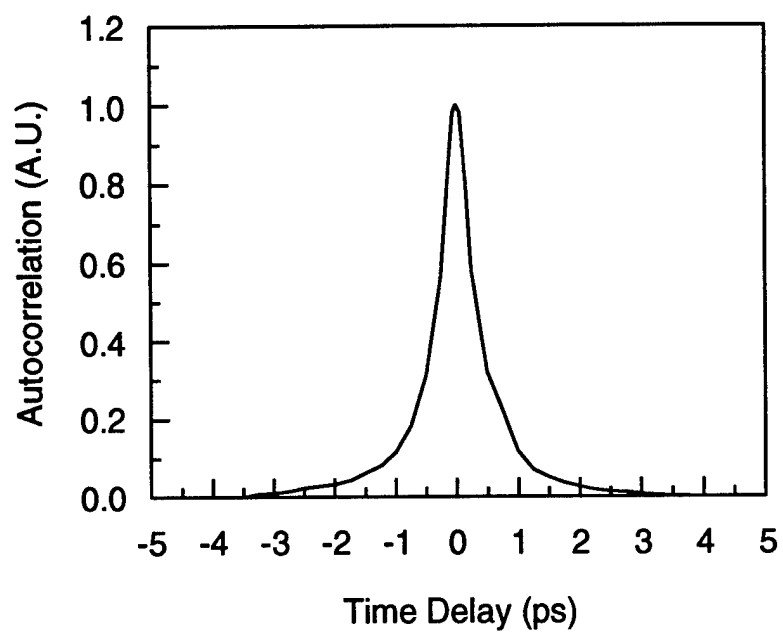


Figure 59: The autocorrelation trace of the 527 nm pulses exiting the fiber prism-pair pulse compressor



autocorrelation trace corresponds to a pulsewidth of 450 fs with a time-bandwidth product of 2.17 assuming  $\text{sech}^2$  pulse shape. This corresponds to a compression factor of 10 and the large time-bandwidth product indicates the pulse was highly chirped. The total available output power after the pulse compressor was 500 mW due to the losses of all the optical components and the depolarization in the fiber. The spatial profile of the output beam was elliptical with an aspect ratio of 1:3.

## 7.4 Threshold Study of Femtosecond OPO

As described in section 3.2.3, the power threshold of the KTP OPO will be reduced to about 140 mW if the OPO is pumped by 500 fs pulses. The 450 fs pulses at 527 nm described in section 7.3 were used as the pump pulses in the threshold study of the femtosecond OPO. The experimental setup was the same as that described in section 3.2.3.

To avoid the damage of the second-harmonic-generating KTP crystal and the tips of the fiber used in pulse compression, the output of the APM Nd:YLF laser was chopped with a 12:1 duty cycle. Again, the parametric fluorescence was detected to help the alignment of the OPO cavity. Due to the low average pump power available, the single pass fluorescence signal leaking from the output coupler was only 0.03 mV while the noise level was 0.01 mV. When the feedback path inside the cavity was unblocked, the fluorescence signal increased to 0.13 mV. However, no oscillation was achieved while the output coupler mirror was moved from  $-1.5$  to  $1.5$  cm with respect to the zero detuning point of the picosecond OPO.

The actual average power sent into the OPO KTP crystal was about 350 mW. According to the simulation, this amount of pump power should be large enough

to overcome the power threshold of the OPO. However, two major reasons may have some serious effect upon the threshold of the OPO. First, the 527 nm pump pulses were highly chirped, which may decrease the efficiency of parametric generation. Second, the spatial profile of the 527 nm pump pulses were elliptical, which decreased the conversion efficiency due to the poor spatial overlapping with the cavity mode.

In order to improve the quality of the pump pulses, several approaches can be used. First, a polarization-preserving fiber can be used to increase the throughput efficiency of the pulse compressor. Second, a grating pair designed for 527 nm can be used to obtain a better spatial profile. Third, the core diameter and the length of the fiber used in the pulse compressor can be optimized in order to achieve linear chirping across the pulse emerging from the fiber, which may lead to a time-bandwidth product close to transform limit.

## 8.0 Conclusions

### 8.1 Summary

A theoretical model for calculating the effective gain of parametric generation and amplification of ultrashort optical pulses has been developed and presented in this project. This model takes into account both spatial and temporal effects, including spatial beam broadening, temporal pulse broadening, spatial walk-off of the pulse beams, and temporal walk-off of the parametrically interacting pulses. A closed-form analytical formulation is obtained for the effective interaction length, the parametric efficiency coefficient, and the effective gain of the parametric process.

From the numerical examples given above and from maximizing the value of  $b$  with the dependence of  $l_{\text{eff}}$  on  $w_{30}$  and  $\Delta t_{30}$  included, we come to following conclusions:

1. When no significant temporal pulse broadening in the crystal is expected, the optimal crystal length is  $l_c = l_{\text{opt}} = 3l_w$ . This crystal length depends on the pulsewidth and the focused beam waist.
  - (a) For a given pump pulsewidth, the required crystal length can be reduced by focusing the beams tighter to reduce  $l_w$  through the reduction of  $l_{sw}$ . This can be done until the effect of spatial beam broadening becomes important, which then may or may not reduce the efficiency, depending on the specific parameters characterizing the situation. In any event, the beam should be focused to the extent that  $l_{sw} < l_{tw}$ , if possible.

Beyond this, the efficiency increases from further focusing the beams, only at a slower rate, and quickly saturates.

- (b) If the pump pulsewidth can be varied, reducing the pulsewidth can increase the parametric efficiency if  $l_{sw} < l_{tw}$ . The maximum parametric efficiency occurs when  $l_{tw} = l_{sw}$ . Beyond this, further reducing the pulsewidth without reducing the beam waist size actually hurts the parametric efficiency.
  - (c) For short pulses, the optimal condition is  $l_{sw} = l_{tw}$ . For long pulses, one can do slightly better by having  $l_{sw} < l_{tw}$ . The combination of  $w_{30}$  and  $\Delta t_{30}$  for  $l_{sw} = l_{tw}$  can be found from Fig. 9.
2. For extremely short pulses, temporal pulse broadening in the crystal can be important. In this case, the optimal crystal length is determined based on the acceptable broadening in the pulses rather than on the consideration of the maximum parametric efficiency alone. Generally speaking, to avoid significant pulse broadening, the crystal length chosen is smaller than that of the maximum parametric efficiency. For such short pulses and short crystals, the parametric efficiency can increase quadratically with the decrease of the beam waist size. Therefore, the beams should be focused as tight as possible.
  3. As far as the noncollinear phase matching geometry is concerned, theoretical formulations presented in Section 2.0 still apply. Different phase-matching geometries affect the values of  $l_{sc}$  and  $l_{sw}$  through changing values of  $\alpha_1$ ,  $\alpha_2$ , and  $\alpha_3$ . As we have mentioned in the previous section, the effects of non-collinear phase matching geometry is simple and elegant. First, to increase

the parametric efficiency, the value of  $l_{sw}$  needs to be maximized. Second, the more a parametric process is dominated by the spatial effects, the more effective the use of noncollinear phase-matching geometry is in improving its efficiency.

We have assumed that the pulses are not chirped at the input surface of the nonlinear crystal throughout this paper. In real experimental situations, the pulses are often chirped. This does not pose a problem to our theoretical framework. Nor does it invalidate our general conclusions. However, it does change the quantitative numerical results. Extension of our formulation to chirped pulses is straightforward, but mathematically tedious. It is thus not done in this project. It can be done, if necessary, by replacing  $\Delta t_{j0}^2$  in Eq. 12 with  $\Delta t_{j0}^2/(1 + iC_{j0})$  where  $C_{j0}$  is a constant representing the initial chirping in pulse  $j$  at the input, and then carrying out the rest of the theoretical calculations outlined in Section 2.0.

In the numerical examples presented in Section 3.0, we have assumed for simplicity that all three parametric beams are focused to the same beam waist size and all three pulses have the same pulsewidth at the input. Therefore, all the quantitative results demonstrated there are subject to this condition. Again, in real experimental situations, this is rarely the case, particularly when there is a large difference between the signal and idler wavelengths. However, this does not invalidate our general conclusions either. In reality, although the beam waist sizes are often different, they are kept very close to one another for maximum efficiency. Similarly, the signal and idler pulsewidths typically vary within  $\pm 50\%$  of the pump pulsewidth, as has been predicted by previous theoretical work and verified by all

the reported experimental work. In applying our theory to any experimental results of known beam waist ratios and pulsewidth ratios, it is only necessary to use the experimentally known values for these ratios in the evaluation of relevant parameters.

In this research project, parametric generation of wavelength-tunable ultrashort optical pulses was also demonstrated using an additive-pulse mode-locked Nd:YLF laser. A KTP-based picosecond optical parametric oscillator synchronously pumped by frequency-doubled APM Nd:YLF laser pulses was demonstrated. Above the threshold of 900 mW average pump power, continuous tuning was demonstrated from 851 to 938 nm in the signal branch and from 1200 to 1381 nm in the idler branch. At three times the threshold, 3.2 ps signal pulses with an average power of 83 mW and 2.4 ps pulses with an average power of 280 mW were obtained. Characteristics of this OPO have been studied in detail. The significance of the OPO is that it is the first demonstration of OPO synchronously pumped by a flashlamp pumped APM Nd:YLF laser and it offers a possibility to produce wavelength-tunable pulses which cover the 600 to 4500 nm transmission window of KTP by simply using one OPO without intracavity doubling.

Femtosecond pulse generation from Nd:YLF laser was presented. Two different approaches to generate femtosecond frequency-doubled Nd:YLF laser pulses were compared. The efforts to produce femtosecond OPO and to generate wavelength-tunable optical pulses at the wavelength range of 10-11  $\mu\text{m}$  were also included.

## 8.2 Future Research

The method we have presented for analyzing the OPO systems is very powerful and versatile. Since it accounts for both the spatial and temporal effects, one can approximate various experimental parameters to a substantial accuracy. Like any other theoretical research, this method is not yet fully explored and can be used in various other applications. In this project, only one kind of nonlinear crystal, KTP, was used to demonstrate the validity of our method. Other important nonlinear crystals, such as BBO and LBO for efficient parametric generation from ultraviolet to near-infrared and AgGaS<sub>2</sub> and AgGaSe<sub>2</sub> for efficient parametric generation from near- to mid-infrared, can also be characterized by employing our method. We can also extend this theory to the most fundamental phenomenon of nonlinear optics: second harmonic generation (SHG). SHG of ultrashort pulses can be modeled using this method with some modifications to the theory and similar simulations can be performed to better understand the process. Many other nonlinear crystals used for SHG, of course, can again be considered using this theory.

Theoretical models without the verification by experimental results are not practical. Therefore, many experiments can be performed and their parameters compared with the theoretical values for the experimental parameters. Given the many simplifying assumptions made in obtaining the numerical results presented in this report, these results, when used to predict the threshold of synchronously pumped OPOs in our laboratory, are found to be in very good agreement with experimental results [76].

The cw mode-locked Nd:YLF laser in our laboratory can generate high-peak power ultrashort pulses with pulsewidth from 30 ps to a few hundred femtosecond

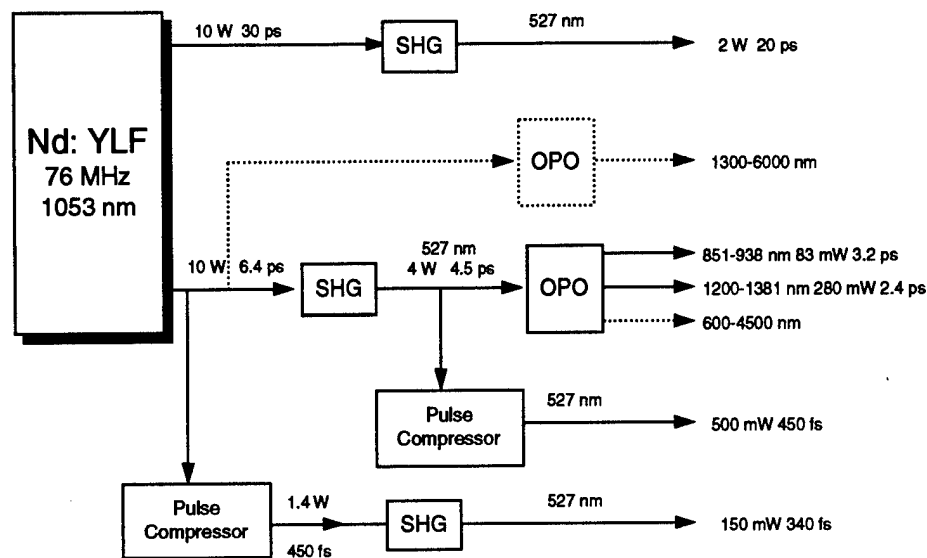


Figure 60: The Schematic diagram of the current available laser pulses(solid line) and the future systems(dotted line).

at two different wavelengths. The 527 nm frequency-doubled pulses can be used as the pump laser of the visible to near-infrared range OPO. The 1053 nm pulses can be used as the pump laser of the near- to mid-infrared range OPO. With different crystals and different sets of optics, ultrashort pulses tunable from visible to mid-infrared could be generated by one pump laser system. Figure 60 summarizes the currently available pulses from our system and the future possible systems that could be developed.

A picosecond OPO is relatively difficult to build due to the high average power



threshold in comparison with a femtosecond OPO. However, generation of femtosecond pump pulses from a Nd:YLF laser with good pulse and beam quality and high average power is not trivial. Many parameters of the pulse compressor have to be fine-tuned in order to improve the throughput efficiency and pulse quality.

In order to extend the wavelength of the OPO into mid-infrared range, the absorption of the crystals must be overcome first. Since no theoretical study has been done to investigate the influence of the crystal absorption upon the efficiency of the parametric generation process, it would be a very important work to find out the effect of crystal absorption upon the threshold of OPO.

Optical parametric oscillators are powerful research tools and have been increasing their number of applications at a fast rate. Several commercialized products, for example devices capable of tuning from the ultraviolet to the near-infrared region, have already been on the market. Possible applications using OPOs in myriad disciplines are endless. As we near the end of the 20th century, we expect to find more applications of laser and nonlinear optical devices in the near future. It is hoped that the results in this report will play an important role in further research and development of OPOs.

## References

- [1] A. Laubereau, *Ultrashort Laser Pulses and Applications*. Springer-Verlag, New York, 1988.
- [2] K.L. Vodopyanov, "Parametric generation of tunable infrared radiation in  $\text{ZnGeP}_2$  and GaSe pumped at  $3\text{ }\mu\text{m}$ .", *Journal of Optical Society of America B*, 10, 1723–1729, 1993.
- [3] A.G. Yodh, H.W.K. Tom, G.D. Aumiller, and R.S. Miranda, "Generation of tunable mid-infrared picosecond pulses at 76 MHz.", *Journal of Optical Society of America B*, 8, 1663–1667, 1991.
- [4] E. C. Cheung and J. M. Liu, "Theory of a synchronously pumped optical parametric oscillator in steady-state operation", *Journal of Optical Society of America B*, 7(8), 1385–1401, August 1990.
- [5] E. C. Cheung and J. M. Liu, "Efficient generation of ultrashort, wavelength-tunable infrared pulses", *Journal of Optical Society of America B*, 8, 1491–1506, 1991.
- [6] A. Piskarskas, V. Smil'gyavichyus, and A. Umbrasas, "Continuous Parametric Generation of Picosecond Light Pulses", *Soviet Journal of Quantum Electronics*, 18(2), 155–156, February 1988.
- [7] M. Ebrahimzadeh, G. P. A. Malcolm, and A. I. Ferguson, "Continuous-wave mode-locked optical parametric oscillator synchronously pumped by a diode-laser-pumped solid-state laser", *Optics Letters*, 17(3), 183–185, February 1992.

- [8] M. J. McCarthy and D. C. Hanna, "Continuous-wave mode-locked singly resonant optical parametric oscillator synchronously pumped by a laser-diode-pumped Nd:YLF laser", *Optics Letters*, 17(6), 402-404, March 1992.
- [9] A. Nebel, C. Fallnich, R. Beigang, and R. Wallenstein, "Noncritically phase-matched continuous-wave mode-locked singly resonant optical parametric oscillator synchronously pumped by a Ti:sapphire laser", *Journal of Optical Society of America B*, 10(11), 2195-2200, November 1993.
- [10] Ch. Grässer, D. Wang, R. Beigang, and R. Wallenstein, "Singly resonant optical parametric oscillator of  $\text{KTiOPO}_4$  synchronously pumped by the radiation of a continuous-wave mode-locked Nd:YLF laser", *Journal of Optical Society of America B*, 10(11), 2218-2221, November 1993.
- [11] J. Chung and A. E. Siegman, "Singly resonant continuous-wave mode-locked  $\text{KTiOPO}_4$  optical parametric oscillator pumped by Nd:YAG laser", *Journal of Optical Society of America B*, 10(11), 2201-2210, November 1993.
- [12] G. J. Hall, M. Ebrahimzadeh, G. P. Malcolm, and A. I. Ferguson, "Synchronously pumped optical parametric oscillators using all-solid-state pump lasers", *Journal of Optical Society of America B*, 10(11), 2168-2179, November 1993.
- [13] S. D. Butterworth, M. J. McCarthy, and D. C. Hanna, "Widely tunable synchronously pumped optical parametric oscillator", *Optics Letters*, 18(17), 1429-1431, September 1993.

- [14] M. J. McCarthy and D. C. Hanna, "All-solid-state synchronously pumped optical parametric oscillator", *Journal of Optical Society of America B*, 10(11), 2180–2190, November 1993.
- [15] A. Robertson and A. J. Ferguson, "Synchronously pumped all-solid-state lithium triborate optical parametric oscillator in a ring configuration", *Optics Letters*, 19(2), 117–119, January 1994.
- [16] E. C. Cheung, K. Koch, and G. T. Moore, "Silver thiogallate, singly resonant optical parametric oscillator pumped by a continuous-wave mode-locked Nd:YAG laser", *Optics Letters*, 19(9), 631–633, May 1994.
- [17] D. C. Edelstein, E. S. Wachman, and C. L. Tang, "Broadly Tunable High Repetition Rate Femtosecond Optical Parametric Oscillator", *Applied Physics Letters*, 54(18), 1728–1730, May 1989.
- [18] E. S. Wachman, W. S. Pelouch, and C. L. Tang, "cw femtosecond pulses tunable in the near- and midinfrared", *Journal of Applied Physics*, 70(3), 1893–1895, August 1991.
- [19] G. Mak, Q. Fu, and H. M. van Driel, "Externally pumped high repetition rate femtosecond infrared optical parametric oscillator", *Applied Physics Letters*, 60(5), 542–544, February 1992.
- [20] Q. Fu, G. Mak, and H. M. van Driel, "High-power, 62-fs infrared optical parametric oscillator synchronously pumped by a 76-MHz Ti:sapphire laser", *Optics Letters*, 17(14), 1006–1008, July 1992.

- [21] W. S. Pelouch, P. E. Powers, and C. L. Tang, "Ti:sapphire-pumped, high-repetition-rate femtosecond optical parametric oscillator", *Optics Letters*, 17(15), 1070-1072, August 1992.
- [22] P. E. Powers, S. Ramakrishna, C. L. Tang, and L. K. Cheng, "Optical parametric oscillation with  $\text{KTiOAsO}_4$ ", *Optics Letters*, 18(14), 1171-1173, July 1993.
- [23] P. E. Powers, R. J. Ellingson, W. S. Pelouch, and C. L. Tang, "Recent advances of the Ti:sapphire-pumped high-repetition-rate femtosecond optical parametric oscillator", *Journal of Optical Society of America B*, 10(11), 2162-2167, November 1993.
- [24] J. M. Dudley, D. T. Reid, M. Ebrahimzadeh, and W. Sibbet, "Characteristics of a non-critically phase-matched Ti:sapphire pumped femtosecond optical parametric oscillator", *Optics Communications*, 104(4), 419-430, January 1994.
- [25] P. E. Powers, C. L. Tang, and L. K. Cheng, "High-repetition-rate femtosecond optical parametric oscillator based on  $\text{CsTiOAsO}_4$ ", *Optics Letters*, 19(1), 37-39, January 1994.
- [26] T. J. Driscoll, G. M. Gale, and F. Hache, "Ti:sapphire second-harmonic pumped visible range femtosecond optical parametric oscillator", *Optics Communications*, 110(5), 638-644, September 1994.

- [27] M. F. Becker, D. J. Kuizenga, D. W. Phillion, and A. E. Siegman, "Analytic Expressions for Ultrashort Pulse Generation in Mode-Locked Optical Parametric Oscillators", *Journal of Applied Physics*, 45(9), 3996–4005, September 1974.
- [28] G. D. Boyd and A. Ashkin, "Theory of parametric oscillator threshold with single-mode optical masers and observation of amplification in  $\text{LiNbO}_3$ ", *Physical Review*, 146(1), 187–198, June 1966.
- [29] G. D. Boyd and D. A. Kleinman, "Parametric interaction of focused Gaussian light beams", *Journal of Applied Physics*, 39(8), 3597–3639, July 1968.
- [30] R. Asby, "Optical-mode interaction in nonlinear media", *Physical Review*, 187(3), 1062–1069, November 1969.
- [31] Stephen J. Brosnan and Robert L. Byer, "Optical parametric oscillator threshold and linewidth studies.", *IEEE Journal of Quantum Electronics*, QE-15(6), 415–431, June 1979.
- [32] Juh Tzeng Lue and Chien Jen Sun, "Limiting factors for parametric generation with focused high-order transverse- and multilongitudinal-mode lasers", *Journal of Optical Society of America B*, 4(12), 1958–1963, December 1987.
- [33] Takashi Kushida, Yuichi Tanaka, and Masahiro Ojima, "Tunable Picosecond Pulse Generation by Optical Parametric Oscillator", *Japanese Journal of Applied Physics*, 16(12), 2227–2235, December 1977.

- [34] Yuichi Tanaka, Takashi Kushida, and Shigeo Shionoya, "Broadly Tunable, Repetitive, Picosecond Parametric Oscillator", *Optics Communications*, 25(2), 273–276, May 1978.
- [35] G. I. Onishchukov, A. A. Fomichev, and A. I. Kholodnykh, "Picosecond Optical Parametric Oscillator Pumped by Radiation from a Continuously Excited YAG : Nd<sup>3+</sup> Laser", *Soviet Journal of Quantum Electronics*, 16(6), 1001–1002, August 1983.
- [36] A. Piskarskas, V. Smil'gyavichyus, A. Umbrasas, and I. Yuodishyus, "Parametric Generation of Picosecond Light Pulses in an LiNbO<sub>3</sub> Crystal at Repetition Frequencies up to 10 kHz", *Soviet Journal of Quantum Electronics*, 16(6), 841–843, June 1986.
- [37] D. T. Reid, M. Ebrahimzadeh, and W. Sibbett, "Noncritically phase-matched Ti:sapphire-pumped femtosecond optical parametric oscillator based on RbTiOAsO<sub>4</sub>", *Optics Letters*, 20(1), 55–57, January 1995.
- [38] M. Ebrahimzadeh, S. French, W. Sibbett, and A. Miller, "Picosecond Ti:sapphire-pumped optical parametric oscillator based on LiB<sub>3</sub>O<sub>5</sub>", *Optics Letters*, 20(2), 166–168, January 1995.
- [39] S. French, M. Ebrahimzadeh, and A. Miller, "High-power, high-repetition-rate picosecond optical parametric oscillator for the near- to mid-infrared", *Optics Letters*, 21(2), 131–133, January 1996.

- [40] G. R. Holtom, R. A. Crowell, and L. K. Cheng, "Femtosecond mid-infrared optical parametric oscillator based on CsTiOAsO<sub>4</sub>", *Optics Letters*, 20(18), 1880–1882, September 1995.
- [41] S. W. McCahon, S. A. Anson, D.-J. Jang, and T. F. Boggess, "Generation of 3-4  $\mu$ m femtosecond pulses from a synchronously pumped, critically phase-matched KTiOPO<sub>4</sub> optical parametric oscillator", *Optics Letters*, 20(22), 2309–2311, November 1995.
- [42] G. M. Gale, M. Cavallari, T. J. Driscoll, and F. Hache, "Sub-200fs tunable pulses in the visible from an 82-MHz optical parametric oscillator", *Optics Letters*, 20(14), 1562–1564, July 1995.
- [43] D. T. Reid, M. Ebrahimzadeh, and W. Sibbett, "Efficient femtosecond pulse generation in the visible in a frequency-doubled optical parametric oscillator based on RbTiOAsO<sub>4</sub>", *Journal of Optical Society of America B*, 12(6), 1157–1163, June 1995.
- [44] Y. R. Shen, *The Principles of Nonlinear Optics*. John Wiley & Sons, 1984.
- [45] G. C. Bhar and U. Chatterjee, "Analyses of Phase-Matching for Non-collinear Three-Wave Mixing in Uniaxial Crystals", *Japanese Journal of Applied Physics*, 29(6), 1103–1107, June 1990.
- [46] G. C. Bhar, U. Chatterjee, and S. Das, "A technique for the calculation of phase-matching angle for type-II noncollinear sum-frequency generation in negative uniaxial crystals", *Optics Communications*, 80, 381–384, January 1991.



- [47] Xue-Lin Yang, Sheng-Wu Xie, and Zhen-Hong Jia, "Noncritical phase-matching in the different frequency generation of noncollinear alignment: an exact analysis", *Applied Optics*, 33(31), 7518–7519, November 1994.
- [48] A. Agnesi, G. C. Reali, V. Kubecek, S. Kumazaki, Y. Takagi, and K. Yoshihara, " $\beta$ -Barium borate and lithium triborate picosecond parametric oscillators pumped by frequency-tripled passive negative-feedback mode-locked Nd:YAG laser", *Journal of Optical Society of America B*, 10(11), 2211–2217, November 1993.
- [49] Vitaly Krylov, Alexander Kalintsev, Alexander Rebane, Daniel Erni, and Urs P. Wild, "Noncollinear parametric generation in  $\text{LiIO}_3$  and  $\beta$ -barium borate by frequency-doubled femtosecond Ti:sapphire laser pulse", *Journal of Optical Society of America B*, 20(2), 151–153, January 1995.
- [50] U. Chatterjee, A. M. Rudra, P. K. Datta, G. C. Bhar, and T. Sasaki, "Efficient tunable near infrared source by difference frequency mixing in potassium titanyl phosphate crystal", *Applied Physics*, 28(2), 275–279, February 1995.
- [51] Lawrence A. W. Gloster, Zhi Xing Jiang, and Terence A. King, "Characterization of an Nd:YAG-Pumped  $\beta$ -BaB<sub>2</sub>O<sub>4</sub> Optical Parametric Oscillator in Collinear and Noncollinear Phase-Matched Configurations", *IEEE Journal of Quantum Electronics*, 30(12), 2961–2969, December 1994.
- [52] L. A. W. Gloster, I. T. McKinnie, and T. A. King, "Noncollinear phase matching in a type I barium borate optical parametric oscillator", *Optics Communications*, 112, 328–332, December 1994.

- [53] M. J. T. Milton, T. J. McIlveen, D. C. Hanna, and P. T. Woods, "High-efficiency infrared generation by difference-frequency mixing using tangential phase matching", *Optics Communications*, 87, 273–277, February 1991.
- [54] R. C. Eckardt, H. Masuda, Y. X. Fan, and R. L. Byer, "Absolute and relative nonlinear optical coefficients of KDP, KD\*P, BaB<sub>2</sub>O<sub>4</sub>, LiIO<sub>3</sub>, MgO:LiNbO<sub>3</sub>, and KTP measured by phase-matched second-harmonic generation.", *IEEE Journal of Quantum Electronics*, QE-26, 922–933, 1990.
- [55] H. Vanherzeele and J.D. Bierlein, "Magnitude of the nonlinear-optical coefficients of KTiOPO<sub>4</sub>", *Optics Letters*, 17, 982–984, 1992.
- [56] J.M. Liu and J.K. Chee, "Passive mode locking of a cw Nd:YLF laser with a nonlinear external coupled cavity", *Optics Letters*, 15(12), 685–687, June 1990.
- [57] J.K. Chee, J.M. Liu, and M.N. Kong, "Cavity-detuning characteristics of cw additive-pulse mode-locked Nd:YLF laser", *IEEE Journal of Quantum Electronics*, 28(3), 700–709, March 1992.
- [58] D. von der Linde, "Characterization of the noise in continuously operating mode-locked lasers", *Applied Physics B*, 39(1), 201–217, January 1986.
- [59] U. Keller, K.D. Li, M. Rodwell, and D.M. Bloom, "Noise characterization of femtosecond fiber Raman soliton lasers", *IEEE Journal of Quantum Electronics*, 25(3), 280–288, March 1989.

- [60] M.J. Rodwell, D.M. Bloom, and K.J. Weingarten, "Subpicosecond laser timing stablization", *IEEE Journal of Quantum Electronics*, 25(4), 817-827, April 1989.
- [61] A. Finch, X. Zhu, P.N. Kean, and W. Sibbett, "Noise characterization of mode-locked color-center laser sources", *IEEE Journal of Quantum Electronics*, 26(6), 1115-1123, June 1990.
- [62] U. Keller, C.E. Socolich, G. Sucha, M.N. Islam, and M. Wegener, "Noise characterization of femtosecond color-center lasers", *Optics Letters*, 15(17), 974-976, September 1990.
- [63] J. Son, J.V. Rudd, and J.F. Whitaker, "Noise characterization of a self-mode-locked Ti:sapphire laser", *Optics Letters*, 17(10), 733-735, May 1992.
- [64] G.T. Harvey, M.S. Heutmaker, P.R. Smith, M.C. Nuss, U. Keller, and J.A. Valdmanis, "Timing jittering and pump-induced amplitude modulation in the colliding-pulse-mode-locked (CPM) laser", *IEEE Journal of Quantum Electronics*, 27(2), 295-301, February 1991.
- [65] J. Goodberlet, J. Jacobson, J.G. Fujimoto, P.A. Shultz, and T.Y. Fan, "Self-starting additive-pulse mode-locked diode-pumped Nd:YAG laser", *Optics Letters*, 15(9), 504-506, May 1990.
- [66] E. S. Wachman, D. C. Edelstein, and C. L. Tang, "Continuous-wave mode-locked and dispersion-compensated femtosecond optical parametric oscillator", *Optics Letters*, 15(2), 136-138, January 1990.

- [67] John. D. Bierlein and Herman Vanherzeele, "Potassium titanyl phosphate: properties and new applications", *Journal of Optical Society of America B*, 6(4), 622–633, 1989.
- [68] E. C. Cheung, K. Koch, G. T. Moore, and J. M. Liu, "Measurements of second-order nonlinear optical coefficients from the spectral brightness of parametric fluorescence", *Optics Letters*, 19, 168–170, 1994.
- [69] J. M. Liu, Gousheng Zhou, and S. J. Pyo, "Parametric gain of the generation and amplification of ultrashort optical pulses", *Journal of Optical Society of America B*, 12(11), 2274–2287, 1995.
- [70] Koelchner, *Solid State Laser Engineering*. Springer, 1988.
- [71] A. Robertson, N. Langford, and A. I. Ferguson, "Frequency doubled diode-pumped pulse compressed additive-pulse mode-locked Nd<sup>3+</sup> doped lithium yttrium fluoride laser producing 250 fs duration pulses", *Applied Physics Letters*, 66(20), 2622–2624, May 1995.
- [72] J. A. Giodmaine, M. A. Duguay, and J. W. Hansen, "Compression of optical pulses", *IEEE Journal of Quantum Electronics*, QE-4(5), 252–255, May 1968.
- [73] E. B. Treacy, "Optical pulse compression with diffraction gratings", *IEEE Journal of Quantum Electronics*, QE-5(9), 454–458, September 1969.
- [74] R. L. Fork, O. E. Martinez, and J. P. Gordon, "Negative dispersion using pairs of prisms", *Optics Letters*, 9(5), 150–152, May 1984.

- [75] J. K. Chee and J. M. Liu, "Compression of cw passively additive-pulse mode-locked Nd:YLF laser pulses", *Optics Communications*, 89(5), 414–418, May 1992.
- [76] L. P. Chen, Y. Wang, and J. M. Liu, "Singly resonant optical paraetric oscillator synchronously pumped by frequency-doubled additive-pulse mode-locked Nd:YLF laser pulses", *Journal of Optical Society of America B*, 12(11), 2192–2198, 1995.
- [77] M.J.W. Rodwell, K.J. Weingarten, D.M. Bloom, T. Bear, and B.H. Kolner, "Reduction of timing flunctuations in a mode-locked Nd:YAG laser by electronics feedback", *Optics Letters*, 11(10), 638–640, October 1986.
- [78] M.C. Nuss, U. Keller, G.T. Harvey, M.S. Heutmaker, and P.R. Smith, "Amplitude noise reduction of 50dB in colliding-pulse-mode-locked dye lasers", *Optics Letters*, 15(18), 1026–1028, September 1990.
- [79] S.B. Darack, D.R. Dykaar, and G.T. Harvey, "Timing-jitter stabilization of a colliding-pulse mode-locked laser by active control of the cavity length", *Optics Letters*, 16(21), 1677–1679, November 1991.
- [80] D.E. Spence, J.M. Evans, W.E. Sleat, and W. Sibbet, "Regeneratively initiated self-mode-locked Ti:sapphire laser", *Optics Letters*, 16(22), 1762–1764, November 1991.
- [81] P.A. Harten, S.G. Lee, J.P. Sokoloff, J.R. Salcedo, and N. Peyghambarian, "Noise in a dual dye jet hybridly mode-locked near infrared femtosecond laser", *Optics Communications*, 91(5), 465–473, August 1992.

- [82] M. Ding and K. Kikuchi, "Noise characteristics of femtosecond fiber Raman soliton laser with high-Q cavity", *IEEE Photonics Technology Letters*, 4(10), 1109–1112, October 1992.
- [83] D. Henderson and A.G. Roddie, "A comparison of spectral and temporal techniques for the measurement of timing jitter and their application in a mode-locked argon ion and dye laser system", *Optics Communications*, 100(5), 456–460, July 1993.
- [84] T.B. Simpson, T. Day, F. Doft, M.M. Malley, and G.W. Sutton, "Frequency-stabilized mode-locked solid-state laser system for precision range-Doppler image", *IEEE Journal of Quantum Electronics*, 29(9), 2489–2496, September 1993.
- [85] I. G. Fuss, "An interpretation of the spectral measurement of optical pulse train noise", *IEEE Journal of Quantum Electronics*, 30(17), 2707–2710, November 1994.
- [86] Yong Wang, L.P. Chen, and J.M. Liu, "Noise characterization of mode-locked lasers by comparing power spectra of the fundamental and second harmonic pulses", *Optics Letters*, 20(20), October 1995.
- [87] H.A. Haus and A. Mecozzi, "Noise of mode-locked laser", *IEEE Journal of Quantum Electronics*, 29(3), 983–996, March 1993.
- [88] A. Papoulis, *Probability, Random Variables, and Stochastic Processes*. McGraw-Hill, 1984.

# **A Spectral Measurement of The Noise in Continuous-Wave Mode-Locked Laser Pulses**

A theoretical analysis of the noise of a periodic optical pulse train is presented. It is shown that the amplitude fluctuation, the pulsewidth fluctuation, the pulse timing jitter, and the cross correlations between any two of these three noise parameters can be separately quantified by comparing the noise power spectra of the fundamental pulses and those of the second harmonic pulses. The noise characteristics of an actively mode-locked Nd:YLF laser are presented to demonstrate this technique.

## **A.1 Introduction**

Characterization of the noise in the optical pulse train of a continuous-wave (CW) mode-locked laser using a spectral technique was first presented by von der Linde[58]. von der Linde's noise model is under the assumptions that the pulsewidth has no fluctuation, that the pulse timing jitter and the amplitude fluctuation (peak intensity fluctuation) is small, and that the amplitude fluctuation and the pulse timing jitter are not correlated. Under these assumptions, the pulse-energy fluctuation can be interpreted as the amplitude fluctuation. Using this model, only the power spectral density of the pulse amplitude fluctuation and that of the pulse timing jitter can be deduced from the power spectra measured with the combination of a photodetector and a spectrum analyzer. Several research groups have used this power-spectrum technique to measure the amplitude fluctuation and the pulse timing jitter of several CW mode-locked lasers[77, 59, 60, 61, 62, 78, 64, 79, 80, 81,

82, 83, 84, 63]. For most mode-locked lasers, however, there is no justification that the pulsewidth fluctuation and the cross correlations between the pulsewidth fluctuation and the amplitude fluctuation are negligible[85]. When the pulsewidth fluctuation and the cross correlations between the noise parameters are considered, there is a distinction between the pulse-amplitude fluctuation and the pulse-energy fluctuation. In this general condition, the amplitude noise defined in the earlier papers [58, 59, 60, 61, 62, 63] is not really the amplitude fluctuation of the pulse peak intensity, but is rather the pulse-energy fluctuation of the pulse. Although measurements of the power spectra of higher harmonics were suggested to obtain more detailed information of laser pulsewidth fluctuation[58], no theoretical analysis has been carried out. Nor has any characterization procedure using the higher harmonics to deduce more detailed information on the laser noise been proposed. Recently, we have demonstrated the possibility of deducing various noise parameters of a mode-locked laser pulse train by comparing the noise power spectra of the fundamental and the second harmonic pulses[86]. In this paper, we carry out the theoretical analysis and present the method for separately quantifying six key noise parameters of a pulse train, including the amplitude fluctuation, the pulsewidth fluctuation, the pulse timing jitter, and the cross correlations between any two of these three noise parameters. The experimental results of the noise parameters of an actively mode-locked Nd:YLF laser system are also presented to demonstrate this technique.



## A.2 Theoretical Derivation

Harmonic signals of a laser pulse train offer a convenient way to extract more information about the pulse train itself due to the nonlinear nature of the harmonic-generation process. In order to fully separate various noise parameters, including the amplitude fluctuation, the pulsewidth fluctuation, the pulse timing jitter, and the cross correlations between these noise parameters, of a given laser pulse train, one can measure both the pulse train itself (the fundamental) and its frequency-doubled signal (the second harmonic). When the second harmonic is generated at the low-efficiency limit without saturation, it is quadratically dependent on the instantaneous fundamental pulse intensity. In this case, the noise parameters of the second harmonic pulse train are determined by those of the fundamental pulse train through very simple relations. Because of the nonlinear nature of the harmonic generation process, these relations yield additional independent equations connecting the noise parameters, thus allowing one to deduce these parameters separately. In the following analysis, we discuss the noise models for the fundamental and the second harmonic, the approximations made in the analysis, the corresponding power spectra of the fundamental and the second harmonic, and the effect of the response of the detection system.

### A.2.1 Noise Model

The intensity of a periodic pulse train can be modeled as:

$$I_1(t) = \sum_{n=-\infty}^{+\infty} (I_1 + I_{1n}) h_1 \left( \frac{t - nT - T_n}{\Delta t_1 + \Delta t_{1n}} \right), \quad (73)$$

where  $h_1(t)$  is the normalized dimensionless intensity shape function of the individual pulses,  $T$  is the average repetition period of the pulses,  $T_n$  is the pulse timing jitter,  $I_1$  is the average value of the intensity amplitude,  $I_{1n}$  describes the intensity amplitude fluctuation,  $\Delta t_1$  is the average full width at half-maximum (FWHM) pulsewidth, and the sequence  $\Delta t_{1n}$  describes the pulsewidth fluctuation. The maximum of the intensity shape function  $h_1(t)$  is normalized to unity. In the limit of negligible pump depletion and no saturation for the second-harmonic generation process, the intensity of the second harmonic of this fundamental pulse train is quadratically dependent on that of the fundamental and can be modeled as:

$$\begin{aligned} I_2(t) &= K \sum_{n=-\infty}^{+\infty} (I_1 + I_{1n})^2 h_1^2 \left( \frac{t - nT - T_n}{\Delta t_1 + \Delta t_{1n}} \right) \\ &= K \sum_{n=-\infty}^{+\infty} (I_1 + I_{1n})^2 h_2 \left( \frac{t - nT - T_n}{\Delta t_1 + \Delta t_{1n}} \right), \end{aligned} \quad (74)$$

where  $K$  is a constant determined by the efficiency of the second-harmonic generation process and  $h_2(t) = h_1^2(t)$ .

### A.2.2 Approximations

In our analysis, we assume that the stochastic sequences,  $I_{1n}$ ,  $T_n$ , and  $\Delta t_{1n}$ , are stationary and the intensity  $I_1(t)$  is a cyclostationary function. Under the assumptions that the quantities  $I_{1n}/I_1$ ,  $\Delta t_{1n}/\Delta t_1$ , and  $2\pi f_m T_n$  are all much less than unity, where  $f_m$  is the maximum frequency measured, and that the function  $h_1(t)$  has a convergent Taylor series expansion about the point  $t=0$ , it is shown in Appendix B that the intensity function  $I_1(t)$  can be approximated by the following expansion:

$$I_1(t) = I_1 \sum_n \left[ \left( 1 + \frac{I_{1n}}{I_1} \right) h_1 \left( \frac{t - nT}{\Delta t_1} \right) \right]$$

$$\begin{aligned}
& - \left( T_n + \frac{I_{1n}T_n}{I_1} - \frac{\Delta t_{1n}T_n}{\Delta t_1} \right) \dot{h}_1 \left( \frac{t-nT}{\Delta t_1} \right) \\
& - \left( \frac{\Delta t_{1n}}{\Delta t_1} - \frac{\Delta t_{1n}^2}{\Delta t_1^2} + \frac{I_{1n}\Delta t_{1n}}{I_1\Delta t_1} \right) (t-nT) \dot{h}_1 \left( \frac{t-nT}{\Delta t_1} \right) \\
& + \frac{1}{2} T_n^2 \ddot{h}_1 \left( \frac{t-nT}{\Delta t_1} \right) + \frac{\Delta t_{1n}T_n}{\Delta t_1} (t-nT) \ddot{h}_1 \left( \frac{t-nT}{\Delta t_1} \right) \\
& + \frac{1}{2} \frac{\Delta t_{1n}^2}{\Delta t_1^2} (t-nT)^2 \ddot{h}_1 \left( \frac{t-nT}{\Delta t_1} \right) \Big], \tag{75}
\end{aligned}$$

where  $\dot{h}_1$  and  $\ddot{h}_1$  are the first- and second-order time derivatives of the pulse shape function, respectively. Similarly, it can be shown that the second harmonic intensity function  $I_2(t)$  is approximated by the following expansion:

$$\begin{aligned}
I_2(t) = K I_1^2 \sum_n & \left[ \left( 1 + \frac{2I_{1n}}{I_1} + \frac{I_{1n}^2}{I_1^2} \right) h_2 \left( \frac{t-nT}{\Delta t_1} \right) \right. \\
& - \left( T_{1n} + \frac{2I_{1n}T_{1n}}{I_1} - \frac{\Delta t_{1n}T_{1n}}{\Delta t_1} \right) \dot{h}_2 \left( \frac{t-nT}{\Delta t_1} \right) \\
& - \left( \frac{\Delta t_{1n}}{\Delta t_1} - \frac{\Delta t_{1n}^2}{\Delta t_1^2} + \frac{2I_{1n}\Delta t_{1n}}{I_1\Delta t_1} \right) (t-nT) \dot{h}_2 \left( \frac{t-nT}{\Delta t_1} \right) \\
& + \frac{1}{2} T_{1n}^2 \ddot{h}_2 \left( \frac{t-nT}{\Delta t_1} \right) + \frac{\Delta t_{1n}T_{1n}}{\Delta t_1} (t-nT) \ddot{h}_2 \left( \frac{t-nT}{\Delta t_1} \right) \\
& \left. + \frac{1}{2} \frac{\Delta t_{1n}^2}{\Delta t_1^2} (t-nT)^2 \ddot{h}_2 \left( \frac{t-nT}{\Delta t_1} \right) \right]. \tag{76}
\end{aligned}$$

### A.2.3 Power Spectra

The power spectra of both the fundamental and second-harmonic pulse trains can be obtained from the Fourier transform of the time-averaged autocorrelation of  $I_k(t)$ , where  $k = 1$  for the fundamental and  $k = 2$  for the second harmonic. The detailed derivation of the time-averaged autocorrelation and the power spectrum of  $I_1(t)$  is given in Appendix C. The power spectra of the optical signal  $I_k(t)$  can be approximated by the following equation:

$$P_{I_k}(\omega) \approx K^{2(k-1)} \frac{I_1^2}{T^2} \Delta t_1^2 |H_k(\Delta t_1 \omega)|^2 \sum_n \left\{ 2\pi \delta \left( \omega - n \frac{2\pi}{T} \right) \right.$$

$$\begin{aligned}
& +k^2 S_{\hat{I}_1} \left( \omega - n \frac{2\pi}{T} \right) + \frac{S_{\Delta t_1} \left( \omega - n \frac{2\pi}{T} \right)}{\Delta t_1^2} + 2k \frac{\text{Re}[S_{\Delta t_1 \hat{I}_1} \left( \omega - n \frac{2\pi}{T} \right)]}{\Delta t_1} \\
& + \omega \cdot 2k \cdot \text{Im} \left[ S_{T \hat{I}_1} \left( \omega - n \frac{2\pi}{T} \right) \right] + \omega \cdot 2 \frac{\text{Im}[S_{T \Delta t_1} \left( \omega - n \frac{2\pi}{T} \right)]}{\Delta t_1} \\
& + \omega^2 \cdot S_T \left( \omega - n \frac{2\pi}{T} \right) \\
& + \omega \cdot \text{Re} \left[ \frac{d}{d\omega} \ln H_k(\Delta t_1 \omega) \right] \cdot \frac{2S_{\Delta t_1} \left( \omega - n \frac{2\pi}{T} \right)}{\Delta t_1^2} \\
& + \omega \cdot \text{Re} \left[ \frac{d}{d\omega} \ln H_k(\Delta t_1 \omega) \cdot \frac{2k S_{\Delta t_1 \hat{I}_1} \left( \omega - n \frac{2\pi}{T} \right)}{\Delta t_1} \right] \Bigg\} \quad (77)
\end{aligned}$$

where  $k = 1$  for the fundamental and  $k = 2$  for the second harmonic,  $H_k(\omega)$  is the Fourier transform of the pulse shape function  $h_k(t)$ ,  $S_{\hat{I}_1}(\omega)$  is the power spectral density of the normalized amplitude noise  $I_{1n}/I_1$ ,  $S_{\Delta t_1}(\omega)$  is the power spectral density of the pulsewidth fluctuation  $\Delta t_{1n}$ ,  $S_T(\omega)$  is the power spectral density of the pulse timing jitter noise  $T_n$ .  $S_{\Delta t_1 \hat{I}_1}(\omega)$  is the power spectral density of the cross correlation between the pulsewidth fluctuation  $\Delta t_{1n}$  and the normalized amplitude noise  $I_{1n}/I_1$ ; the other two cross correlation parameters,  $S_{T \hat{I}_1}$  and  $S_{T \Delta t_1}$ , are similarly defined. If the temporal pulse shape is symmetric, both  $H_1(\Delta t_1 \omega)$  and  $H_2(\Delta t_1 \omega)$  are real functions. For most pulse shapes of interest,

$$\frac{2}{\Delta t_1^2} \frac{d}{d\omega} \ln H_k(\Delta t_1 \omega) \approx -\beta_k \cdot \omega \quad (78)$$

where  $\beta_k$  are pulse shape-dependent constants. Then, the power spectra can be further simplified to have the following form:

$$\begin{aligned}
P_{I_k}(\omega) = & K^{2(k-1)} \frac{I_1^{2k}}{T^2} \Delta t_1^2 |H_k(\Delta t_1 \omega)|^2 \sum_n \left\{ 2\pi \delta \left( \omega - n \frac{2\pi}{T} \right) \right. \\
& + k^2 S_{\hat{I}_1} \left( \omega - n \frac{2\pi}{T} \right) + \frac{S_{\Delta t_1} \left( \omega - n \frac{2\pi}{T} \right)}{\Delta t_1^2} + 2k \frac{\text{Re} [S_{\Delta t_1 \hat{I}_1} \left( \omega - n \frac{2\pi}{T} \right)]}{\Delta t_1} \\
& \left. + \omega \cdot 2k \cdot \text{Im} \left[ S_{T \hat{I}_1} \left( \omega - n \frac{2\pi}{T} \right) \right] + \omega \cdot 2 \frac{\text{Im} [S_{T \Delta t_1} \left( \omega - n \frac{2\pi}{T} \right)]}{\Delta t_1} \right\}
\end{aligned}$$

Pulse shape, $h_1(t)$	$\beta_1$	$\beta_2$
$\exp(-4\ln 2 \cdot t^2)$	$\frac{1}{4 \ln 2}$	$\frac{1}{8 \ln 2}$
$\text{sech}^2(1.76t)$	$\frac{\pi^2}{6} \left(\frac{1}{1.76}\right)^2$	$\left(\frac{\pi^2}{6} - 1\right) \left(\frac{1}{1.76}\right)^2$

Table 2:  $\beta_k$  of the Gaussian and  $\text{sech}^2$  pulse shape

$$\begin{aligned}
& + \omega^2 \cdot \left[ S_T \left( \omega - n \frac{2\pi}{T} \right) - \beta_k S_{\Delta t_1} \left( \omega - n \frac{2\pi}{T} \right) \right] \\
& - \omega^2 \cdot k \beta_k \Delta t_1 \text{Re} \left[ S_{\Delta t_1 \hat{I}_1} \left( \omega - n \frac{2\pi}{T} \right) \right] \}.
\end{aligned} \tag{79}$$

The values of  $\beta_k$  for the Gaussian and hyperbolic secant-squared pulse shapes, which are the most commonly seen optical pulse shapes, are summarized in Table 2.

In order to explain the physical meaning of each terms in the power spectra we obtain, we further define the normalized pulse-energy fluctuation as[85]

$$\frac{E_{1n}}{E_1} = \frac{I_{1n}}{I_1} + \frac{\Delta t_{1n}}{\Delta t_1}. \tag{80}$$

By using this definition, the power spectra can be expressed as:

$$\begin{aligned}
P_{I_k}(\omega) = & K^{2(k-1)} \frac{I_1^{2k}}{T^2} \Delta t_1^2 |H_k(\Delta t_1 \omega)|^2 \sum_n \left\{ 2\pi \delta \left( \omega - n \frac{2\pi}{T} \right) + S_{\widehat{E_k}} \left( \omega - n \frac{2\pi}{T} \right) \right. \\
& \left. + \omega \cdot S_{T\widehat{E_k}} \left( \omega - n \frac{2\pi}{T} \right) + \omega^2 \cdot S_{J_k} \left( \omega - n \frac{2\pi}{T} \right) \right\},
\end{aligned} \tag{81}$$

where the normalized energy noise spectral density,  $S_{\widehat{E_k}}(\omega)$ , is defined as

$$S_{\widehat{E_k}}(\omega) = k^2 S_{\widehat{I_1}}(\omega) + \frac{S_{\Delta t_1}(\omega)}{\Delta t_1^2} + 2k \frac{\text{Re} [S_{\Delta t_1 \hat{I}_1}(\omega)]}{\Delta t_1}, \tag{82}$$

the cross-correlation noise spectral density,  $S_{T\widehat{E}_k}(\omega)$ , is defined as

$$S_{T\widehat{E}_k}(\omega) = 2k \cdot \text{Im} [S_{T\widehat{I}_1}(\omega)] + 2 \frac{\text{Im} [S_{T\Delta t_1}(\omega)]}{\Delta t_1}, \quad (83)$$

and the total jitter noise spectral density,  $S_{J_k}(\omega)$ , is defined as

$$S_{J_k}(\omega) = S_T(\omega) - \beta_k S_{\Delta t_1}(\omega) - k\beta_k \Delta t_1 \text{Re} [S_{\Delta t_1 \widehat{I}_1}(\omega)]. \quad (84)$$

It is seen that the fluctuation of pulsewidth contributes to both  $S_{\widehat{E}_k}(\omega)$  and  $S_{J_k}(\omega)$ , and the noise in the second harmonic pulses is enhanced due to its nonlinear dependence on the amplitude fluctuation. If the pulsewidth fluctuation and the cross correlation noise are negligible, then  $S_{\widehat{E}_1}(\omega) = S_{\widehat{I}_1}(\omega)$ ,  $S_{T\widehat{E}_1}(\omega) = 0$ , and  $S_{J_1}(\omega) = S_T(\omega)$ . In this case, Eq. 81 for the fundamental is reduced to that used so far in the literature [58, 59, 63, 85].

#### A.2.4 Response of The Detection System

When an optical pulse train is incident on a photodetector, the photocurrent registered by the detection system is given by

$$i_k(t) = \int_{-\infty}^{+\infty} g_k(t-t') I_k(t') dt', \quad (85)$$

where  $g_k(t)$  is impulse response function of the detection system, including the photodetector, any electric transmission cables, and the spectrum analyzer. It follows that the truncated power spectrum of this generated photocurrent is given by

$$P_{i_k}(\omega) = 2\pi |g_k(\omega)|^2 P_{I_k}(\omega), \quad (86)$$

where  $g_k(\omega)$  is the Fourier transform of  $g_k(t)$ . Within the bandwidth of  $g_k(\omega)$ , the truncated power spectrum of the photocurrent,  $P_{i_k}(\omega)$ , can represent the power

spectrum of the optical signal. Under the condition that the maximum frequency measured is smaller than  $(2\pi\Delta t_1)^{-1}$ ,  $H_k(\Delta t_1\omega)$  can be taken as a constant. The measured power spectrum of the photocurrent within the bandwidth of the detection system can be derived from Eq. 81 to yield

$$P_{i_k}(\omega) = P_{C_k} \sum_n \left\{ 2\pi\delta\left(\omega - n\frac{2\pi}{T}\right) + S_{\widehat{E_k}}\left(\omega - n\frac{2\pi}{T}\right) + \omega \cdot S_{T\widehat{E_k}}\left(\omega - n\frac{2\pi}{T}\right) + \omega^2 \cdot S_{J_k}\left(\omega - n\frac{2\pi}{T}\right) \right\}, \quad (87)$$

where  $P_{C_k}$  is a constant which represents the carrier power.

### A.3 Measurement Method

In experiments, we usually measure the power spectrum in the unit of the frequency  $f$  (Hz) instead of that of the radial frequency  $\omega$ . It is convenient to define the power spectrum in terms of frequency  $f$  for experimental purposes. Using Eq. 87, we have

$$P_{i_k}(f) = P_{C_k} \sum_n \{ \delta(f - nf_0) + S_{\widehat{E_k}}(f - nf_0) + (2\pi nf)^2 \cdot S_{T\widehat{E_k}}(f - nf_0) + (2\pi nf)^2 \cdot S_{J_k}(f - nf_0) \}. \quad (88)$$

where  $f = \omega/2\pi$ ,  $f_0 (= 1/T)$  is the repetition frequency of the pulse train, and  $k = 1, 2$  for the fundamental and second harmonic, respectively. Using Eq. 88 we can define the  $n$ th harmonic side-band noise spectral density of the fundamental and the second harmonic pulse trains as

$$S_{n_k}(f) = S_{\widehat{E_k}}(f) + (2\pi nf_0) \cdot S_{T\widehat{E_k}}(f) + (2\pi nf_0)^2 \cdot S_{J_k}(f), \quad (89)$$

where  $n$  is the harmonic number of the power spectrum,  $f$  is the frequency offset to the  $n$ th carrier frequency,

$$S_{\widehat{E_k}}(f) = k^2 S_{\widehat{I_1}}(f) + \frac{S_{\Delta t_1}(f)}{\Delta t_1^2} + 2k \frac{\text{Re}[S_{\Delta t_1 \widehat{I_1}}(f)]}{\Delta t_1} \quad (90)$$

is the normalized energy noise spectral density,

$$S_{T\widehat{E}_k}(f) = 2\{k \cdot \text{Im}[S_{T\widehat{I}_1}(f)] + \frac{\text{Im}[S_{T\Delta t_1}(f)]}{\Delta t_1}\} \quad (91)$$

is the spectral density of the cross correlation between the pulse timing jitter and the normalized energy fluctuation, and

$$S_{J_k}(f) = S_T(f) - \beta_k S_{\Delta t_1}(f) - k\beta_k \Delta t_1 \text{Re}[S_{\Delta t_1 \widehat{I}_1}(f)] \quad (92)$$

is the total jitter noise spectral density.

In experiments, the total noise power for various harmonic order  $n$  can be obtained by integrating the side-band noise spectral density  $S_{n_k}(f)$ . By integrating Eq. 89, we get following relation for the total noise power at the harmonic order  $n$ :

$$\sigma_{n_k}^2 = \sigma_{\widehat{E}_k}^2 + (2\pi n f_0) \cdot C_{T\widehat{E}_k} + (2\pi n f_0)^2 \cdot \sigma_{J_k}^2 \quad (93)$$

where  $\sigma_{n_k}^2$ ,  $\sigma_{\widehat{E}_k}$ ,  $\sigma_{J_k}$ , and  $C_{T\widehat{E}_k}$  are the total noise power, the rms normalized energy fluctuation, the rms total jitter, and the cross correlation between the pulse timing jitter and the normalized energy fluctuation, respectively. Assuming the noise spectral density is symmetric, the parameters  $\sigma_{\widehat{E}_k}$ ,  $\sigma_{J_k}$ , and  $C_{T\widehat{E}_k}$  are, respectively, defined by the following equations:

$$\begin{aligned} \sigma_{\widehat{E}_k} &= \left[ 2 \int_{f_L}^{f_H} \frac{S_{\widehat{E}_k}(f)}{1.2B} df \right]^{\frac{1}{2}} = \left[ \frac{1}{\pi} \int_{\omega_L}^{\omega_H} \frac{S_{\widehat{E}_k}(\omega)}{1.2B} d\omega \right]^{\frac{1}{2}} \\ \sigma_{J_k} &= \left[ 2 \int_{f_L}^{f_H} \frac{S_{J_k}(f)}{1.2B} df \right]^{\frac{1}{2}} = \left[ \frac{1}{\pi} \int_{\omega_L}^{\omega_H} \frac{S_{J_k}(\omega)}{1.2B} d\omega \right]^{\frac{1}{2}} \\ C_{T\widehat{E}_k} &= 2 \int_{f_L}^{f_H} \frac{S_{T\widehat{E}_k}(f)}{1.2B} df = \frac{1}{\pi} \int_{\omega_L}^{\omega_H} \frac{S_{T\widehat{E}_k}(\omega)}{1.2B} d\omega, \end{aligned} \quad (94)$$

where 1.2 is the factor for the equivalent noise bandwidth of the spectrum analyzer,  $B$  is the resolution bandwidth, and  $f_L$  and  $f_H$  are the lower and upper limits of



the frequency offset[63]. The values of  $\sigma_{\widehat{E_k}}$ ,  $\sigma_{J_k}$ , and  $C_{T\widehat{E_k}}$  can be determined by measuring the total noise power  $\sigma_{n_k}^2$  of various harmonic order  $n$  since the total noise power is a quadratic function of the harmonic numbers  $n$ , as can be seen in Eq. 93.

By integrating Eqs. 90-92 for the fundamental and the second harmonic over a given frequency range, we get the following equations:

$$\sigma_{\widehat{E_1}}^2 = \sigma_{\widehat{I_1}}^2 + \frac{\sigma_{\Delta t_1}^2}{\Delta t_1^2} + \frac{2}{\Delta t_1} C_{\Delta t_1 \widehat{I_1}}, \quad (95)$$

$$\sigma_{\widehat{E_2}}^2 = 4\sigma_{\widehat{I_1}}^2 + \frac{\sigma_{\Delta t_1}^2}{\Delta t_1^2} + \frac{4}{\Delta t_1} C_{\Delta t_1 \widehat{I_1}}, \quad (96)$$

$$C_{T\widehat{E_1}} = C_{T\widehat{I_1}} + \frac{C_{T\Delta t_1}}{\Delta t_1}, \quad (97)$$

$$C_{T\widehat{E_2}} = 2C_{T\widehat{I_1}} + \frac{C_{T\Delta t_1}}{\Delta t_1}, \quad (98)$$

$$\sigma_{J_1}^2 = \sigma_{T_1}^2 - \beta_1 \sigma_{\Delta t_1}^2 - \beta_1 \Delta t_1 C_{\Delta t_1 \widehat{I_1}}, \quad (99)$$

$$\sigma_{J_2}^2 = \sigma_{T_1}^2 - \beta_2 \sigma_{\Delta t_1}^2 - 2\beta_2 \Delta t_1 C_{\Delta t_1 \widehat{I_1}}, \quad (100)$$

where the  $\sigma_{\widehat{I_1}}$ ,  $\sigma_{\Delta t_1}$ ,  $\sigma_T$ ,  $C_{\Delta t_1 \widehat{I_1}}$ ,  $C_{T\widehat{I_1}}$ , and  $C_{T\Delta t_1}$  are, respectively, the rms normalized pulse-amplitude fluctuation, the rms pulsewidth fluctuation, the rms pulse timing jitter, the cross correlation between the pulsewidth fluctuation and the normalized amplitude fluctuation, the cross correlation between the pulse timing jitter and the normalized amplitude fluctuation, and the cross correlation between the pulse timing jitter and the pulsewidth fluctuation. The parameters  $\sigma_{\widehat{I_1}}$ ,  $\sigma_{\Delta t_1}$ ,  $\sigma_T$ ,  $C_{\Delta t_1 \widehat{I_1}}$ ,  $C_{T\widehat{I_1}}$ , and  $C_{T\Delta t_1}$  are defined by the following equations:

$$\begin{aligned} \sigma_{\widehat{I_1}} &= \left[ 2 \int_{f_L}^{f_H} \frac{S_{\widehat{I_1}}(f)}{1.2B} df \right]^{\frac{1}{2}} = \left[ \frac{1}{\pi} \int_{\omega_L}^{\omega_H} \frac{S_{\widehat{I_1}}(\omega)}{1.2B} d\omega \right]^{\frac{1}{2}} \\ \sigma_{\Delta t_1} &= \left[ 2 \int_{f_L}^{f_H} \frac{S_{\Delta t_1}(f)}{1.2B} df \right]^{\frac{1}{2}} = \left[ \frac{1}{\pi} \int_{\omega_L}^{\omega_H} \frac{S_{\Delta t_1}(\omega)}{1.2B} d\omega \right]^{\frac{1}{2}} \end{aligned}$$

$$\begin{aligned}
\sigma_T &= \left[ 2 \int_{f_L}^{f_H} \frac{S_T(f)}{1.2B} df \right]^{\frac{1}{2}} = \left[ \frac{1}{\pi} \int_{\omega_L}^{\omega_H} \frac{S_T(\omega)}{1.2B} d\omega \right]^{\frac{1}{2}} \\
C_{\Delta t_1 \hat{I}_1} &= 2 \int_{f_L}^{f_H} \frac{S_{\Delta t_1 \hat{I}_1}(f)}{1.2B} df = \frac{1}{\pi} \int_{\omega_L}^{\omega_H} \frac{S_{\Delta t_1 \hat{I}_1}(\omega)}{1.2B} d\omega \\
C_{T \hat{I}_1} &= 2 \int_{f_L}^{f_H} \frac{S_{T \hat{I}_1}(f)}{1.2B} df = \frac{1}{\pi} \int_{\omega_L}^{\omega_H} \frac{S_{T \hat{I}_1}(\omega)}{1.2B} d\omega \\
C_{T \Delta t_1} &= 2 \int_{f_L}^{f_H} \frac{S_{T \Delta t_1}(f)}{1.2B} df = \frac{1}{\pi} \int_{\omega_L}^{\omega_H} \frac{S_{T \Delta t_1}(\omega)}{1.2B} d\omega
\end{aligned} \tag{101}$$

Because there are six equations (Eqs. 95–100) for six unknown quantities,  $\sigma_{\hat{I}_1}$ ,  $\sigma_{\Delta t_1}$ ,  $\sigma_T$ ,  $C_{\Delta t_1 \hat{I}_1}$ ,  $C_{T \hat{I}_1}$ , and  $C_{T \Delta t_1}$ , the noise characteristics of a mode-locked laser can be completely characterized when the values of  $\sigma_{\hat{E}_1}$ ,  $\sigma_{\hat{E}_2}$ ,  $C_{T \hat{E}_1}$ ,  $C_{T \hat{E}_2}$ ,  $\sigma_{J_1}$ , and  $\sigma_{J_2}$  are deduced from the measured total noise powers  $\sigma_{n_1}$  and  $\sigma_{n_2}$  for various harmonic orders  $n$  by taking measurement on both the fundamental and second-harmonic pulse trains.

If the cross-correlation between  $T_n$  and  $I_{1n}$  and that between  $T_n$  and  $\Delta t_{1n}$  are negligible, which is an appropriate assumption for active mode-locking systems[87],  $C_{T \hat{I}_1} \approx C_{T \Delta t_1} \approx 0$ . In this case,  $C_{T \hat{E}_k} \approx 0$  and Eq. 93 is simplified to become

$$\sigma_{n_k}^2 = \sigma_{\hat{E}_k}^2 + (2\pi n f_0)^2 \cdot \sigma_{J_k}^2. \tag{102}$$

Hence  $\sigma_{\hat{E}}$  and  $\sigma_J$  for the fundamental and the second-harmonic pulses can be obtained by using the previously established power-spectrum technique[58]. In this special situation, only four equations (Eqs. 95, 96, 99, 100) need to be solved to obtain the four unknown noise parameters:  $\sigma_{\hat{I}_1}$ ,  $\sigma_{\Delta t_1}$ ,  $\sigma_T$ , and  $C_{\Delta t_1 \hat{I}_1}$ . The noise parameters of a mode-locked laser can then be characterized when the values of  $\sigma_{\hat{E}_1}$ ,  $\sigma_{\hat{E}_2}$ ,  $\sigma_{J_1}$ , and  $\sigma_{J_2}$  are determined.

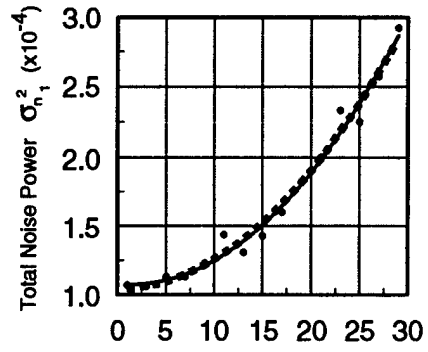
## A.4 Experimental Demonstration

The noise power spectra of a Quantronix 416 actively mode-locked Nd:YLF laser were measured using a *p-i-n* high-speed photodetector terminated directly into a Hewlett-Packard 8650A spectrum analyzer. The 3-dB bandwidth of the detection system including the photodetector and the spectrum analyzer is about 2.9 GHz. The laser generates pulses at 1.053  $\mu\text{m}$  wavelength with a FWHM pulsewidth of 30 ps at a repetition rate of 76 MHz. The second harmonic pulses at 527 nm wavelength were generated by sending the fundamental pulses through a KTP crystal. They have an averaged FWHM pulsewidth of 20 ps.

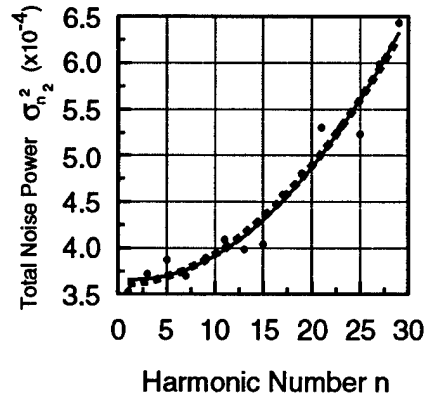
The noise power spectra of the odd harmonics of both the fundamental and the second harmonic pulses were measured. The resolution bandwidth,  $B$ , of the spectrum analyzer is 30 Hz for a frequency offset less than 2.5 kHz. The total noise power  $\sigma_{n_k}^2$  was calculated by integrating the power spectral density from 50 Hz to 1.5 kHz. The total noise power  $\sigma_{n_k}^2$  of different harmonic order  $n$  for both the fundamental and the second harmonic pulses are shown in Figs. 61(a) and (b), respectively. The total noise power of the second harmonic pulses are higher than that of the fundamental pulses.

Using Eq. 93,  $\sigma_{E_k}$ ,  $\sigma_{J_k}$ , and  $C_{TE_k}$  for the fundamental and the second harmonic pulses can be determined by the dependence of the total noise power  $\sigma_{n_k}^2$  on the harmonic number  $n$ . The solid curves in Figs. 61(a) and (b) are the best-fitted curves of the total noise power  $\sigma_{n_k}^2$  as a function of the harmonic number  $n$  using Eq. 93. The values of  $\sigma_{\hat{I}_1}$ ,  $\sigma_{\Delta t_1}$ ,  $\sigma_T$ ,  $C_{\Delta t_1 \hat{I}_1}$ ,  $C_{T \hat{I}_1}$ , and  $C_{T \Delta t_1}$  were then deduced using Eqs. 95-100. The results are summarized in Table 3 as Model 1.

It can be seen that the rms pulse-energy fluctuation of the second harmonic



(a)



(b)

Figure 61: Total noise power  $\sigma_{n_k}^2$  of (a) the fundamental and (b) the second harmonic pulses of an actively mode-locked Nd:YLF laser. The solid line is the fitting curve of Eq. 93. The dashline is the fitting curve of Eq. 102.

	$\sigma_{\widehat{E_1}}(\%)$	$\sigma_{\widehat{E_2}}(\%)$	$\sigma_{J_1}(\text{ps})$	$\sigma_{J_2}(\text{ps})$	$C_{TE_1}(\% \cdot \text{ps})$	$C_{TE_2}(\% \cdot \text{ps})$
Model 1	1.0	1.9	1.0	1.2	-0.15	-0.21
Model 2	1.0	1.9	1.0	1.3	-	-
	$\sigma_{\widehat{I_1}}(\%)$	$\sigma_{\Delta t_1}(\text{ps})$	$\sigma_T(\text{ps})$	$C_{\Delta t_1 \widehat{I_1}}(\% \cdot \text{ps})$	$C_{T\widehat{I_1}}(\% \cdot \text{ps})$	$C_{T\Delta t_1}(\text{ps}^2)$
Model 1	4	1.6	1.1	-7	-0.06	-0.03
Model 2	4	1.7	1.1	-8	-	-

Table 3: Noise parameters of the fundamental and second harmonic pulses

pulses is higher than that of the fundamental pulses, and the total jitter term of the second-harmonic pulses is slightly larger than that of the fundamental pulses as well. Furthermore, it was found that the rms normalized pulse-amplitude fluctuation  $\sigma_{\widehat{I_1}}$  is larger than the rms normalized pulse-energy fluctuation  $\sigma_{\widehat{E_1}}$ . The rms pulse timing jitter  $\sigma_T$  is slightly different from the rms total jitter  $\sigma_J$  in magnitude. It can be seen from Table 3 that there is a strong correlation between the pulsewidth fluctuation and that of the pulse-amplitude fluctuation because the absolute value of  $C_{\Delta t_1 \widehat{I_1}}$  is comparable to that of the product of  $\sigma_{\Delta t_1}$  and  $\sigma_{\widehat{I_1}}$ . The value of  $C_{\Delta t_1 \widehat{I_1}}$  is found to be negative, which implies that a pulsewidth fluctuation that reduces the pulsewidth is accompanied by an intensity fluctuation that increases the intensity amplitude, and vice versa. The values of  $C_{T\widehat{I_1}}$  and  $C_{T\Delta t_1}$  are also found to be negative. However, their absolute values are much smaller than those of  $\sigma_T \sigma_{\widehat{I_1}}$  and  $\sigma_T \sigma_{\Delta t_1}$ , respectively. Therefore,  $C_{T\widehat{I_1}}$  and  $C_{T\Delta t_1}$  are negligible in our case, whereas  $C_{\Delta t_1 \widehat{I_1}}$  is not.

In order to verify that  $C_{T\widehat{I_1}}$  and  $C_{T\Delta t_1}$  are negligible in our case, Eq. 102 is used to fit the experimental data in this case. The dashed curves in Figs. 61(a) and (b) are the best-fitted curves for the total noise power  $\sigma_{n_k}^2$  as a function of the harmonic number  $n$  using Eq. 102. The deduced noise parameters are summarized

in Table 3 as Model 2. The values of  $\sigma_{\hat{I}_1}$ ,  $\sigma_{\Delta t_1}$ ,  $\sigma_T$ , and  $C_{\Delta t_1 \hat{I}_1}$  differ very little in both models. These results justified the uncorrelated noise model in our actively mode-locked Nd:YLF laser.

## A.5 Discussions and Conclusion

Although the physical origin of the noise is not discussed in this paper, it can be shown that the noise power spectra can be further simplified if the the optical pulse train has certain special properties. For example, in the case of fundamental soliton pulses, the pulse area is constant and the pulse shape is  $\text{sech}^2$ . We then have the following realtions:

$$\begin{aligned}\frac{1}{2} \frac{I_{1n}}{I_1} &= -\frac{\Delta t_{1n}}{\Delta t_1} \\ S_{\hat{I}_1}(\omega) &= 4 \frac{S_{\Delta t_1}(\omega)}{\Delta t_1^2} \\ \frac{S_{\Delta t_1 \hat{I}_1}(\omega)}{\Delta t_1} &= -\frac{1}{2} S_{\hat{I}_1}(\omega).\end{aligned}\tag{103}$$

The corresponding noise power spectrum becomes

$$\begin{aligned}P_{I_k}(\omega) &= P_{C_k} \sum_n \left\{ 2\pi \delta\left(\omega - n \frac{2\pi}{T}\right) \right. \\ &\quad + \left(k - \frac{1}{2}\right)^2 S_{\hat{I}_1}\left(\omega - n \frac{2\pi}{T}\right) \\ &\quad + \omega \cdot 2 \left(k - \frac{1}{2}\right) \text{Im} \left[ S_{T \hat{I}_1}\left(\omega - n \frac{2\pi}{T}\right) \right] \\ &\quad \left. + \omega^2 \cdot \left[ S_T\left(\omega - n \frac{2\pi}{T}\right) + \frac{\beta_k}{2} \left(k - \frac{1}{2}\right) \Delta t_1^2 S_{\hat{I}_1}\left(\omega - n \frac{2\pi}{T}\right) \right] \right\},\end{aligned}\tag{104}$$

where  $\beta_k$  is that of the  $\text{sech}^2$  pulses. Because Eq. 104 is a quadratic equation of  $\omega$  with only three unknown quantities, only the noise spectrum of the fundametal pulse train has to be measured to deduce all the noise parameters in the case of fundamental soliton laser pulses.

In another special case that the pulses have a constant energy, we have the following relations:

$$\begin{aligned}\frac{I_{1n}}{I_1} &= -\frac{\Delta t_{1n}}{\Delta t_1} \\ S_{\hat{I}_1}(\omega) &= \frac{S_{\Delta t_1}(\omega)}{\Delta t_1^2} \\ \frac{S_{\Delta t_1 \hat{I}_1}(\omega)}{\Delta t_1} &= -S_{\hat{I}_1}(\omega).\end{aligned}\tag{105}$$

The corresponding noise power spectrum becomes

$$\begin{aligned}P_{I_k}(\omega) &= P_{C_k} \sum_n \left\{ 2\pi \delta\left(\omega - n\frac{2\pi}{T}\right) \right. \\ &\quad + (k-1)^2 S_{\hat{I}_1}\left(\omega - n\frac{2\pi}{T}\right) \\ &\quad + \omega \cdot 2(k-1) \operatorname{Im}\left[S_{T\hat{I}_1}\left(\omega - n\frac{2\pi}{T}\right)\right] \\ &\quad \left. + \omega^2 \cdot \left[S_T\left(\omega - n\frac{2\pi}{T}\right) + \beta_k(k-1)\Delta t_1^2 S_{\hat{I}_1}\left(\omega - n\frac{2\pi}{T}\right)\right] \right\}.\end{aligned}\tag{106}$$

Again, Eq. 106 is a quadratic equation of  $\omega$  with only three unknown quantities and only one measurement is needed. However, if  $k = 1$ ,  $S_{\hat{I}_1}$  cannot be determined from Eq. 106. Therefore, the noise power spectrum of the fundamental pulse train alone cannot be used to determine all the noise parameters, but that of the second harmonic pulse train can be used to accomplish this objective.

In conclusion, we demonstrated a measurement technique to characterize the pulse fluctuation noise of CW mode-locked laser pulses. By comparing the noise power spectra of the fundamental pulses and those of the second harmonic pulses, the pulse-amplitude fluctuation, the pulsewidth fluctuation, the pulse timing jitter, and the cross correlations between any two of these three noise parameters of a mode-locked pulse train can be separately quantified.

In the pulse train of our actively mode-locked Nd:YLF laser, the rms pulse-amplitude fluctuation is larger than the rms pulse-energy fluctuation, and the cross correlation between the pulsewidth and the pulse-amplitude fluctuation was found to be negative and not negligible. The pulsewidth fluctuation is also not negligible in comparison to the peak intensity noise and the pulse timing jitter.

## B Small Noise Approximations

The intensity of a periodic pulse train is given in Eq. (1) as

$$I_1(t) = \sum_{n=-\infty}^{+\infty} (I_1 + I_{1n}) h_1 \left( \frac{t - nT - T_n}{\Delta t_1 + \Delta t_{1n}} \right). \quad (107)$$

Under the assumptions that  $\Delta t_{1n}/\Delta t_1 \ll 1$ , that the pulse shape function,  $h_1(t)$ , has a convergent Taylor series expansion about the point  $t = 0$ , and that the pulse energy is contained within a finite range near the center of the pulse, the pulse shape function can be approximated by the following function:

$$\begin{aligned} h_1 \left( \frac{t}{\Delta t_1 + \Delta t_{1n}} \right) &\approx h_1 \left[ \frac{t}{\Delta t_1} \left( 1 - \frac{\Delta t_{1n}}{\Delta t_1} + \frac{\Delta t_{1n}^2}{\Delta t_1^2} \right) \right] \\ &\approx h_1 \left( \frac{t}{\Delta t_1} \right) - \left( \frac{\Delta t_{1n}}{\Delta t_1} + \frac{\Delta t_{1n}^2}{\Delta t_1^2} \right) t \frac{d}{dt} h_1 \left( \frac{t}{\Delta t_1} \right) \\ &\quad + \frac{1}{2} \frac{\Delta t_{1n}^2}{\Delta t_1^2} t^2 \frac{d^2}{dt^2} h_1 \left( \frac{t}{\Delta t_1} \right). \end{aligned} \quad (108)$$

Under the approximation that  $I_{1n}/I_1 \ll 1$  and  $2\pi f_m T_n \ll 1$ , where  $f_m$  is the maximum frequency measured, the optical pulse train can be approximated by

$$\begin{aligned} I_1(t) = I_1 \sum_n &\left[ \left( 1 + \frac{I_{1n}}{I_1} \right) h_1 \left( \frac{t - nT}{\Delta t_1} \right) \right. \\ &\left. - \left( T_n + \frac{I_{1n} T_n}{I_1} - \frac{\Delta t_{1n} T_n}{\Delta t_1} \right) \dot{h}_1 \left( \frac{t - nT}{\Delta t_1} \right) \right] \end{aligned}$$



$$\begin{aligned}
& - \left( \frac{\Delta t_{1n}}{\Delta t_1} - \frac{\Delta t_{1n}^2}{\Delta t_1^2} + \frac{I_{1n} \Delta t_{1n}}{I_1 \Delta t_1} \right) (t - nT) \dot{h}_1 \left( \frac{t - nT}{\Delta t_1} \right) \\
& + \frac{1}{2} T_n^2 \ddot{h}_1 \left( \frac{t - nT}{\Delta t_1} \right) + \frac{\Delta t_{1n} T_n}{\Delta t_1} (t - nT) \ddot{h}_1 \left( \frac{t - nT}{\Delta t_1} \right) \\
& + \frac{1}{2} \frac{\Delta t_{1n}^2}{\Delta t_1^2} (t - nT)^2 \ddot{h}_1 \left( \frac{t - nT}{\Delta t_1} \right) \Big]. \tag{109}
\end{aligned}$$

where

$$\dot{h}_1 \left( \frac{t - nT}{\Delta t_1} \right) = \frac{d}{dt} h_1 \left( \frac{t - nT}{\Delta t_1} \right) \tag{110}$$

and

$$\ddot{h}_1 \left( \frac{t - nT}{\Delta t_1} \right) = \frac{d^2}{dt^2} h_1 \left( \frac{t - nT}{\Delta t_1} \right) \tag{111}$$

## C Derivation of Power Spectra

The time-averaged autocorrelation function of a cyclostationary process

$$a(t) = \sum_{n=-\infty}^{\infty} a_n h(t - nT) \tag{112}$$

is[88]

$$\overline{R}(\tau) = \frac{1}{T} \sum_{m=-\infty}^{\infty} R_a[m] \rho(\tau - mT), \tag{113}$$

where

$$R_a[m] = E\{a_{n+m} a_n\} \quad \rho(t) = h(t) * h(-t). \tag{114}$$

Assuming that the stochastic sequences,  $I_{1n}$ ,  $T_{1n}$ , and  $\Delta t_{1n}$ , are stationary and that the intensity function,  $I_1(t)$ , is cyclostationary (or periodic stationary)[88],

the time-averaged autocorrelation function of  $I_1(t)$  can be written as

$$\begin{aligned}
\overline{R_{I_1}}(\tau) = \frac{I_1^2}{T} \sum_{m=-\infty}^{\infty} \left\{ \left( 1 + \frac{R_{I_1}[m]}{I_1^2} \right) \rho_{00} \left( \frac{\tau - mT}{\Delta t_1} \right) \right. \\
+ \frac{R_{\Delta t_1}[m]}{\Delta t_1^2} \rho_{1'1'} \left( \frac{\tau - mT}{\Delta t_1} \right) \\
+ R_T[m] \rho_{11} \left( \frac{\tau - mT}{\Delta t_1} \right) \\
- \frac{R_{I_1 T}[m]}{I_1} \rho_{01} \left( \frac{\tau - mT}{\Delta t_1} \right) - \frac{R_{T I_1}[m]}{I_1} \rho_{10} \left( \frac{\tau - mT}{\Delta t_1} \right) \\
+ \frac{R_{T \Delta t_1}[m]}{\Delta t_1} \rho_{1'1} \left( \frac{\tau - mT}{\Delta t_1} \right) - \frac{R_{\Delta t_1 T}[m]}{\Delta t_1} \rho_{11'} \left( \frac{\tau - mT}{\Delta t_1} \right) \\
+ \overline{T_n^2} \rho_{02} \left( \frac{\tau - mT}{\Delta t_1} \right) \\
+ \left[ \frac{\overline{\Delta t_{1n}^2}}{\Delta t_1^2} - \frac{\overline{I_{1n} \Delta t_{1n}}}{I_1 \Delta t_1} - \frac{R_{I_1 \Delta t_1}[m]}{I_1 \Delta t_1} \right] \rho_{01'} \left( \frac{\tau - mT}{\Delta t_1} \right) \\
+ \left[ \frac{\overline{\Delta t_{1n}^2}}{\Delta t_1^2} - \frac{\overline{I_{1n} \Delta t_{1n}}}{I_1 \Delta t_1} - \frac{R_{\Delta t_1 I_1}[m]}{\Delta t_1 I_1} \right] \rho_{1'0} \left( \frac{\tau - mT}{\Delta t_1} \right) \\
+ \frac{1}{2} \frac{\overline{\Delta t_{1n}^2}}{\Delta t_1^2} \rho_{02'} \left( \frac{\tau - mT}{\Delta t_1} \right) \\
+ \frac{1}{2} \frac{\overline{\Delta t_{1n}^2}}{\Delta t_1^2} \rho_{2'0} \left( \frac{\tau - mT}{\Delta t_1} \right) \\
+ \frac{\overline{\Delta t_{1n} T_n}}{\Delta t_1} \rho_{02''} \left( \frac{\tau - mT}{\Delta t_1} \right) \\
+ \left. \frac{\overline{\Delta t_{1n} T_n}}{\Delta t_1} \rho_{2''0} \left( \frac{\tau - mT}{\Delta t_1} \right) \right\} \quad (115)
\end{aligned}$$

where

$$\begin{aligned}
R_{I_1}[m] &= E\{I_{1n+m} I_{1n}\} & R_{\Delta t_1} &= E\{\Delta t_{1n+m} \Delta t_{1n}\} \\
R_{T_1}[m] &= E\{T_{n+m} T_n\} & R_{I_1 T}[m] &= E\{I_{1n+m} T_n\} \\
R_{\Delta t_1 T}[m] &= E\{\Delta t_{1n+m} T_n\} & R_{I_1 \Delta t_1}[m] &= E\{I_{1n+m} \Delta t_{1n}\} \quad (116)
\end{aligned}$$

and

$$\rho_{00} \left( \frac{t}{\Delta t_1} \right) = h_1 \left( \frac{t}{\Delta t_1} \right) * h_1 \left( \frac{-t}{\Delta t_1} \right) \quad \rho_{11} \left( \frac{t}{\Delta t_1} \right) = h_1 \left( \frac{t}{\Delta t_1} \right) * h_1 \left( \frac{-t}{\Delta t_1} \right)$$

$$\begin{aligned}
\rho_{01} \left( \frac{t}{\Delta t_1} \right) &= h_1 \left( \frac{t}{\Delta t_1} \right) * \dot{h}_1 \left( \frac{-t}{\Delta t_1} \right) & \rho_{10} \left( \frac{t}{\Delta t_1} \right) &= \dot{h}_1 \left( \frac{t}{\Delta t_1} \right) * h_1 \left( \frac{-t}{\Delta t_1} \right) \\
\rho_{01'} \left( \frac{t}{\Delta t_1} \right) &= h_1 \left( \frac{t}{\Delta t_1} \right) * \left[ -t \cdot \dot{h}_1 \left( \frac{-t}{\Delta t_1} \right) \right] \\
\rho_{1'0} \left( \frac{t}{\Delta t_1} \right) &= \left[ t \cdot \dot{h}_1 \left( \frac{t}{\Delta t_1} \right) \right] * h_1 \left( \frac{-t}{\Delta t_1} \right) \\
\rho_{02} \left( \frac{t}{\Delta t_1} \right) &= h_1 \left( \frac{t}{\Delta t_1} \right) * \ddot{h}_1 \left( \frac{-t}{\Delta t_1} \right) \\
\rho_{1'1'} \left( \frac{t}{\Delta t_1} \right) &= \left[ t \cdot \dot{h}_1 \left( \frac{t}{\Delta t_1} \right) \right] * \left[ -t \cdot \dot{h}_1 \left( \frac{-t}{\Delta t_1} \right) \right] \\
\rho_{02'} \left( \frac{t}{\Delta t_1} \right) &= h_1 \left( \frac{t}{\Delta t_1} \right) * \left[ (-t)^2 \cdot \ddot{h}_1 \left( \frac{-t}{\Delta t_1} \right) \right] \\
\rho_{2'0} \left( \frac{t}{\Delta t_1} \right) &= \left[ t^2 \cdot \ddot{h}_1 \left( \frac{t}{\Delta t_1} \right) \right] * h_1 \left( \frac{-t}{\Delta t_1} \right) \\
\rho_{02''} \left( \frac{t}{\Delta t_1} \right) &= h_1 \left( \frac{t}{\Delta t_1} \right) * \left[ -t \cdot \ddot{h}_1 \left( \frac{-t}{\Delta t_1} \right) \right] \\
\rho_{2''0} \left( \frac{t}{\Delta t_1} \right) &= \left[ t \cdot \ddot{h}_1 \left( \frac{t}{\Delta t_1} \right) \right] * h_1 \left( \frac{-t}{\Delta t_1} \right) \\
\rho_{11'} \left( \frac{t}{\Delta t_1} \right) &= \dot{h}_1 \left( \frac{t}{\Delta t_1} \right) * \left[ -t \cdot \dot{h}_1 \left( \frac{-t}{\Delta t_1} \right) \right] \\
\rho_{1'1} \left( \frac{t}{\Delta t_1} \right) &= \left[ t \cdot \dot{h}_1 \left( \frac{t}{\Delta t_1} \right) \right] * \dot{h}_1 \left( \frac{-t}{\Delta t_1} \right)
\end{aligned} \tag{117}$$

The Fourier transform of the time-averaged autocorrelation  $\overline{R_{I_1}}(\tau)$  is the power spectrum

$$\begin{aligned}
P_{I_1}(\omega) \approx & \frac{I_1^2}{T^2} \Delta t_1^2 |H_1(\Delta t_1 \omega)|^2 \sum_n \left\{ 2\pi \delta \left( \omega - n \frac{2\pi}{T} \right) \right. \\
& + S_{\hat{I}_1} \left( \omega - n \frac{2\pi}{T} \right) + \frac{S_{\Delta t_1} \left( \omega - n \frac{2\pi}{T} \right)}{\Delta t_1^2} + 2 \frac{\text{Re}[S_{\Delta t_1 \hat{I}_1}(\omega - n \frac{2\pi}{T})]}{\Delta t_1} \\
& + \omega \cdot 2 \cdot \text{Im} \left[ S_{T \hat{I}_1} \left( \omega - n \frac{2\pi}{T} \right) \right] + \omega \cdot 2 \frac{\text{Im}[S_{T \Delta t_1}(\omega - n \frac{2\pi}{T})]}{\Delta t_1} \\
& + \omega^2 \cdot S_T \left( \omega - n \frac{2\pi}{T} \right) \\
& + \omega \cdot \text{Re} \left[ \frac{d}{d\omega} \ln H_1(\Delta t_1 \omega) \right] \cdot \frac{2S_{\Delta t_1}(\omega - n \frac{2\pi}{T})}{\Delta t_1^2} \\
& \left. + \omega \cdot \text{Re} \left[ \frac{d}{d\omega} \ln H_1(\Delta t_1 \omega) \cdot \frac{2S_{\Delta t_1 \hat{I}_1}(\omega - n \frac{2\pi}{T})}{\Delta t_1} \right] \right\}
\end{aligned} \tag{118}$$

where

$$\begin{aligned}
\sum_n S_{\hat{I}_1} \left( \omega - n \frac{2\pi}{T} \right) &= T \sum_m \frac{R_{I_1}[m]}{I_1^2} \exp(-imT\omega) \\
\sum_n S_{\Delta t_1} \left( \omega - n \frac{2\pi}{T} \right) &= T \sum_m R_{\Delta t_1}[m] \exp(-imT\omega) \\
\sum_n S_T \left( \omega - n \frac{2\pi}{T} \right) &= T \sum_m R_T[m] \exp(-imT\omega) \\
\sum_n S_{\Delta t_1 \hat{I}_1} \left( \omega - n \frac{2\pi}{T} \right) &= T \sum_m \frac{R_{\Delta t_1 I_1}[m]}{I_1} \exp(-imT\omega) \\
\sum_n S_{T \hat{I}_1} \left( \omega - n \frac{2\pi}{T} \right) &= T \sum_m \frac{R_{T I_1}[m]}{I_1} \exp(-imT\omega) \\
\sum_n S_{T \Delta t_1} \left( \omega - n \frac{2\pi}{T} \right) &= T \sum_m R_{T \Delta t_1}[m] \exp(-imT\omega)
\end{aligned} \tag{119}$$

and

$$H_1(\omega) = \int_{-\infty}^{\infty} h_1(t) \exp(-i\omega t) dt \tag{120}$$

is the Fourier transform of  $h_1(t)$ . Following a similar procedure, the power spectrum for the second harmonic can also be derived.

## D Bibliography

1. E.C. Cheung, K. Koch, G.T. Moore, and J.M. Liu, "Measurements of Second-Order Nonlinear Optical Coefficients from the Spectral Brightness of Parametric Fluorescence," *Opt. Lett.* **19**, 168-170 (1994).
2. J.M. Liu, "Parametric Generation of Broadly Wavelength-Tunable Picosecond and Femtosecond Pulses," *Current Topics in Quantum Electronics*, **1**, 73-90 (1994). (Invited)
3. Yong Wang, L.P. Chen, and J.M. Liu, "Noise Characterization of Mode-Locked Lasers by Comparing the Power Spectra of the Fundamental and Second Harmonic Pulses," *Opt. Lett.* **20**, 2117-2119 (1995).
4. L.P. Chen, Yong Wang, and J.M. Liu, "Singly-Resonant Optical Parametric Oscillator Synchronously Pumped by Frequency-Doubled Additive-Pulse Mode-Locked Nd:YLF Laser Pulses," *J. Opt. Soc. Am. B.* **12**, 2192-2198 (1995).
5. J.M. Liu, Guosheng Zhou, and S.J. Pyo, "Parametric Gain of the Generation and the Amplification of Ultrashort Optical Pulses," *J. Opt. Soc. Am. B.* **12**, 2274-2287 (1995).
6. L.P. Chen, Yong Wang, and J.M. Liu, "Spectral Measurement of the Noise in Continuous-wave Mode-Locked Laser Pulses," accepted for publication in *IEEE J. Quantum Electron.* **32** (1996).

## DISTRIBUTION LIST

AUL/LSE Bldg 1405 - 600 Chennault Circle Maxwell AFB, AL 36112-6424	1 cy
DTIC/OCP 8725 John J. Kingman Rd, Suite 0944 Ft Belvoir, VA 22060-6218	2 cys
AFSAA/SAI 1580 Air Force Pentagon Washington, DC 20330-1580	1 cy
PL/SUL Kirtland AFB, NM 87117-5776	2 cys
PL/HO Kirtland AFB, NM 87117-5776	1 cy
Prof. J. M. Liu 56-147C Engineering IV Electrical Engineering Department University of California, Los Angeles Los Angeles, CA 90095-159410	2 cys
Official Record Copy PL/LIDN/Dr Chris Clayton	2 cys